Universidade de Aveiro
2022

Aneeta
Jaggernauth

DEPOSIÇÃO POR CAMADA ATÓMICA DE FILMES COM ELEVADA CONSTANTE DIELÉTRICA PARA ESTRUTURAS MOS EM DIAMANTE

ATOMIC LAYER DEPOSITION OF HIGH-κ DIELECTRIC FILMS FOR DIAMOND MOS STRUCTURES

Universidade de Aveiro
2022

Aneeta Jaggernauth

DEPOSIÇÃO POR CAMADA ATÓMICA DE FILMES COM ELEVADA CONSTANTE DIELÉTRICA PARA ESTRUTURAS MOS EM DIAMANTE

ATOMIC LAYER DEPOSITION OF HIGH-κ DIELECTRIC FILMS FOR DIAMOND MOS STRUCTURES

Tese apresentada à Universidade de Aveiro para cumprimento dos requisitos necessários à obtenção do grau de Doutor em Ciência e Engenharia de Materiais, realizada sob a orientação científica do Doutor Rui Ramos Ferreira e Silva, Professor Associado do Departamento de Engenharia de Materiais e Cerâmica da Universidade de Aveiro e da Doutora Joana Catarina Martins Mendes, Investigadora no Instituto de Telecomunicações – Pólo de Aveiro.

This work was supported by FCT through the doctoral grant # SFRH/BD/144984/2019, within the scope of PORTUGAL2020, and developed within the project CICECO-Aveiro Institute of Materials, UIDB/50011/2020, UIDP/50011/2020 & LA/P/0006/2020, financed by national funds through the FCT/MEC (PIDDAC). The Instituto de Telecomunicações – pólo de Aveiro is also acknowledged for providing the required conditions.

FCT Fundação para a Ciência e a Tecnologia · PORTUGAL 2020 · UNIÃO EUROPEIA · COMPETE 2020 · REPÚBLICA PORTUGUESA · CENTRO 2020 · ciceco aveiro institute of materials

This thesis is dedicated to lifelong learning and its practitioners

o júri

Presidente

Prof. Doutor João Manuel Nunes Torrão
Professor Catedrático, Universidade de Aveiro

Vogais

Prof. Doutora Sandra Maria Fernandes Carvalho
Professora Associada com Agregação, Universidade de Coimbra

Prof. Doutor Henrique Leonel Gomes
Professor Associado com Agregação, Universidade de Coimbra

Prof. Doutor Pedro Miguel Cândido Barquinha
Professor Associado, Universidade Nova de Lisboa

Prof. Doutor Luiz Fernando Ribeiro Pereira
Professor Auxiliar, Universidade de Aveiro

Doutora Joana Catarina Martins Mendes
Investigadora, Instituto de Telecomunicações (coorientadora)

Acknowledgements

Throughout my life I have had the good fortune of being moulded by sages dedicated to nurturing the minds and character of those in their charge.

The first and foremost of these are my parents who have bestowed within me a profound respect for education and learning, an unfailing connection to Divinity, and confidence for charting my own course. My sister has served as my faithful moral compass on my chosen, winding but scenic, path and I consider myself all the more enduring because of her. No part of my journey would be possible without them, and no words will ever sufficiently express my gratitude to and for them.

In this particular endeavour my academic advancement has been placed in the capable hands of my supervisor, Prof. Dr. Rui Silva and co-supervisor, Dr. Joana Mendes. I am grateful to them for furnishing me with this opportunity to learn and explore towards the attainment of scientific understanding as well as more global perspectives. They have permitted me the freedom to develop and trust my own intuition and the direction of my curiosities. I believe these to be rare qualities that will serve me well in academia and life in general. Their leadership and guidance have been pillars in my experience, those only to be cherished.

I also extend my gratitude to the persons in my lab who have graciously helped me in the more practical aspects of the thesis work, in particular Miguel Neto and Ricardo Silva, and all others who have taken the time to discuss my doubts and concerns, directing me to greater understanding and focus. I am humbled by their interest and willingness and can only hope to emulate these attributes. This sentiment holds for the many at the Department of Materials and Ceramic Engineering at Universidade de Aveiro who have keenly attended to my dilemmas, both academic and administrative. I am deeply appreciative to them, as I am to all mentioned in these few paragraphs as well as the numerous who are not, for it will easily compete with the length of the thesis.

Finally, this thesis would not have been possible without the diligent work of generous collaborators, Marina Gutiérrez, Mary Paz Alegre, Daniel Araújo, Igor Bdikin, Jolien Dendooven, Véronique Cremers, Jonas Deuermeier, Jordi Llobet and Philippe Godignon.

To all these sages, I say, thank you for doing what you do and doing it so well, so that I may have this opportunity.

palavras-chave

Òxidos dielétricos
Deposição por camada atómica
Diamante policristalino
Interfaces
Dispositivos MOS

Resumo

A incapacidade de os dispositivos eletrónicos em silício manterem o desempenho desejado nalgumas aplicações específicas levou à procura de novos materiais que cumpram os requisitos necessários. No caso particular dos dispositivos metal-óxido-semicondutor (MOS) esta procura tem sido feita a dois níveis. O primeiro envolve a utilização de filmes com constante dielétrica κ elevada: à medida que mais e mais dispositivos são integrados num mesmo circuito para possibilitar a multiplicidade das operações, o tamanho de cada dispositivo individual tem vindo a diminuir, o que leva à necessidade de procurar materiais para substituir os filmes convencionais de SiO_2 e Al_2O_3 em transístores e condensadores, de modo a manter o controlo do fluxo de portadores e evitar correntes de fuga. O segundo diz respeito à utilização de materiais semicondutores de banda extremamente elevada que possibilitem o funcionamento dos dispositivos em condições extremas. O diamante policristalino (DPC) tem estas características e oferece uma relação custo-benefício favorável para o fabrico de dispositivos MOS, no entanto é ainda necessário o seu estudo para estas aplicações em concreto.

A deposição de filmes com constante dielétrica elevada sobre o DPC tem sido limitada ao Al_2O_3, não obstante a possibilidade de fabrico de filmes com constante dielétrica mais elevada através da deposição por camada atómica (DCA), uma técnica que tem como vantagem inerente a ocorrência de reações químicas auto-limitantes e saturantes com controlo ao nível da camada atómica, sendo portanto vantajosa para o estudo das propriedades interfaciais.

O trabalho desta tese explora assim a utilização de óxidos dielétricos de Al (AlO), Ta (TaO) e Ti (TiO) em estruturas MOS, com filmes de DPC como camada semicondutora. A novidade deste trabalho prende-se com o estudo das propriedades na interface e com questões de fabricação, mais especificamente com a estabilidade mecânica de filmes de AlO depositados em superfícies de DPC com terminações químicas diferentes, com desafios inerentes à DCA de filmes de TaO, com o alinhamento das bandas de energia entre filmes de TIO e DPC e com o desempenho de MOSFETs com dielétrico de TiO em filmes de diamante dopado com boro. Em suma, esta tese descreve um conjunto de conhecimentos pertinentes para a utilização de óxidos com elevada constante dielétrica depositados por DCA em dispositivos MOS baseados em diamante.

keywords

Dielectric oxides
Atomic layer deposition
Polycrystalline diamond
Interfaces
MOS devices

abstract

Changes in the expected performance of electronic devices in extreme applications have heavily influenced investigation into Si-substitute materials having the ability to meet these demands. Two examples are especially pertinent to the performance of metal oxide semiconductor (MOS) devices. The first is the move towards films with high dielectric constants (high-κ); as more devices are integrated into the same circuit to facilitate the numerous system operations, the size of each device is greatly reduced necessitating exploration into more suitable options for replacing SiO_2 and Al_2O_3 films in transistors and capacitors to effectively control semiconductor charge carriers and prevent charge leakage. The second is investigation into ultra-wide band gap (UWBG) semiconductor materials to efficiently permit device operation in extreme conditions. Polycrystalline diamond (PCD) is an UWBG material that provides a cost-effective option for MOS devices, but it has yet to be fully studied for these applications.

The combination of high-κ films on PCD for MOS components has been limited to Al_2O_3 despite the ability to fabricate films with higher κ values by atomic layer deposition (ALD), a technique which imparts advantages of self-limiting and saturation reactions with atomic layer control, thus being advantageous for studying interfacial properties.

The work in this thesis therefore explores dielectric oxides of Al (AlO), Ta (TaO) and Ti (TiO) for use in MOS structures, with PCD films utilized as the semiconducting layer. Novelty is achieved by investigating interfacial properties and fabrication issues, more specifically, the mechanical stability of AlO films on chemically different PCD surfaces, challenges related to the ALD of TaO films, energy band alignment between TiO and PCD, and the behaviour of MOSFETs utilizing TiO dielectrics on B-doped diamond (BDD). In all, this thesis provides a body of research pertinent to the use of ALD high-κ oxides for use in diamond-based MOS devices.

Table of Contents

Introduction 1

Chapter 1: Literature Review 5

1.0 The evolution of MOSFET materials 5

2.0 Atomic layer deposition (ALD) 8
- 2.1. ALD Technique 8
- 2.2. Main Parameters 9
  - 2.2.1 Pulse and purge durations 9
  - 2.2.2 Deposition temperature 11
  - 2.2.3 Precursor temperature 12

3.0 Polycrystalline Diamond Films (PCD) 13
- 3.1 PCD film growth 13
- 3.2 Diamond film conductivity 15
  - 3.2.1 Surface and bulk conductivity 15
  - 3.2.2 PCD film conductivity 18

4.0 ALD of High-κ Films on Polycrystalline Diamond 19
- 4.1 High-κ Film Nucleation 19
- 4.2 Manipulation of Surface Terminations 20
  - 4.2.1 PCD surface O-bond configurations 21
  - 4.2.2 Surface O-terminations and PCD crystal orientation 24
- 4.3 Temperature dependent high-κ fabrication 24
- 4.4 Substrate Topography 27

5.0 Diamond-based MOS Devices 28
- 5.1 High-κ oxide films in Diamond MOS Devices 28
- 5.2 Energy Band Alignment and Electronic Manipulation 31
- 5.3 Diamond MOS Device Performance 33

Chapter 2: Interface Quality of ALD Alumina Films with Polycrystalline Diamond 45

1.0 Introduction 45

2.0 Experimental Procedure 46
- 2.1. Growth of B-doped Diamond Films 46
- 2.2. Deposition of Alumina Thin Films by ALD 48
- 2.3. Characterization Techniques 49

3.0 Results and Discussion 50
- 3.1. BDD Thin Films 50
- 3.1 ALD Alumina Thin Films 53
- 3.2 Interfacial Analysis 54

4.0 Conclusions *61*

Chapter 3: Fabrication of Tantalum Oxide Films by ALD Using PDMAT and H_2O 65

1.0 Introduction *65*

2.0 Experimental Procedure *67*
2.1. TaO Film Fabrication by ALD 67
2.2. TaO Film Characterization 67

3.0 Results and Discussion *68*

4.0 Conclusions *76*

Chapter 4: ALD of Titanium Oxide Films and their Energy Band Alignment with Polycrystalline Diamond 79

1.0 Introduction *79*

2.0 Experimental Procedure *81*
2.1. TiO Film Fabrication by ALD 81
2.2. TiO Films on PCD Surfaces 81
2.2.1 *Growth of PCD Films by HFCVD* 81
2.2.2 *ALD TiO films on PCD* 82
2.3. Characterization Techniques 82

3.0 Results and Discussion *82*
3.1. Fabrication of Titanium Oxide Films 82
3.2. XPS Analysis of TiO Films 84
3.3. Energy band alignment of TiO with H-PCD 86
3.3.1 Modification of the H-terminated PCD Surface by TiO Precursor Exposure 87
3.3.2 Determination of the TiO-H-PCD Energy Band Alignment 90

4.0 Conclusions *93*

Chapter 5: Fabrication of B-doped Polycrystalline Diamond Films and MOS Devices 99

1.0 Introduction *99*

2.0 Experimental Procedure *101*
2.1. Diamond Film Fabrication 101
2.2. Diamond Film Characterization 101
2.3. TiO Deposition on Diamond Film Surface 102
2.4. MOSFET Fabrication and Characterization 102

3.0 Results and Discussion *103*
3.1. PCD Film Sheet Resistivity 103
3.2. MOS Device Characterization 106

4.0 Conclusions *112*

Chapter 6: General Conclusions and Future Perspectives 115

List of Figures

Figure 1: Schematic representations of a basic MOSFET design (A) showing the position of the gate insulator, which is an oxide layer between the gate contact and semiconductor; (B) describing the operation of a p-type MOSFET in depletion mode. 5
Figure 2: Representation of one ALD cycle for Al_2O_3 using precursors, trimethylaluminium (TMA) and water. This process is prevalent in literature, typically starting with hydroxyl-terminated surfaces. Purging prevents mixing of precursors by removing any unreacted precursor and by product molecules formed from precursor-surface reactions. 9
Figure 3: Graphical representations of saturation and self-limitation in ALD reactions investigated by changes in growth per cycle (GPC) with (A) pulse duration of precursors, (B) purging duration and (C) deposition temperature. Constant GPCs exhibit regions of saturation and self-limitation, the ALD window exhibits the temperatures over which precursor reactions with the surface are ideal[23,29,30]. 11
Figure 4: Schematic of HFCVD technique to produce the gas species contributing to B doped diamond growth; the image is based on literature investigating both theoretical and experimental findings[48,59]. The gas molecules are dissociated to a reactive species upon exposure to heated filaments, which allows them to react with the seeded surface resulting in growth of sp^3 diamond. 15
Figure 5: Graph of Hall concentration vs B concentration for MPCVD grown BDD films, where Hall concentration is considered to be a reflection of free hole concentration inside the BDD grains, so that for larger B concentrations the hole concentration is shown to be lower than that for atomic B. The inset graph demonstrates that a lower hole mobility occurs for the most doped sample, attributed to compensation of B acceptor atoms most likely by B incorporation by B-B dimer formation. The highest hole mobility is observed for B doping resulting in a metallic-state film as a result of a high concentration of B acceptor atoms [reprinted by permission from Springer Nature Customer Service Centre GmbH: Springer European Physical Journal (EPJ) from reference[73], Copyright (2013)]. 17
Figure 6: Plot of sheet resistivity for SCD films with 38 nm alumina passivation layers deposited by ALD at temperatures shown, 100-450 ^oC. Diamond sheet resistivity increased after annealing at 550 ^oC for all samples except for that with the surface passivation film deposited at 450 ^oC, suggesting, in this case, true passivation of diamond surface charge carriers [reprinted from[123], Copyright (2014), with the permission of AIP Publishing]. 26
Figure 7: (A) HFVCD and (B) ALD systems at the Department of Ceramics and Materials Engineering at Universidade de Aveiro 48
Figure 8: (A) surface image of as-grown BDD showing polycrystalline morphology; (B) cross-section SEM image of as-grown BDD with average thickness in the range 1.6±0.4 µm; (C) Raman spectrum of as-grown BDD identifying film composition which includes, sp^3 C diamond, sp^2 C from D and G bands of graphite, polymeric sp^2 C and B incorporation. 51
Figure 9: Comparison of H-BDD and O-BDD surfaces by XPS, main contributions are from the structure of BDD, which include C-C/C-H bonding and sp^2 C, and the surface C-OH/C-O-C ligands, which contribute a larger percentage ratio for O-BDD. Inset SEM images demonstrate no change in the morphology due to O_2 plasma treatment. 52
Figure 10: Interface images taken by SEM of ALD alumina on as-grown (left) and surface O_2 plasma functionalized (right) BDD films showing the conformal deposition of the film; average alumina film thickness by SEM was 146±4 nm. 53
Figure 11: Characterization of alumina film fabricated by 1000 ALD cycles; (A) XRR fringe separation used to calculated alumina film thickness of 139.27±0.75 nm; (B) X-Ray diffractogram exhibits that the ALD alumina

film is amorphous and (C) FTIR spectrum revealing film composition of short range order of 2, 4 and 6 coordinated Al-O, and terminal –CO and –OH groups. 54
Figure 12: (A) Optical microscope images of indentation marks produced after loading and unloading of loads 30-150 mN onto the respective samples. The top panel shows, from left to right, indentation marks with increasing load strengths on Al-O-BDD while the bottom panel are those for AlO-H-BDD. Each load value is related to its respective top and bottom image and the scale shown holds for all images. (B) Permanent indentation depth, produced by each load in the range 5-150 mN, demonstrates containment in the alumina film or near the interface (dotted lines) for AlO-O-BDD, but beyond the interface for AlO-H-BDD. Each plotted value reflects the mean and standard deviation of three tests performed at the respective maximum normal applied load. 55
Figure 13: (A) Load-Displacement curve for the maximum normal applied load of 150 mN. Sample displacement results in no major inconsistencies that would identify depths of fractures or delamination; the inset graph demonstrates that the permanent indentation depth occurred deeper into the BDD film for AlO-H-BDD compared to AlO-O-BDD. The permanent depth of 287 nm attained for AlO-H-BDD, was the maximum achieved for all the tests performed at 150 mN. Load-displacement curves for applied loads of 125 and 100 mN, for AlO-H-BDD and AlO-O-BDD, are shown in (B) and (C), and (D) and (E), respectively. 57
Figure 14: AFM images of (A) AlO-H-BDD and (B) AlO-O-BDD with planar and 3D views of the respective indentation marks resulting from loading and unloading of 150 mN. Only a residual indentation mark of the Berkovich tip is shown on the AlO-O-BDD surface when the load is removed, while a circular buckle is formed on the AlO-H-BDD surface showing film delamination. (C) Demonstrates the height (Z) and radius (X) of the areas of film delamination experienced by AlO-H-BDD and is compared to the less deformed AlO-O-BDD surface. 58
Figure 15: HRTEM micrographs of the BDD-Si interface are shown in (A) for AlO-O-BDD and (B) AlO-H-BDD, an amorphous layer at the interface is present for both samples comprising Si, O and C, determined from the EDX analysis, shown in (C) for AlO-O-BDD. 59
Figure 16: STEM-HAADF micrographs and corresponding EDX images are shown in for AlO-O-BDD in the top panel and AlO-H-BDD in the bottom panel; the first image is the STEM-HAADF image of the respective samples and subsequent images are those showing the areas of the sample where C, O and Al are present. The alumina film is adhered to the BDD film in AlO-O-BDD whereas the majority of the alumina film has delaminated from the BDD surface due to loss of cohesive strength. 60
Figure 17: (a) XRF spectra for films deposited at ALD temperatures, 250, 260, 270, 280 ^oC, showing Si Kα and Ta Lα intensities, normalized for 100 cycles; (b) graph of Ta/Si intensity variation with deposition temperature (blue graph), and film growth per cycle (GPC) variation with deposition temperature (green graph) obtained by XRR measurements. 69
Figure 18: Graphs for identifying saturation parameters at ALD temperature of 270 ^oC; (a) XRF spectra showing peak intensities for Si Kα and Ta Lα, normalized for 100 cycles, for films deposited at exposures 0.1, 0.3, 0.4 s; (b) graph showing variation of Ta/Si intensity with H_2O exposure (blue) from XRF spectra in (a), and variation of GPC with H_2O exposure (green) from XRR analysis; points a_1 and a_2 are the respective GPC and Ta/Si intensity for TaO films deposited at 0.3 s exposure until a thickness of 3.5 nm. 69
Figure 19: Graph showing correlation between XRR and XRF techniques for measurement reliability of ALD TaO films; while there is a high correlation between film thickness and Ta/Si intensity, discrepancies exist which can be explained by differences in film density 70
Figure 20: (a) GPC and (b) film thickness variation with number of ALD cycles, obtained by XRR, for TaO films deposited at 270 ^oC with H_2O exposure of 0.3 s and PDMAT exposure of 0.2 s. 71
Figure 21: XRD diffractograms of films deposited at (a) 0.1-0.5 s H_2O exposures, and (b) 0.3 s H_2O exposures for 100 and 250 cycles, with the diffractogram also shown for the latter annealed at 600 ^oC in a N_2 atmosphere.

The film at 0.1 s exposure is amorphous while that at 0.3 s begins to show δ-Ta_2O_5 crystal phase, confirmed by the thicker film at 0.3 s, and with a preferred orientation upon annealing. 73
Figure 22: Surface topography of 0.3 s TaO films at 270 ^oC, obtained by AFM. 74
Figure 23: TaO films on as-grown PCD surfaces deposited with different H_2O exposure times 0.1 s, 0.3 s, and 0.4 s, for 200, 100 and 100 ALD cycles, respectively. 76
Figure 24: (a) XRF spectra showing Ti signals, normalized for 400 cycles, for TiO films deposited at ALD temperatures 180 – 220 ^oC, with precursor residence times of 4 s each; (b) graphically represents the normalized Ti/Si intensities obtained for the films across the temperature range, thus demonstrating the Ti loading with respect to ALD temperature. 83
Figure 25: (a) XRF spectra showing Ti signal for TiO films deposited at precursor residence times 2- 8 s at 210 ^oC; (b) graphical representation of the Ti/Si intensity obtained for films across the residence durations, thus highlighting parameters for saturation. 84
Figure 26: XPS spectra of TiO films deposited at 200 ^oC with 4 s precursor residence times; (a) widescan spectrum; (b) Ti2p doublet; (c) O1s peak showing lattice Ti-O and smaller contributions from O-H and O-C; (d) C1s peak showing contributions from C surface contamination as well as from unreacted precursor. 86
Figure 27: SEM micrograph showing ALD TiO film, approximately 20 nm, on a polycrystalline diamond (PCD) surface 87
Figure 28: XPS spectra of PCD films showing (a) widescan with C1s and O1s peaks; (b) C1s peak, deconvoluted to show 4 contributing peaks; (c) small O1s contribution. 88
Figure 29: XPS spectra of 2 nm TiO films on PCD surface showing (a) widescan with C1s, O1s, Ti2p and N1s peaks identified; (b) Ti2p peak, deconvoluted to show both stoichiometric TiO_2 peaks as well as small Ti^{3+} contributions; (c) O1s peak primarily from Ti-O and (d) C1s peak showing contributions from the PCD structure as well as its changing surface with H_2O and TDMAT exposure. 90
Figure 30: Valence band determinations from XPS spectra for (a) 100nm TiO film, (b) PCD film and (c) 2 nm TiO film on PCD; (d) represents the energy band alignment of TiO and H-terminated PCD, where CBM and VBM are conduction band minimum and valence band maximum, respectively. ΔE_V and PCD band bending, 3.06 eV and 0.13 eV, respectively, are highlighted. 93
Figure 31: Sheet resistance and resistivity graphs showing their variation with B precursor to CH_4 concentration; the effect of the B is more noticeable for B_{pre}/CH_4 values from 200 ppm. 104
Figure 32: Variation in sheet resistivity with B precursor flow rate for CH_4 rates of 3 and 5 sccm; influence on ρ_{sh} is seen for higher B flow rates. 105
Figure 33: Cross-sectional view of BDD films grown under different parameters and presented in order of increasing CH_4 flow rate and B_{pre} flow rate. 106
Figure 34: SEM surface images showing (a) 45 ^{o} tilted SEM image showing fabricated MOSFETs; (b) top-view, high resolution SEM image showing the drain, source and gate electrodes of the transistor. 107
Figure 35: (a) SEM tilted image of gate area with a volume milled by FIB to reveal the cross-section; (b) magnified SEM image of gate cross-section showing the various layers and respective thicknesses; x_1, x_2, and x_3 are approximated points on the sample where EDX analysis was performed, the results of which are shown in (c). 108
Figure 36: MOSFET characterization graphs showing (a) surface current of TiO films on BDD5 and BDD7; (b) leakage current through G of TiO-BDD5 MOSFET; (c) leakage current for 2 transistors, MOS 1 and MOS 2, fabricated from TiO-BDD7 and (d) respective drain currents for MOS 1 and MOS 2. 109
Figure 37: SEM micrographs in (a) and (b) showing the surface morphology of BDD5 and BDD7, respectively; (c) shows the topography of BDD5 with rms roughness of 86 nm. 111

List of Tables

Table 1: Comparison of O species obtained by different oxidation techniques on diamond surfaces 23
Table 2: ALD temperatures at which alumina films are deposited on diamond surfaces for the purpose of charge carrier passivation 25
Table 3: MOS devices utilizing high-κ films on diamond films 30
Table 4: Measured and calculated values for the core level and valence band BEs, E_{CL} and E_v, respectively, for determination of the valence band offset (ΔE_V) 91
Table 5: HFCVD growth conditions for polycrystalline diamond films 101
Table 6: PCD film properties, film thickness, sheet resistance and sheet resistivity 103

Abbreviations

ALD	Atomic layer deposition
AlO	Alumina films with unknown stoichiometry
B	Boron
BDD	Boron-doped diamond
BE	Binding energy
C	Capacitance
C	Carbon
CBM	Conduction band minimum
CL	Core level
CVD	Chemical vapour deposition
D	Drain
EA	Electron affinity
E_g	Energy bandgap
G	Gate
GPC	Growth per cycle
high-κ	High dielectric constant
HFCVD	Hot filament chemical vapour deposition
I_{DS}	Drain-source current
I_{DSMAX}	Maximum drain-source current
I_G	Gate-source current
κ	Dielectric constant
MOS	Metal-oxide-semiconductor
MOSFET	Metal-oxide-semiconductor field effect transistor
MCD	Microcrystalline diamond
NCD	Nanocrystalline diamond
NEA	Negative electron affinity
PCD	Polycrystalline diamond
PEA	Positive electron affinity
PDMAT	Pentakisdimethylamido tantalum
S	Source
SCD	Single crystal diamond
TaO	Tantalum oxide films with unknown stoichiometry
TDMAT	Tetrakisdimethylamido titanium
TiO	Titanium oxide films with unknown stoichiometry
TMA	Trimethylaluminum
UNCD	Ultra-nanocrystalline diamond
UWBG	Ultra-wide bandgap
VBM	Valence band maximum
V_{DS}	Drain-source voltage
V_{GS}	Gate-source voltage
V_{TH}	Threshold voltage
2DHG	2-dimensional hole gas

Introduction

Dielectric materials are electrical insulators with the ability to be polarized in the presence of an externally applied electric field. The dielectric constant (κ) of a material therefore indicates the extent of a material to be polarized, so that those with higher κ values are more susceptible to polarization than those with lower values. Typically, κ is synonymous with relative permittivity, that is, the permittivity of a material relative to that of a vacuum. The polarization of the dielectric in an electric field means that it is able to store electric charge, and it is this property that makes it particularly valuable for capacitors; κ is directly proportional to the capacitance of a capacitor.

In metal oxide semiconductor (MOS) devices such as MOS field effect transistors (MOSFETs), the role of the dielectric oxide is to increase the concentration of charge carriers in the semiconductor by its polarizability, while at the same time, as it is electrically insulating, prevent the movement of charge carriers across the MOS stack. The role of the dielectric is therefore vital to the performance of MOS devices and is made even more interesting by the variety of semiconducting materials researched today.

Diamond semiconducting films expand on the capabilities of Si devices by imparting, among other properties, a much wider bandgap, larger thermal conductivity and faster charge carrier mobility. Polycrystalline diamond (PCD), as opposed to single crystal diamond (SCD), films theoretically provide a cost-effective option for high performance electronics under thermally challenging conditions.

Thus far, the focus of research has been on the performance of SCD MOS devices, primarily with Al_2O_3. PCD, however, benefits from growth consistency over a larger area and lower fabrication costs, and the use of high-κ oxides provide possibilities for enhanced performance. MOS devices based on PCD films are lacking in literature with one of the main reasons being the challenges of surface roughness and its effects on dielectric breakdown. Pre-emptive to this, however, is the necessity for studies on the quality of high-κ layers and their interfaces with diamond surfaces, which may hold a greater understanding for their function in MOS structures.

The work presented in this thesis aims to bridge this gap in knowledge by investigating the fabrication of high-κ oxide films by atomic layer deposition (ALD) and their interfaces with PCD surfaces, for better understanding their performance in MOS devices. This will be achieved through the following objectives:

- Fabrication of alumina (AlO), tantalum oxide (TaO) and titania (TiO) films by ALD, with growth properties measured for high-κ TaO and TiO films;
- Determination of interfacial properties namely, adhesive strength and energy band alignment, of oxide films on PCD surfaces;
- Electrical characterization of B doped diamond (BDD) films grown by various parameters;
- Comparison of MOSFETs using TiO films on BDD films of different conductivities.

This research is motivated by two current trends in today's electronic devices. Firstly, the use of smaller devices and components, where the properties of thin films and interfaces are more significant to performance, and secondly, device functionality in harsh environments which include those with high temperatures and strong mechanical vibrations. It is therefore the intent of this work to be impactful for the development of functional PCD-based MOS devices utilizing high-κ oxides, for applications in harsh environments where the thermal conductivity of diamond can be advantageous.

The work is organized into 6 chapters starting with a literature review of pertinent topics and following to the studies of ALD fabrication of high-κ films, their deposition on PCD surfaces and investigation of interfacial properties. The investigative work culminates with a preliminary study of TiO-BDD MOSFETs, with general conclusions and future perspectives discussed in the 6th and final chapter. The chapters, with their primary contents and scientific contributions, are as follows:

Chapter 1: Literature Review

- This chapter provides a review of pertinent topics such as, ALD as a technique, the growth of PCD films and properties related to their conductivity, state of the art of high-κ films on diamond surfaces and diamond-based MOSFETs. It is the intent to provide an overview of both high-κ films deposited by ALD and conductive diamond films, as well as their use in concert in MOS devices.
- Contributions:
    - This chapter is a modified version of our published review: A. Jaggernauth, J. C. Mendes and R. F. Silva, J. Mater. Chem. C, 2020, **8**, 13127–13153

Chapter 2: Interface Quality of ALD Alumina Films with Polycrystalline Diamond

- This chapter studies, via nanoindentation, transmission electron microscopy (TEM), X-ray photoelectron spectroscopy (XPS) and atomic force microscopy (AFM), the differences in AlO-BDD interfaces for as-grown BDD and functionalized BDD surfaces exposed to O_2. The results demonstrated a higher propensity towards delamination of the AlO film on as-grown BDD, argued as being due to low precursor surface coverage during initial ALD cycles on the predominantly H-terminated as-grown BDD surface.
- Contributions:
    - This chapter is a modified version of our published article: A. Jaggernauth, R. M. Silva, M. A. Neto, et al, Surf. Coatings Technol., 2020, **397**, 125991.
    - *Interfacial integrity enhancement of atomic layer deposited alumina on boron doped diamond by surface plasma functionalization.* **Invited talk** at 3rd International Conference on Nanomaterials Science and Mechanical Engineering; 2020.
    - *The effect of surface functionalization on the interfacial integrity of boron doped diamond and atomic layer deposited alumina.* **Poster** presented at European Materials Research Society (E-MRS) Spring Meeting; 2019.

- *Influence of H or O terminated polycrystalline diamond on the mechanical properties of diamond/alumina coats*. **Poster** presented at 30th International Conference on Diamond and Carbon Materials; 2019.

Chapter 3: Fabrication of Tantalum Oxide Films by ALD Using PDMAT and H_2O

- This chapter studies the ALD of TaO films by XRF, XRR and XRD to determine saturation parameters and influence of ALD parameters on film properties. Depositions at higher temperatures (>260 ^{o}C) were shown to be influenced by PDMAT decomposition. Pivotal to this work is the discussion of the challenges presented by the solid PDMAT precursor, which included inconsistent heating and thus exposure during depositions, inevitably leading to GPC inconsistency. TaO films, however, were successfully achieved on PCD surfaces.
- Expected contributions:
  - Currently being formatted for journal submission with provisional title, *"Fabrication of tantalum oxide films by atomic layer deposition for use on polycrystalline diamond "*.

Chapter 4: ALD of Titanium Oxide Films and their Energy Band Alignment with Polycrystalline Diamond

- This chapter investigates saturation conditions for TiO films by ALD, using XRF, and film stoichiometry by XPS. Investigation of the energy band alignment of TiO on as-grown PCD surfaces was also carried out using XPS, to determine the feasibility of these high-κ films for use in PCD MOS devices. Both CB and VB offsets were calculated as being >1 eV but a low barrier between the CBM of TiO and VBM of PCD was also ascertained.
- Expected contributions:
  - Currently being formatted for journal submission with provisional title, *"Energy band alignment of TiO films with polycrystalline diamond"*.

Chapter 5: Fabrication of B-doped Polycrystalline Diamond Films and MOS Devices

- This final chapter of experimental reporting focuses on fabrication of BDD films under various hot-filament chemical vapour deposition (HFCVD) deposition conditions, and their resulting conductivities. Films of two different conductivities were used for MOSFETs using TiO dielectrics. TiO films displayed different conductivities on the different BDD films, such that one was insulating while the other was conductive, thus permitting leakage current. The main challenge in MOSFET performance was the lack of control of the I_{DS} current by the gate.
- Contributions:
  - *Polycrystalline diamond and high-κ dielectric films for MOS devices.* **Poster** presented at Encontro Ciencia; 2020.

Chapter 6: General Conclusions and Future Perspectives

- This closing chapter highlights the main conclusions of this thesis and suggests research actions, building from this work, for furthering knowledge in the ALD of high-κ films on PCD surfaces,

their optimization, interfacial qualities, and performance in MOS devices. These suggestions stem from the challenges discussed in the thesis as well as ideas arising from successful results.

Chapter 1: Literature Review

1.0 The evolution of MOSFET materials

Investigation of high-κ materials for semiconductor devices, especially MOSFETs, burgeoned in response to the shrinking size of electronics and even smaller size of the transistors which control them. Moore's law, observed in the 1960s and a staple in any reference to the downsizing trends in electronics[1-3], suggested that the number of transistors per square inch of integrated circuit would double approximately every 2 years thereby improving its performance, while decreasing their physical size[2]. The limitations of this trend are no longer imminent as the semiconductor industry today finds itself well below the maximum limit of the nanometre range of transistor sizes, modifying MOSFET design in addition to materials to remain competitive. This continuing shrinkage has challenged the performance of Si MOSFETs with SiO_2 gate insulators, accelerating research for high-κ gate insulators and passivation layers.

MOSFETs are common in digital circuits where they are used for signal amplification and switching. In the simplest case, a MOSFET can be regarded as a semiconductor, which may be a film or substrate, with three metal electrodes on the surface, the gate (G), drain (D) and source (S), as exhibited in

Figure 1A. The D and S electrodes are ohmic contacts. An oxide layer is deposited between the surface of the semiconductor and G electrode. The application of a voltage V_{DS} between the D and S electrodes (

Figure 1B) results in a current I_{DS} through them; a second voltage V_{GS}, applied between G and S, modulates the current I_{DS}. MOSFETs can be classified as depletion (normally-on) or enhancement (normally-off) devices. In the first case, as V_{DS} is applied I_{DS} flows and the flow of carriers can only be stopped if V_{GS} of the appropriate sign is applied. In the case of enhancement-type MOSFETs, the application of V_{GS} is required to open the channel between D and S so that carriers can flow if V_{DS} is applied. The sign of V_{GS} required to close/open the channel depends on the type of semiconductor that is, n- or p-type.

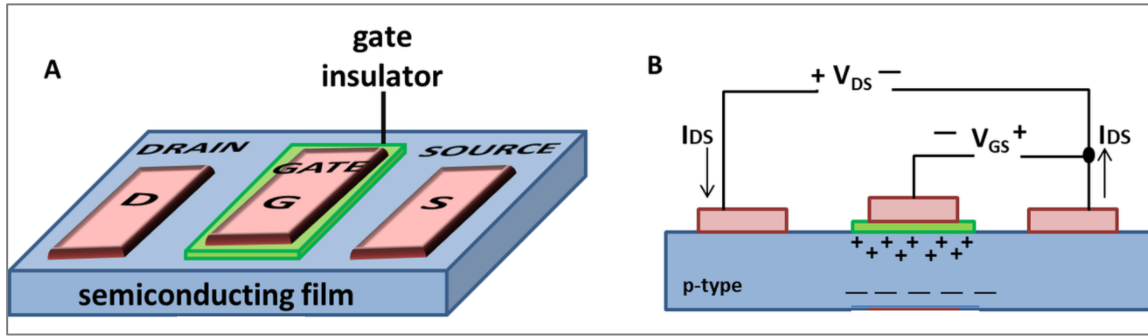

Figure 1: Schematic representations of a basic MOSFET design (A) showing the position of the gate insulator, which is an oxide layer between the gate contact and semiconductor; (B) describing the operation of a p-type MOSFET in depletion mode.

Typically, Si MOSFETs utilize SiO_2 and silicon oxynitride (SiON) gate insulators because of their ease of fabrication on Si via simple reactions with oxygen or nitrogen forming insulating films with excellent mechanical, electrical and relative dielectric properties, SiON having a higher dielectric constant than SiO_2[1]. The native oxide of Si forms an abrupt interface with the Si substrate, free from carrier-trapping intermediate electronic states, and its wide bandgap ensures a sufficiently large barrier to holes and electrons when in contact with Si[2]. The breakdown in SiO_2 insulators, and therefore MOSFET performance, arises when this layer becomes too thin and ineffective for concentrating and controlling the Si semiconductor charge carriers due to high leakage currents, that is, it fails to achieve the capacitance per unit area required for much smaller transistor sizes[1].

The capacitance (C) of the gate oxide can be estimated considering equation (1) for a parallel-plate capacitor, where A and t are the area and thickness of the oxide layer, respectively, κ is the relative permittivity or dielectric constant of the material separating the two plates, and A>>t. Following Moore's law, as devices get smaller, the area of the gate oxide decreases thereby decreasing C; reducing t, however, will prevent this decrease in C thus maintaining the effectiveness of the gate oxide, at least to its limit, which for SiO_2 is approximately 2 nm[1,4]. Replacing SiO_2 with materials of higher κ provides another avenue for achievement of the required C with a thicker dielectric/oxide layer, thus preventing the electric breakdown of the oxide and minimizing current leakage across the semiconductor-dielectric interface.

$$\frac{C}{\mathrm{A}} = \frac{\kappa\varepsilon_0}{\mathrm{t}} \qquad (1)$$

The κ value of the gate dielectric therefore becomes a principal factor for MOSFET performance but high values are achieved at the detriment of bandgap width. It was determined that gate dielectrics should possess a minimum barrier, or band offset, for both charge carriers, electrons and holes, of 1 eV in order to prevent high current leakage[5]. This factor therefore suggests an apt selection of the dielectric and semiconductor as the band offset is characteristic of this pair. The dielectric should therefore have a sufficiently high κ value to ensure control of large C and minimize leakage current due to dielectric thickness. In addition, the dielectric-semiconductor interface should render sufficiently large band offsets to prevent injection of charges across the interface. A comprehensive discussion of bandgap

offsets for various high-κ substitutes on Si, along with other pertinent considerations for material selection, have already been published in other literature[2,5].

The fabrication of these nano-thin high-κ films is facilitated by ALD, a technique which provides atomic-level control resulting in uniform, continuous and conformal nanoscale thin films. The invention of ALD is credited to two distinct methodologies, the first is the molecular layering technique invented in the 1960s in the Soviet Union by Professors Aleskovskii and Kolt'sov and the second is atomic layer epitaxy, the original name for ALD, invented by Dr. Tuomo Suntola of Finland in the 1970s for deposition of high dielectric, luminescent thin films for flat panel electroluminescent displays[6,7]. ALD is a bottom-up, layer-by-layer deposition utilizing the precursor vapour phase to deposit thin films onto a surface. It is a modification of chemical vapour deposition (CVD) in that the surface is exposed to only one precursor at a time rather than two or more at the same time as with CVD. The success of ALD for achieving nano-thin films due to control of the precursor saturating conditions makes it advantageous for use in the fabrication of MOS layers.

Limitations of SiO_2 for nanoscale gate dielectrics, spurring investigation for high-κ counterparts, have also fostered interest in alternative semiconductor materials. The abrupt interface formed by SiO_2 with Si provides consistent and reliable band alignment, preventing the movement of charges across the interface making it ideal for MOSFET applications. This advantage expires with the use of other dielectrics on Si, encouraging roles for a larger variety of semiconductors targeted for their specific properties.

Silicon carbide (SiC) is a wide bandgap (WBG) semiconductor and a contender for replacing Si in high power/high temperature electronic devices. It exhibits a larger bandgap than Si while maintaining a high-quality interface with SiO_2 substantiating its use in higher power applications of Schottky barrier diodes (SBD) and MOSFETs[8]. Gallium nitride (GaN) and other III-V semiconductors boast superior electron mobility and bandgaps that are both wide and direct with the possibility of amenability[9], GaN is utilized in power devices, solid state lighting and optical devices, and its wide bandgap permits short wavelength emissions[8]. Reviews of impactful semiconductors are many and for each application there are combinations of elements and buffer layers for enhancing performance[8–12]. Literature has also unveiled the many semiconductors fabricated by the ALD technique, being especially advantageous for two-dimensional nanoscale semiconductor films[3,13]. In addition, distinctions are being made between WBG and ultra-wide bandgap semiconductors (UWBG), the latter identified as semiconductors having bandgaps much wider than GaN's 3.4 eV, and include diamond, gallium oxide (Ga_2O_3), aluminium gallium nitride (AlGaN)/AlN and cubic boron nitride (BN)[9].

UWBG materials such as Ga_2O_3, cubic BN, AlGaN/AlN and diamond are now at the forefront of semiconductor research due to their very high breakdown electric field, charge carrier mobility and carrier saturation velocity compared to their narrower bandgap counterparts[9,14]. Diamond proves especially interesting coupling these properties with an extremely high thermal conductivity, 2290-3450 $Wm^{-1}K^{-1}$, allowing its devices to withstand high voltages, operate at high frequencies, efficiently transfer heat and operate under extreme conditions[9,15]. Extreme or hostile environments are associated with various industries and includes those having high temperatures (350-1000 °C), high pressures (>1000 atm), extreme mechanical vibrations, high radiation, corrosive media and electromagnetic interference,

in which mechanical and electronic properties of semiconductor devices and dielectrics can be compromised and their overall operation made unreliable or impossible[9].

The principal issue that plagues diamond's rise to end use eminence is its relatively high cost, especially compared to easily fabricated and readily available Si, and scalability. Other issues have also been raised such as the numerous defects present in diamond substrates, high activation energy required for conductivity in BDD due to deep acceptor levels, and reliability of behaviour for electrical applications[8,16]. Investigations of SCD for MOS devices are far more frequent than for PCD. The former minimizes the effect of an inhomogeneous film on electrical properties, as defects can persist in SCD films, while the latter provides a cost effective and scalable option for reducing the effect of heat in devices, increasing their efficiency. Recent literature more specific to application-oriented reviews on diamond based MOS devices can be found in these references[17,18].

The advantages of diamond at this time outweigh its challenges, favouring its use in MOSFETs for niche applications in harsh environments and for addressing issues of heat in devices. PCD MOSFETs comprise a nanometre-thick dielectric layer between the gate contact and diamond film to contain current flow in the semiconducting PCD film and prevent its leakage through the gate. The fabrication of both films therefore needs to be optimized for their individual roles and realization of a high-quality interface suited for the targeted electrical performance. It is the intent of this chapter to highlight pertinent parameters and considerations for the optimization of PCD films and of high-κ oxides, which include Al_2O_3, HfO_2 and TiO_2, by ALD onto these films, specifically for use in MOSFETs. Generally, diamond-based MOSFETs are characterized by electrical properties but from a materials engineering point of view, variations or discrepancies in these properties can be explained by low interface quality especially with oxide films of thicknesses <10 nm, where the effect of defects can be magnified and the movement of charge carriers across interfaces is more difficult to control. It is therefore important to first understand the surface chemistry and morphology of PCD films, reactions between ALD precursors and surface ligands during initial cycles, and manipulation of surface chemistry, towards the achievement of higher quality interfaces for optimized device performance.

2.0 Atomic layer deposition (ALD)

2.1. ALD Technique

ALD has been used to fabricate a variety of thin films the most noteworthy for microelectronics being metal oxides for high-κ materials in semiconductor devices[7,19], although metals and nitrides have also been deposited as electrodes for gate stacks, and interconnects[4,7,20], and sulphides are gaining momentum in ALD for the fabrication of semiconductors for energy storage applications[13,19]. Reviews have already cohesively tabulated the extensive array of materials deposited by ALD along with their respective precursors, including those falling into these categories[3,19,21]. A more recent review has elucidated and discussed issues related to reproducibility of film properties, and misconceptions about technique behaviour[22]. Relevant to this work however the focus will remain on ALD of high-κ materials for semiconductor devices.

ALD is a bottom-up deposition technique utilizing interchanging of precursors in vapour phase to deposit atomically thin films onto a surface. This interchange of precursors, separated by a purging step with an inert vapour, ensures the deposition of one layer of adsorbed precursor at a time, resulting in film proliferation layer-by-layer. In a typical binary metal oxide deposition two precursors are used, a metal source and an oxygen source, this is depicted in Figure 2 for ALD of Al_2O_3 using trimethylaluminium (TMA) as the metal precursor and H_2O as the oxygen precursor, the reactivity of which has been comprehensively studied in literaure[21,23-25]. ALD proceeds in cycles with each half-cycle resulting in a change in the surface species signalling the addition of a new layer. One cycle is defined by first purging the chamber with an inert gas such as N_2, followed by exposure to the first precursor, purging again, and then exposure to the second precursor (Figure 2). The number of cycles used in ALD determines the thickness of the deposited layer. Purging between precursor exposures enlightens to the fact that mixing of precursors is forbidden in ALD, in contrast to CVD processes.

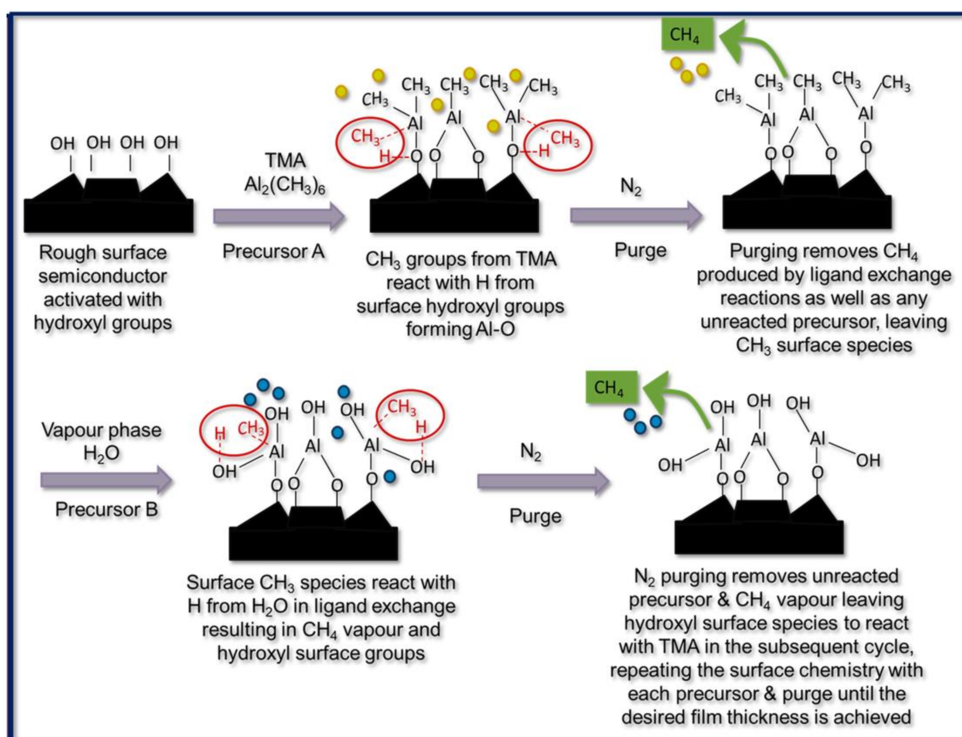

Figure 2: Representation of one ALD cycle for Al_2O_3 using precursors, trimethylaluminium (TMA) and water. This process is prevalent in literature, typically starting with hydroxyl-terminated surfaces. Purging prevents mixing of precursors by removing any unreacted precursor and by product molecules formed from precursor-surface reactions.

To achieve the desired thin film, typically defined by characteristics such as stoichiometry, thickness, and crystallinity, there needs to be an understanding of the ALD parameters and how they affect the precursors and the substrate. This is imperative as not all ALD systems display ideal behaviour with factors such as substrate type, surface functionalization and topography, and deposition temperature, precursor temperature, pulse and purging durations all affecting the resulting film. Assuming that self-limiting and saturating conditions are achieved for a particular planar surface,

changes in surface functionalization and roughness may require additional tuning of deposition parameters.

2.2. Main Parameters

2.2.1 Pulse and purge durations

The reaction between precursor molecules and surface sites should be saturating and self-limiting. Saturation ensures that all possible sites available for precursor reactions do indeed react, and once all the available sites are filled the precursor ceases to react with any other species, including itself, thus describing a self-limiting reaction. It should go without saying that surface reactions must be irreversible in order to be self-limiting and result in saturation. ALD parameters must therefore reflect that no further precursor reactions could occur with surface sites, and any available unreacted site is due only to steric hindrance that is, blocking of available sites by the ligands of the reacted precursor[21]. The likelihood of this occurrence has been shown to increase with size disparity between molecules of the two reacting precursors[26].

Saturation is governed by the amount of precursor species a substrate receives from a precursor pulse or the impingement flux, and the net exposure to this species over the duration of that pulse[27]. The net exposure, Q, in molecules/m^2, is described by equation (2) from the Knudsen equation considering an ideal gas, and is the integral of the molecular impingement flux for the pulse duration[27]. M, T and p are the molar mass, temperature and partial pressure of the precursor species, respectively, while N_A and R are Avogadro's constant and the universal gas constant, respectively. A specific precursor with constant M at constant temperature would therefore have a partial pressure that is time dependent such that the amount of precursor, or dose, introduced to the substrate is achieved by controlling only the precursor pressure, which is in turn controlled by the pulse duration, for a fixed chamber volume[27]. The pulse duration therefore determines the amount of precursor species impinged onto the sample surface and its resulting ability to saturate available sites.

$$Q = \int_{t_i}^{t_f} \frac{N_A}{\sqrt{2\pi MRT}} \, p \, dt \qquad (2)$$

Typically, saturation is proven by analysis of the growth per ALD cycle (GPC) with changes in precursor pulse duration, performed for each precursor in the ALD process at constant deposition temperature[28-30]. The achievement of a constant GPC, irrespective of pulse duration, signals the occurrence of precursor saturation (Figure 3A), as exposure to more species does not result in more surface reactions. The range over which constant GPC is obtained is unique to the precursor for the deposition temperature used. At short pulse durations, if the surface is not fully saturated, it may be due to low pressure and few available species for surface site reactions. The species of subsequent precursor exposures then fill remaining available sites on this initial surface and on the few isolated areas of growing film from sites which have reacted, typically called islands, rather than contribute to the uniform thickness of the film[21,31]. In such a case, unsaturated conditions would result in a lower GPC due to the deposition of a thinner film than that formed under saturated conditions for the same number of cycles[28-30]. Increasing precursor pulse durations would then result in a higher pressure and greater

number of species in the gas phase, reacting with more of the surface sites in each cycle and increasing the GPC. Eventually an increase in the pulse duration will cease to increase the GPC as all available surface sites react with the precursor species produced by the pulse, completely saturating the surface. This is graphically represented in Figure 3A. The bonding of precursor species to the surface can also be measured as an increase in mass and can also be an indication of saturation. The use of a quartz crystal microbalance (QCM) in situ, which measures the mass signal during exposure and purging, can therefore be used to confirm precursor deposition behaviour; saturation is shown by a constant mass increase per cycle[32].

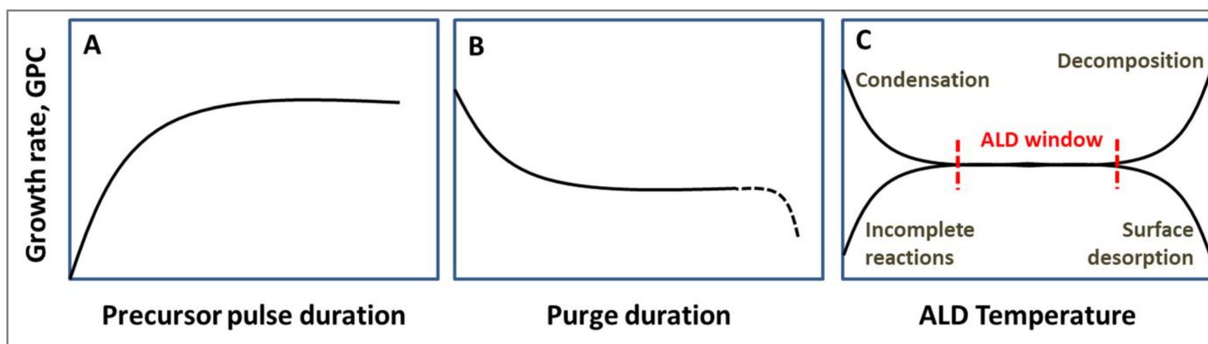

Figure 3: Graphical representations of saturation and self-limitation in ALD reactions investigated by changes in growth per cycle (GPC) with (A) pulse duration of precursors, (B) purging duration and (C) deposition temperature. Constant GPCs exhibit regions of saturation and self-limitation, the ALD window exhibits the temperatures over which precursor reactions with the surface are ideal[23,29,30].

Purging between precursor exposures is also a consideration of saturation as it affects the mass deposition on the surface and hence the GPC. Purging with an inert gas such as N_2 prevents mixing of the precursors prior to reactions with surface sites, thus preventing CVD reactions, so that sufficient purging durations will be manifested as a constant GPC and maintain saturating behaviour[29,30]. Insufficient purging times were found to influence film thickness, uniformity and chemical composition. Non-uniform films were noticed for ALD of HfO_2 and ZrO_2 for purge times below a respective minimum, being thicker at the area of the reactor entrance and thinner at its exit; interestingly, increasing the purging times beyond the minimum required for saturation at higher temperatures resulted in the removal of chemisorbed precursor species[33], identified by the broken line of Figure 3B. Precursor adsorption is explained as being due to both chemisorption with surface sites and physisorption of unreacted precursor at the surface, a short purging time can therefore remove gaseous precursor but not the physisorbed species, which can then react during subsequent cycles, resulting in a higher GPC[33,34] (Figure 3B). Purging durations should therefore be investigated for saturation as precursor pulse durations alone may not sufficiently explain the precursor kinetics.

Together with saturation, self-limitation needs to be achieved for ALD to be fulfilled. Self-limitation occurs when the precursor molecules react only with the available surface sites and not with themselves, even after saturation has been achieved. Unreacted precursor molecules remain in the gaseous phase and are removed from the chamber via the purging step in the ALD cycle, preventing interaction between precursors prior to surface reactions. Similar to saturation, self-limitation can be demonstrated by a constant GPC with precursor pulse duration[35] as deviations from this can be due to

precursor self-reactions or decomposition, so that while saturation has occurred on the surface sites, continuous reactions of the precursor with itself will increase the GPC. Self-limitation can also be observed when a constant GPC is achieved with deposition temperature (Figure 3C); further discussion of this ensues in the next section dedicated to deposition temperature.

2.2.2 Deposition temperature

The deposition temperature is that set and maintained in the ALD chamber. Generally, depositions are performed at modest temperatures, below 350 ^{o}C[19], but temperatures below 100 ^{o}C are used in cases where higher temperatures may alter sample surface groups, decompose the sample or precursor, or where ALD is utilized as an energy efficient option[30,36,37]. The ALD window is the temperature range in which ALD reactions are self-limiting and saturating, and typically a consistent GPC is achieved (Figure 3C), although this may not always be the case. Temperatures above or below this range are shown to alter the characteristics of the deposited film, increasing the temperature may result in a loss of self-limitation, which can occur due to decomposition of the precursor at higher temperatures, facilitating additional adsorption, or desorption of surface species, resulting in lower GPC[23,30,35].

Low temperature plasma enhanced ALD (PEALD) was investigated for AlN deposition in the range 100-200 ^{o}C resulting in a constant growth rate of 0.86 Å/cycle[30], while AlN films from trimethylaluminium (TMA) and NH_3 demonstrated a change in growth rate from 0.05 to 0.16 nm/cycle with a change in deposition temperature from 274 to 335 ^{o}C[38]. It was suggested that TMA self-decomposition occurred at these higher temperatures preventing self-limitation[39], but NH_3 surface reactions required these high temperatures, which could be circumvented by the use of NH_3 plasma[30]. This permitted a lower temperature for TMA surface reactions without self-decomposition, resulting in self-limiting reactions[30]. The role of deposition temperature is therefore two-fold, providing the optimal conditions for surface reactions but also maintaining the precursor molecule in a vapour phase without self-decomposition. This ensures that film proliferation is due only to surface reactions, typically ligand exchange, association or dissociation reactions[21], facilitated by the deposition temperature.

Deviations from a constant GPC for defining the ALD temperature window have been experimentally demonstrated and discussed in literature[22]. TiO_2 films, for example, resulting from tetrakisdimethylamido titanium (TDMAT) and H_2O precursors, described the tendency of a decreasing growth per cycle (GPC) with increasing temperature; saturating reactions were, however, confirmed by the achievement of a consistent thickness with an increase in Ti precursor pulse time[40-42]. This occurrence of a non-constant GPC in the ALD window was explained by a decrease in the number of surface sites with increasing temperature, so that saturation occurred for all the sites, although being fewer as temperature increased, resulting in a decreasing GPC[40,42]. It is therefore possible to have an ALD window which is not defined by a constant GPC but rather by the occurrence of surface saturation reactions.

2.2.3 Precursor temperature

If necessary, precursors can be heated in order to achieve a vapour phase, as they may exist in a solid or liquid form. Ta precursor tert-butylimido-tris-ethylmethylamido Ta (TBTEMT), a liquid at

room temperature, have been heated to 60 ^{o}C in order to obtain a suitable vapour pressure for ALD of Ta_2O_5[29]. Pentaethoxytantalum (PET) also a Ta precursor was heated to 160 ^{o}C in order to achieve sufficient vapour pressure in ALD of Ta_2O_5 films for use in metal-insulator-metal capacitors[43]. Custom complexes such as tetrakis(N-*tert*-butylacetamido) Zr and tetrakis(N-isopropylisobutyramido) Hf developed for enhancing the thermal stability of Zr and Hf precursors, respectively, are colourless crystalline solids which undergo sublimation between 130 to 140 °C at 6.67 Pa and have therefore been suggested for use in ALD[44]. Heating of precursors is performed with knowledge of their phase transition temperatures as their decomposition can occur when temperatures are too high.

In the development of new precursors better targeted for ALD growth of structures with high thermal stability, low impurity concentration and deposited at high growth rates, both sublimation or boiling temperatures and decomposition temperatures are investigated due to their pertinence to precursor reactivity. Decomposition temperature describes that at which a precursor no longer holds its chemical bonds and therefore does not react with surface ligands predictably for ALD reactions to form the desired chemically uniform structure. This temperature becomes important for selection of vaporization or deposition temperatures as it can lead to precursor decomposition upon vaporizing or upon reaction with the surface sites, for example, low reactivity between precursor and surface sites can be alleviated with increasing deposition temperature but this can then lead to the decomposition of the precursor[45].

Zr and Hf precursor complexes based on tetrakis(N-*tert*-butylacetamido) Zr and tetrakis(N-isopropylisobutyramido) Hf, respectively, exhibited thermal decomposition at temperatures >300 ^{o}C with lower sublimation temperatures between 130-140 ^{o}C, encouraging their use in ALD, owed to their vaporization without decomposition[44]. Different complexes based on the Zr precursor were however seen to have lower decomposition temperatures 218-263 ^{o}C and, although sublimation temperatures were lower, 130 ^{o}C, they still exhibited decomposition upon sublimation, attributed to the presence of smaller groups or atoms on the core atoms, as bulky groups on the core atoms provided thermal stability of the precursor[44]. Evidence of precursor thermal decomposition was demonstrated by an increase in GPC for ALD of Ta_2O_5 at temperatures >275 ^{o}C, using precursors $Ta(NtBu)(NEt_2)_3$ and H_2O[45]. Precursor temperature is therefore not only considered in ALD for achieving vaporization but also to prevent decomposition, while also ensuring sufficient temperatures for surface reactions. This ensures that the precursor achieves the vapour phase and is supplied with sufficient energy to react with surface sites without thermal decomposition.

3.0 Polycrystalline Diamond Films (PCD)

3.1 PCD film growth

The mechanisms involved in the growth of diamond films have already been reported in literature with much exploration into the parameters which result in the achievement of particular morphological, mechanical and electrical properties[15,46-50]. This is due to the popularity of diamond in a variety of applications such as mechanical tool coatings, electrochemical applications and

microelectronic devices. What follows therefore is a synopsis of the HFCVD technique used for achieving PCD films, as well as a discussion of pertinent factors which may theoretically result in more consistent and reliable film conductivity.

Low pressure fabrication of diamond films can be achieved by one of the many types of plasma assisted CVD techniques such as those performed using microwaves (MPCVD)[51], and hot filament enhancement, HFCVD[51,52]. MPCVD generally results in high growth rates and film quality due to its high efficiency in dissociating precursor gases from the molecular to atomic species necessary for achieving the diamond structure[48]. HFCVD is economically beneficial with a thermal activation process enabling ease of use and understanding of the growth mechanism. It results in decent quality microcrystalline and nanocrystalline films, determined by the figure of merit (FOM) obtained via analysis of the Raman spectrum and the ratio of the sp^3 diamond C band around 1332 cm^{-1} compared to the non-diamond bands[53]. Most recently, heavily B doped free-standing diamond films were grown by HFCVD at a relatively high growth rate of 4.2 μm/h[51]. In addition, B incorporation into HFCVD grown (100) SCD was suggested to be more efficient than that for MPCVD due to the shorter lifetime and migration length of B admolecules during the latter caused by a higher atomic H flux and surface etching[54]. These examples demonstrate the continued validation of HFCVD for B doped PCD film growth.

HFCVD utilizes metal filaments with high melting temperatures, such as tungsten (W), Ta or rhenium (Re), heated using a power supply, to temperatures >2000 ^oC. The chamber is first evacuated, then gases pertinent to BDD film growth are introduced into the chamber, maintaining a desired pressure. H_2, CH_4, are generally deemed necessary for diamond film growth, a B precursor is utilized for p-type doping and Ar is typical in polycrystalline systems for decreasing grain sizes. The hot filaments have two purposes, to dissociate the incident gas species to achieve atomic hydrogen, hydrocarbon radicals and B admolecules, schematized in Figure 4, and to create a high temperature gradient near the growth substrate resulting in a non-equilibrium gas phase close to its surface. The use of atomic H is particularly important for diamond growth since diamond, compared to graphite, is more stable towards atomic H which etches graphite (sp^2 C) much faster than diamond (sp^3 C), supressing the nucleation and growth of graphitic structures[15,48]. Atomic H also allows for the maintenance of the sp^3 hybridization configuration and the proliferation of the diamond structure by inducing sites onto which precursors can be adsorbed[48]. In general, growth temperature, pressure and gas concentrations are the principal parameters affecting the diamond structure and composition during HFCVD growth.

Generally, CVD grown diamond films comprise not only sp^3 diamond but sp^2 graphite, amorphous carbon, polyacetylene, and sp^3 diamond-like carbon are also incorporated during growth, their concentrations being dependent on the resulting diamond grain sizes[52,55,56]. The ranges of grain sizes which define categories of diamond films are ambiguous in literature, possibly because of the range of sizes that can be present in one film. Microcrystalline diamond (MCD) is defined for grain sizes 200-2240 nm but also more generally >1 μm[47,57]; nanocrystalline diamond (NCD) is defined for grain sizes <100 nm but has also been used to describe films with grains up to 500 nm and in the range 10 nm to 1 μm[47,58]; finally, ultrananocrystalline diamond (UNCD) is generally defined in the range <10 nm or <5 nm[47,58]. The resulting grain sizes comprising the film are dependent on growth temperature and relative concentrations of precursor gases[48], UNCD is grown in H poor and Ar rich environments while MCD is the result of growth in H rich environments with minimal to no Ar[48].

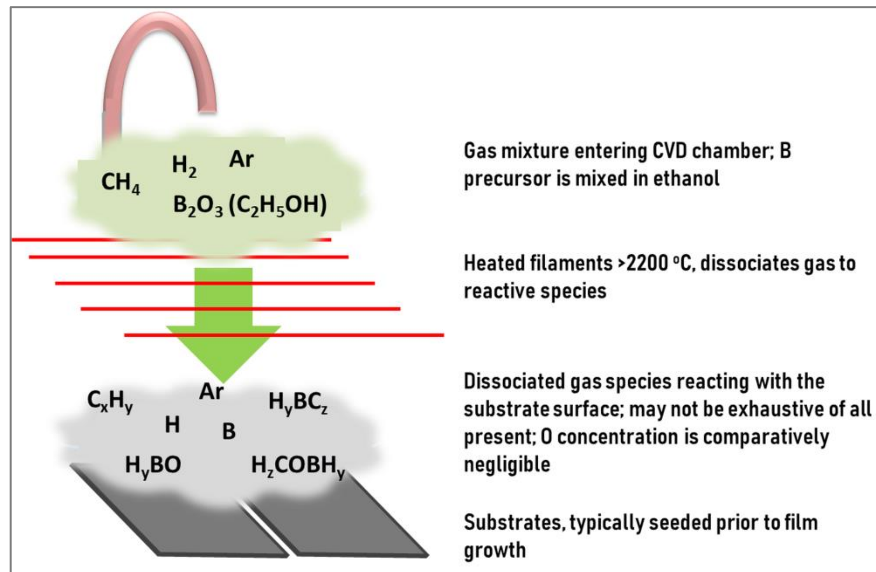

Figure 4: Schematic of HFCVD technique to produce the gas species contributing to B doped diamond growth; the image is based on literature investigating both theoretical and experimental findings[48,59]. The gas molecules are dissociated to a reactive species upon exposure to heated filaments, which allows them to react with the seeded surface resulting in growth of sp^3 diamond.

PCD films with grain sizes ranging from NCD and MCD in the same film are therefore more accurate representations of the films in this work. Optimization of PCD films to realize their theoretical potential and display targeted behaviours has been the focus of more recent research[9,16,46,47,60]. This is because the manipulation of diamond film properties solely for electronic applications can be performed over a variety of factors including sp^3 diamond content, dopant concentration, grain sizes, film thickness and surface termination, all of which can be tuned by nucleation and growth parameters. Complexities arise however as tuning can result in competition among factors and the properties which they influence. Diamond thin films utilized for the desired MOSFETs can benefit from fabrication parameters which optimize their semiconducting behaviour, efficiency in thermal and electronic conductivity, and breakdown field. In addition, these properties should not be undermined when the film is coupled with other materials such as the gate dielectric.

3.2 Diamond film conductivity

3.2.1 Surface and bulk conductivity

Diamond film conductivity is the result of two contributions, bulk conductivity due to dopant incorporation, and surface conductivity due to the presence of a 2-dimensional hole gas (2DHG) formed by adsorbates on H ligands terminating the diamond surface[61]. The latter asserts that it overcomes the problem of the high activation energy required for dopant conductivity in the bulk, which can be ignored if the surface carrier density and mobility are significantly higher than those of the bulk[61].

Diamond surface conductivity is generated from adsorbates on an H-terminated surface, and explained via a transfer doping mechanism whereby electrons from the diamond are transferred to unoccupied states in the surface adsorbate layer leaving behind holes in diamond just under its surface, thus forming a conducting p-type 2DHG or space charge region[60,62,63]. Electron transfer is instigated by modulation of the electronic energy levels at the adsorbate-H-diamond interface, due to the higher electron affinity (EA) of the adsorbates, and therefore stronger attraction, compared to the negative EA (NEA) of H-diamond[62,64]. EA is defined as the energy difference between the conduction band minimum (CBM) and the vacuum level. The lowest unoccupied molecular orbitals (LUMO) in the adsorbed species facilitate the movement of electrons from the valence band maximum (VBM) of diamond, filling these unoccupied levels until equilibrium, identified by Fermi level alignment across the interface, is achieved[60,62,64,65]. Equilibrium charge concentration was reported as being influenced by the area density of molecular adsorbates, and the energy separation between the LUMO of adsorbates and the VBM of diamond[62].

Surface H ligands as well as adsorbates are necessary for this surface p-type conduction but, for adsorbates from air, over time and with temperature increases, hole concentrations decrease[60,64,66]. Solutions to this occurrence have spurred investigation into the exposure of H-diamond surfaces, subsequently annealed to remove adsorbates from air, to gases such as NO_2, NO, SO_2 and O_3[60,67,68]. Additionally, ensuing efforts have explored the fabrication of passivation layers to stabilize surface adsorbates, and therefore charge carriers, utilizing high-κ films such as Al_2O_3 and HfO_2[61,63,69]. Another strategy for enhancing surface conductivity involves the incorporation of transition metal oxides (TMO) with high EA such as, MoO_3, V_2O_5, WO_3, and Nb_2O_3[64,70,71], on the H-diamond surface. These employ an insulator transfer doping mechanism via electron transfer from diamond to the high EA insulators, and subsequent Fermi alignment which occurs when the diamond and insulator are in contact[64]. Further discussion about these techniques for creating and enhancing surface conductivity can be found in these references[60,63,64].

Diamond film conductivity can also be achieved through the introduction of dopants in the bulk by techniques such as ion implantation and integration during diamond growth via the addition of a dopant precursor to the gas mixture. B, P and N have been used as dopants in diamond films; B introduces p-type acceptors (holes) while P and N provide n-type donors (electrons). Conductivity is achieved as the dopants establish mid-gap states in the diamond bandgap thereby facilitating the movement of the respective charge carriers from the VB or conduction band (CB) depending on the dopant used. These mid-gap states are associated with the activation or ionization energy required for the movement of the charge carriers from substitutional dopants in the tetrahedral diamond structure; in the case of B this energy is 0.36 eV, relatively shallow compared to 0.57 eV for P and 1.7 eV for N[9,47,57,63].

Doping of diamond films with B is ubiquitous in literature, both for surface and bulk conductivity. B as a dopant is incorporated as a substitutional atom in the diamond structure. At high doping concentrations there is significant overlap of the excited states of B atoms, forming an impurity band in contact with the top of the VB, omitting the need for thermal activation; metal-like behaviour, beneficial for electrode applications, is therefore demonstrated when heavily doped ($>10^{20}$ B atoms cm^{-3}) and p-type semiconductor behaviour is exhibited when lightly doped (10^{19} B atoms cm^{-3})[47,72,73]. It is worth noting that film conductivity is not linearly proportional to B concentration, and at concentrations

>10^{21} cm^{-3} BDD film conductivity was shown to decrease due to a lowered hole mobility (Figure 5), explained by the formation of B dimers (B-B), as opposed to single B substitution defects formed at lower dopant concentrations[73]. B dimers possess high acceptor energies which again hinder ionization from the valence band to the dopant level[73] suggesting that indefinite increases in the B dopant will not result in more conductive films. B incorporation into diamond films has been determined by techniques which include: Hall effect measurements, also used for hole mobility characterization, neutron depth profiling (NDP), and secondary ion mass spectroscopy (SIMS)[73-76]. The presence of B can also be confirmed by Raman spectroscopy with signals near 500 and 1200 cm^{-1} [72,73,77,78]. The use of these and other characterization techniques such as infra-red (IR) spectroscopy and electron energy loss spectroscopy (EELS) have identified a preferential incorporation of B, for both PCD and SCD films, into {111} and {110} crystal orientations compared to {100}, in some cases exhibiting a difference in B concentration of at least one magnitude[50,79,80].

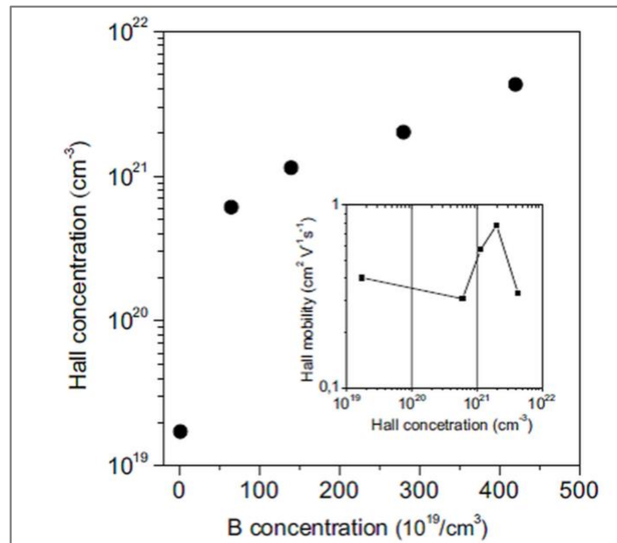

Figure 5: Graph of Hall concentration vs B concentration for MPCVD grown BDD films, where Hall concentration is considered to be a reflection of free hole concentration inside the BDD grains, so that for larger B concentrations the hole concentration is shown to be lower than that for atomic B. The inset graph demonstrates that a lower hole mobility occurs for the most doped sample, attributed to compensation of B acceptor atoms most likely by B incorporation by B-B dimer formation. The highest hole mobility is observed for B doping resulting in a metallic-state film as a result of a high concentration of B acceptor atoms [reprinted by permission from Springer Nature Customer Service Centre GmbH: Springer European Physical Journal (EPJ) from reference[73], Copyright (2013)].

The challenge of substitutional doping lies principally in overcoming dopant activation energies, especially at room temperature where charge carrier densities are low but increase with temperature[63]. Specifically for MOS devices, the application of high applied bias voltages at room temperature is necessary to overcome the activation energy to achieve inversion in the film which consequently may induce early breakdown of the oxide layer[81]. Dopant activation energy is also problematic for fast switching applications whereby insufficient time is given for movement of charges in the film to achieve inversion thus realizing low performance devices due to high apparent film

resistivity. Efforts are therefore made to concentrate film conductivity at the surface or close to the surface by utilizing surface terminations and adsorbates, and dopant incorporation in film layers close to the surface.

3.2.2 PCD film conductivity

The homogeneity of SCD films contributes to their dependability via minimization of variables affecting their performance and as such they have been the focus of power devices[16] as opposed to heterogeneous PCD films. In either case however film properties are defined by film quality that is, the presence of high quality sp^3 diamond, usually determined from Raman spectroscopy analysis by considering the ratio of sp^3/sp^2 film content[53,56,82]. The disadvantages of SCD include its high production cost, limitations to large area growth due to restricted crystal size, the presence of dislocations due to strain induced by B doping, and poor-quality diamond due to dislocations and soot incorporation during long growth durations[16,83,84]. Alternatively, PCD is more economically produced and can be grown on large area Si substrates with high quality sp^3 diamond content, and its lower performance as a power device compared to SCD is still sufficiently high that it remains a contender[83,84].

Surface conductivity of PCD films provides yet another advantage to their use, attested to result in high sub-surface charge densities due to their varied grain orientations and presence of grain boundaries[85-87]. (110) preferentially oriented films displayed higher C-H bond densities, compared to preferentially oriented (001), leading to higher sheet carrier density and lower sheet resistance[87]. In addition, other research determined that H bonding in PCD films increased with decreasing grain sizes between 20 – 300 nm, indicating that H is most likely bonded to C and trapped in grain boundaries[86].

PCD heterogeneity also affects the surface ligands and subsequent chemical bonds that determine the effectiveness of films deposited on the PCD surface. In addition to sp^3 diamond, non-diamond phases such as sp^2 graphite, amorphous carbon, polyacetylene, and sp^3 diamond-like C, are all incorporated into PCD films during growth by CVD techniques[52,55,56]. To this extent, varied PCD film composition and diamond crystal orientation serve as origins of possible selectivity toward chemisorption of the coating species; H-terminated diamond exhibits hydrophobicity, hindering reactions with H_2O oxidants and sp^2 graphite phases which, much like graphene, can manifest as inert areas due to their lack of dangling bonds[88,89]. In the application of MOS devices, discrepancies in surface bonding can result in current leakage and charge trapping due to poor interface quality[2], knowledge of the film surface ligands, or lack thereof, is therefore necessary to determine phases that may lead to selectivity and, in so doing, prevention of these undesirable effects.

As-grown diamond films demonstrate dominant H ligands at the surface mainly due to their cooling in H environment subsequent to high temperature growth. XPS and HREELS analyses of as-grown PCD surfaces have shown the presence of sp^3 C-C bonding and sp^2 C-C or π-bonded C, contributions from the bulk film, with sp^2 C originating from grain boundaries and non-diamond phases[90,91]. The surface terminations are mainly due to CH_X (x = 2, 3) bonds (H-terminations), with smaller contributions from C-O bonding possibly from C-OH, C-O-C, C-O-O-C, and trace amounts of carbonyl and carboxyl groups[90-92]. O surface terminations are therefore present on as-grown diamond films but have been shown to be reduced with thermal cleaning treatments[90,91], the presence of prevailing O species subsequent to treatments have been explained by surface oxidation due to atmospheric exposure or existing as residuals in the graphitic phases[90,91]. Other research has also identified O at the

surface and sub-surface layers of as-grown PCD films as a result of O in the gas mixture from the B precursor B_2O_3[53]. The dominant H-termination of as-grown films will diminish over time but may be restored by H plasma treatments[93-95]. Surface ligand manipulation is also dependent on diamond grain orientation, especially pertinent to PCD films and is discussed primarily for O-terminations in Section 4.2.

4.0 ALD of High-κ Films on Polycrystalline Diamond

4.1 High-κ Film Nucleation

A practical consideration of ALD especially pertinent to its use for fabrication of gate dielectrics and passivation layers on PCD films is that of nucleation, that is, the reactions occurring during initial ALD cycles. Nucleation is dependent on reactions between precursors and substrate sites, which are ideally self-limiting for ALD. In reality, however, initial cycles result in the formation of multilayer islands which eventually coalesce to form a continuous film, signifying the occurrence of non-linear growth at the start of deposition[3,96], a challenge for achieving uniform films of thicknesses <10 nm. Nucleation on heterogeneous surfaces such as those of PCD is further complicated by the variety of surface species due to crystal orientations, grain boundaries and the incorporation of dopants, so that optimization of self-limiting behaviour, through the choice of precursors and ALD parameters[3], may first require a surface functionalization step. It should be noted that the nucleation of high-κ films on PCD has not been addressed in literature, possibly because of the difficulty in determining the presence of a few atoms on an already heterogeneous surface, although this type of investigation is also lacking for SCD films, the opportunity thereby existing to bridge these gaps.

Examples of incubation periods during initial ALD cycles are frequent in recent literature, with in situ and surface characterization techniques being used to gain further understanding. ALD ZnS films on Au were studied using in situ scanning tunnelling microscopy (STM) which demonstrated that at a temperature of 160 ^{o}C islands were formed during the first 3 cycles before a continuous film was realized[97]. Room temperature deposition, however, resulted in mobile physisorbed precursor molecules on the Au surface for at least 3 cycles, with measurements for subsequent unable to be realized[97]. This result highlights the influence of the deposition parameters to minimize the effect of non-linear growth rates during initial cycles[97]. Fabrication of TiO_2 films on Si by ALD at 150 ^{o}C was also studied by in situ STM which determined that island formation occurred during the first 15 cycles before the realization of a continuous film[96]. TiO_2 films deposited on H-terminated Si at 170 ^{o}C using a 'water free' ALD process also highlighted selectivity in growth during initial cycles where Ti was detected by XPS after 5 cycles but remained unchanged for about 80 cycles, after which an increase in signal was detected, although steady state growth was not recognized until 200 cycles. This was explained by the presence of localized Cl on the surface, from the $TiCl_4$ precursors, having reacted with defect sites and forming a passivation layer, inhibiting growth for a few cycles[98]. ALD Al_2O_3 on H-terminated Si at 300 ^{o}C was characterized by TEM and the images showed the presence of Al_2O_3 islands even after 15 cycles and a closed film after 30 cycles of thickness 2.1 nm[31]. It is also worth noting that the sensitivity of the

characterization technique is also an important consideration for determining the occurrence of initial incubation periods resulting in islands with such small sizes. XPS was shown to be insufficiently sensitive to the presence of TiO_2 on H-terminated Si deposited after 35 cycles, although island formation was confirmed by STM after 15 cycles[96].

To curtail the issues of island growth and selectivity in surface reactions, research has addressed techniques of pre and post treatments. Surface treatments prior to ALD has been undertaken to increase the number of surface sites or ligands to enhance nucleation while post annealing treatments have been used to bring order to the atoms of the deposited film thereby removing impurities and improving interface quality.

4.2 Manipulation of Surface Terminations

Surface termination techniques have been used to promote more uniform growth during initial cycles, or at least minimize the number of cycles for nucleation prior to the formation of a closed, continuous film, although achieving linear growth during this stage remains a challenge. H-terminated surfaces of Si and Ge have been shown to be relatively inert to reactions with TMA and H_2O, precursors for Al_2O_3, evidenced by lower GPC rates during the first few ALD cycles which resulted in the formation of islands of Al_2O_3[31,99]. Island formation was attributed to reactions between TMA and surface O defect sites and dangling bonds rather than with the H surface species[31,99]. Exposure of the H-terminated Ge surface to an O_2/Ar plasma resulted in the formation of a GeO_x surface layer which facilitated pronounced TMA adsorption, forming an Al_2O_3/GeO_x intermixing layer and a completely coalesced Al_2O_3 layer[99]. The nucleation however was still determined to be nonlinear although not to the extent as exhibited with the H-terminated sample[99]. TiO_2 deposition on H-terminated Si and OH-terminated Si using $TiCl_4$ and Ti tetraisopropoxide demonstrated greater selectivity towards the OH surface compared to the H surface. XPS measurements detected a definitive Ti 2p signal on the OH surface after 5 ALD cycles, while a weak signal was observed on the H surface after 5 cycles but only readily discernible after 50 cycles[98]. These examples are pertinent to PCD films which are known to be H-terminated as they are cooled in H plasma from temperatures of about 800 ^oC to room temperature subsequent to CVD growth.

The inert surface of graphene has also been functionalized for the purpose of fabricating high-κ top layers by ALD for 2D devices. The strong sp^2 C bonding of graphene has few surface ligands mainly due to defects, rendering its surface inert and hindering nucleation during ALD[34,100]. In comparison, PCD films are known to possess sp^2 C structures of graphite and as such the functionalization techniques of graphene may be worth considering for enhancing nucleation or promoting linear growth. Graphene exposed to atmospheric oxygen plasma prior to ALD of ZrO_2 resulted in an 11 nm thin film after 100 cycles, while the untreated graphene was determined to be covered in coarse grains with pores of ZrO_2[100]. The success of deposition was attributed to the O-containing groups on the graphene surface introduced by the plasma, specifically alkoxy and carboxyl groups[100]. The surface of highly oriented pyrolytic graphene (HOPG) was exposed to varying doses of O_3 in order to determine its ability to produce O surface species[101]. It was found that at relatively small doses, $<1 \times 10^8$ L, O_3 acts to removing surface contamination, while for larger doses, $>1 \times 10^{10}$ L, it has

the effect of producing O surface species[101]. It was also determined that surface contamination of graphene played an important role in achieving uniform ALD of Al_2O_3[101].

The examples given above are representative of the findings in literature where improved nucleation is achieved for ALD of the cited dielectrics on O-terminated surfaces of Si, Ge and graphene[21,99-101]. This is not to say that a predominant H-terminated surface cannot be used for achieving optimal nucleation, but rather that the film termination must be tailored to the particular ALD system of precursors and temperatures to obtain energetic favourability. In addition, manipulation of the surface should serve to preserve or enhance, rather than inhibit, the characteristics of the eventual device. Changes in diamond surface terminations are not limited to H and O species but also include F, Cl and N species because of the advantages imparted by these species for immobilization of biomolecules and proteins, stabilization of shallow nitrogen vacancy (NV^-) centres, modulation of surface electrical conductivity, electron emission in aqueous media and electrochemical applications, and in general, for facilitation of options for further surface functionalization[88,102-107]. These species provide options for further investigation into the nucleation of high-κ layers on PCD surfaces, utilizing precursors of specific chemical families, aptly matched to the surface species. Following the trend in literature however, which points to the prevalence of O surface species for superior nucleation by ALD, compared to H-termination, the former will be the focus of PCD surface treatments in the following sections.

4.2.1 PCD surface O-bond configurations

The surfaces of SCD and PCD films can be manipulated in order to change the surface terminations from predominant H to O-containing species. The motivation for this has included the use of O-terminated diamond films for sensors, due to the change in dipole moment of diamond surface, determination of the resistance of the diamond surface to oxidative erosion, adsorption of structures such as DNA or enzymes for sensing or drug delivery, and manipulation of the coefficient of friction required for use of diamond films in extreme environments and for micro/nano electro-mechanical systems (MEMS/NEMS)[108-111]. Pertinent to electronic devices, O-termination of SCD Schottky barrier diodes was shown to better facilitate the top metal, Zr, thereby increasing the barrier height[112]; O adsorption onto H-terminated diamond demonstrated tuneable band bending up to about 360 meV[94]; and metal oxide semiconductor capacitors (MOSCAPs) utilizing O-terminated SCD were shown to be completely gate controlled, demonstrating a non-detectable leakage current[113]. Investigation linking diamond surface termination to the ALD process parameters and precursors is however limited in literature but is necessary in order to bridge the understanding of fabrication procedures and device performance.

Surface chemistry is a crucial factor in determining the success of ALD to deposit continuous and conformal pin hole free thin films. Different techniques have been used to functionalize PCD and SCD, BDD and undoped (UDD) surfaces, which have resulted in variations in type and concentration of O-containing species. Table 1 summarizes some of these techniques and the associated outcomes, determined primarily by XPS. Oxidation of the PCD surface results in the formation of hydroxyl and ether bonds (C-OH/C-O-C), which are difficult to distinguish by XPS, carbonyl or ketone groups (C=O) as well as double ether configurations, and finally carboxyl groups (HO-C=O). In general, the configurations are associated with the number of bonds, one, two or three, the surface C makes with O[114].

Quantification of the different O bonds is reported in Table 1 in its original form, so that four methods are used in describing the quantification in the table. The percentages placed under the individual bonds were determined from the specific areas of their peak contributions relative to the total C1s peak area[115,116], except where '(of total O)' is noted as these percentage values are relative to the total area of surface O bonds[91]. The third method of quantification is reported in the column O/(C+O), this is the atomic percentage of O when the O1s and C1s core level signals from XPS are considered[90,115]. The final method describes the surface O coverage, as a percentage of monolayer (ML) coverage, which uses the integrated intensity ratio of the O1s peak to the C1s peak[91,114,117]. In general, UV treatments in an ozone environment and plasma treatments with H_2O and O_2 were shown to result in the highest coverage, between 80-90% for the respective parameters used. Electrochemical oxidation did however result in one of the higher concentrations of atomic O, second to a UV treatment performed on the same diamond structure[115]. It should however be noted that the O concentration for the untreated H-terminated diamond was not negligible in all cases. The lowest quantities of surface O were obtained for SCD rather than PCD, although they have not been compared under the same experimental conditions.

Table 1: Comparison of O species obtained by different oxidation techniques on diamond surfaces

Oxidation Technique	Diamond Structure	Character. Technique	O Species Quantification					
			C-OH; C-O-C	O-C-O; C-(C=O)	(C=O)-O	C-O-O-C	O/ (C+O)*	O coverage (ML)†
Electrochemical oxidation								
H_2SO_4; 0.1 mA/cm^2; 40 mins[115]	PCD BDD1.5-2 um	XPS	14%		5% (incl O-C-O)		18%	
Acid Treatment								
HNO_3 + H_2SO_4 (1:3); 200 °C; 120 mins[116]	SCD 001	XPS	8.2%					
HNO_3 + H_2SO_4 (1:1); 250 °C; 60 mins[91]	PCD	HREELS; XPS	6% (of total O)		49% (of total O)	45% (of total O)		58%
H_2SO_4 + H_2O_2 (3:1); 110 °C; 300 mins[90]	NCD UDD 6.0 um	XPS	√	√	√		4%	
UV								
UV/ozone lamp; 5 mins[115]	PCD BDD 1.5-2 um	XPS	10%		5% (incl O-C-O)		15%	
UV/ozone lamp; 10 mins[115]	PCD BDD 1.5-2 um	XPS	11%		1% (incl O-C-O)		10%	
UV/ozone lamp; 55 mins[115]	PCD BDD 1.5-2 um	XPS	29%		5% (incl O-C-O)		23%	
UV/ozone atm; 30 mins[91]	PCD UDD	HREELS; XPS	65% (of total O)		25% (of total O)	10% (of total O)		86%
UV- ozone atm; 500 mbar; 120 mins[116]	SCD (001)	XPS	7%					
UV- ozone atm; atm P; 80 °C; 20 mins[116]	SCD (001)	XPS	5%					
UV/deuterium lamp; O_2 atm; 240 mins[90]	NCD UDD 6.0 um	XPS	√	√	√		6%	
Plasma - H_2O								
H_2O plasma; 2 s[114]	BDD SCD (100)	XPS						15%
H_2O plasma; 10 s[114]	BDD SCD (100)	XPS	√	√				
H_2O plasma; 1 min[114]	BDD SCD (100)	XPS	√	√	√			51%
H_2O plasma; 5 mins[114]	BDD SCD (100)	XPS	√	√				80%
Plasma - O_2								
RF O2 plasma; 30 mins[91]	PCD UDD	HREELS;XPS	34% (of total O)		39% (of total O)	27% (of total O)		90%
O_2 plasma; 1 min[114]	BDD SCD (100)	XPS						2%
O_2 plasma; 60 mins[114]	BDD SCD (100)	XPS						35%
O_2 plasma; 120 mins[114]	BDD SCD (100)	XPS						43%
O_2 plasma;10 s[90]	NCD UDD 6.0 um	XPS	√	√	√		4%	
O_2 plasma; 40 s[115]	PCD BDD 1.5-2 um	XPS	6%		5% (incl O-C-O)		12%	

* Atomic percentage of O when considering both the O1s and C1s signals from XPS[90,115]

† O surface coverage as a percentage of monolayer (ML) coverage determined from the integrated intensity ratio of the O1s peak to the C1s peak[91,114,117]

√ denotes that the specific O bonds were present but not quantified

4.2.2 Surface O-terminations and PCD crystal orientation

Table 1 alludes to a relationship between diamond crystal orientation and affinity for oxidation as lower percentages of O surface species are shown for SCD (100) films and (001) films[114,116] compared to PCD films, which can be seen as a mixture of different crystal orientations, including grain boundaries and defects intrinsic to their polycrystalline nature. The extent of oxidation on (111) and (100) on PCD films has been reported using HREELS analysis which differentiates the CH_x vibrations on these respective planes[91]. The absence of CH_x vibrations was determined for (111) orientations while the vibration peak was dominant for (100), subsequent to UV ozone, acid treatment and O_2 plasma treatment, suggesting that the (111) facets were completely oxidized whereas the (100) facets were only partially oxidized[91]. This conclusion was reasoned with the aid of other works which explored the resistance of these orientations to hyperthermal atomic O attack. It was determined that the energy required for chemisorption of a monolayer of O on-top configuration on (100) diamond lay in the range 8–9 eV while that required for chemisorption of a monolayer of O with on-top configuration for the (111) diamond orientation was in the range 5–6.1 eV[118,119]. It is therefore pragmatic to conclude that (111) facets are easier to oxidize by hyperthermal atomic O attack than (100) facets, the latter requiring more energy for chemisorption of a monolayer.

Additionally, evidence exists for an association between the type of O species formed and the diamond crystal orientation. Simulations of the diamond (111) and (2x1) reconstructed (100) facets with H-termination demonstrated that under hyperthermal oxidation the steady state O coverage tendency is toward the formation of ketone (C-(C=O)) groups on the (100) surface, which loses its (2×1) construction, and oxy radicals on the (111) surface[108]. Exposure of the (100) surface to H_2O plasma has demonstrated a similar result but the types of bonds formed are dependent on exposure duration (Table 1)[114]. Hydroxyl groups are dominant after 10 s of exposure while ketone and double ether groups are present but in a smaller concentration, however, after 5 minutes of exposure, the hydroxyl groups are reduced while the ketone and double ether groups become dominant and sp^2 graphite also appears[114]. O surface groups have also been shown on (100) and (111) diamond films oxidized by air, without an added treatment, and in both cases ether groups were shown to be dominant, while for PCD films hydroxyl groups were dominant[92].

Other works have summarized and discussed these and similar results comparing SCD (100), (111) and (001), PCD and NCD[90,92,118,120,121]. This type of analysis is fundamental for determining which surfaces or oxidation techniques provide the optimal diamond surface species for reactions with specific ALD precursors, should they be required; increasing surface coverage is counterproductive unless it results in the species necessary for the desired reaction.

4.3 Temperature dependent high-κ fabrication

The deposition temperature of films fabricated by ALD unto diamond surfaces has been explored in literature, primarily for Al_2O_3 passivation layers. The necessity for this was determined by antecedent studies probing the desorption temperature of surface adsorbates. Table 2 collates a sample from literature which demonstrates the various ALD temperatures at which Al_2O_3 films are processed,

specifically for their passivation of diamond surface conductivity. The diamond film or device property which evidences passivation is also identified in the table.

Metal-semiconductor field effect transistors (MESFETs), with no intentional passivation layer, employing air adsorbates on SCD, displayed a drop in I_{DS} from 160 to 120 mA/mm when operated in air at temperatures from 20 to 100 °C, respectively[122]. A drop in I_{DS} was shown even when heated just to 60 °C, and decreases in gate-source *C* with temperature, in this range, were explained by the presence of a 'lossy dielectric' on H-terminated diamond[122]. In other works, the electronic properties of heated and cooled SCD films with air adsorbates were measured in vacuum, revealing that in the absence of passivation layers, sheet resistivity increased and sheet carrier concentration decreased around 300 °C[123]. Upon cooling from 500 °C, both these properties were approximately restored, concluding that H-termination is preserved without passivation up to 500 °C[123].

Similar studies achieved slightly different results, confirming desorption of adsorbates on H-terminated SCD at 300 °C in air but without restoration upon cooling; leading to the explanation that a portion of C-H bonds may have been lost at this temperature, possibly due to oxidation[61]. Under vacuum, sheet hole density of SCD films realized a minimum around 200 °C, again with failure to re-establish adsorbates[61]. Finally, the effect of temperature on hole carriers due to NO_2 exposure was also investigated and indicated that a temperature of 150 °C applied to H-terminated diamond films in vacuum was sufficient to reduce hole sheet concentration by one order of magnitude within 10 minutes[67]. Susceptibility of the diamond adsorbates to temperature, prompting changes in sheet resistivity and carrier concentration, has instigated optimization of ALD temperatures for maintaining sheet electronic properties as well as ensuring adsorbate thermal stability.

Table 2: ALD temperatures at which alumina films are deposited on diamond surfaces for the purpose of charge carrier passivation

High-κ film	Surface adsorbate	ALD temperature (°C)	Film thickness (nm)	Passivation tested by post-annealing	Property measured to demonstrate passivation[*†‡§]
Al_2O_3[61]	air	450	18	in air at 550 °C	$\rho_{sh} = 10^4$ ohm/sq
Al_2O_3[123]	air	450	40	in air at 550 °C	$\rho_{sh} = 1.8 \times 10^4$ ohm/sq; $h_{sh} = 0.8\text{-}1.5 \times 10^{13}$ /cm^2
Al_2O_3[124]	air	200	20		$I_{DS} = 339$ mA/mm
Al_2O_3[125,126]	air	250	20		$\mu = 1660 \pm 15$ cm^2/Vs
Al_2O_3[127]	air	300	25		$h_{sh} = 3.3 \times 10^{13}$ /cm^2; $I_{DS} = 205$ mA/mm
Al_2O_3[67]	NO_2	80	10	in vacuum at 150 °C	$h_{sh} = 4.5 \times 10^{13}$ /cm^2
Al_2O_3[68]	NO_2	150	17		$I_{DS} = -1350$ mA/mm
Al_2O_3[128]	NO_2	180	32		$h_{sh} = 2 \times 10^{13}$ /cm^2

[*] ρ_{sh} - sheet resistivity
[†] h_{sh} - sheet charge carrier concentration
[‡] μ - charge carrier mobility
[§] I_{DS} - drain-source channel current

Al_2O_3 films investigated for diamond surface passivation are the most prevalent in literature, although other dielectrics including AlN and HfO_2[69,129] have also been researched. ALD of Al_2O_3 films has been explored for passivation layers of both PCD and SCD films, with deposition temperatures ranging from 80 – 450 °C. Successful passivation of air adsorbates was shown for Al_2O_3 films, 20 - 25 nm in thickness, deposited at 200, and 300 °C; this was evidenced by large current outputs, I_{DS}, of 339 and 205 mA/mm, respectively[124,127]. A more comprehensive study was performed for ALD at 450 °C, which incorporated post annealing in air at 550 °C to substantiate passivation by examining adsorbate thermal stability[123,130]. A comparison of diamond sheet resistivities following Al_2O_3 deposition and then after annealing, shown in Figure 6, revealed that whilst sheet resistivity remained almost unchanged, or even improved, with Al_2O_3 deposited at 450 °C, an increase was observed for films deposited at lower temperatures, thus attesting to the reliability of the high temperature passivation layer[123,131]. Lower temperature ALD, 80 – 150 °C, was utilized for Al_2O_3 films for passivation of NO_2. Passivation was confirmed for films deposited at 80 °C, which demonstrated a stable sheet hole concentration for temperatures up to 400 °C[60]. In addition, MOSFETs employing 17 nm alumina deposited at 150 °C exhibited I_{DS} of -1350 mA/mm, one of the largest reported, at V_{GS} -5 V; even in the absence of an applied gate bias a high current of 600 mA/mm was measured[68]. Al_2O_3 layers at 80 °C also resulted in stable passivation of NO_2 on H-terminated diamond, evidenced by preservation of hole concentration and mobility at 225 °C[67]. The temperature ranges discussed here, for both air adsorbate and NO_2 passivation, are utilized in MOS devices, justified by the successes presented in literature.

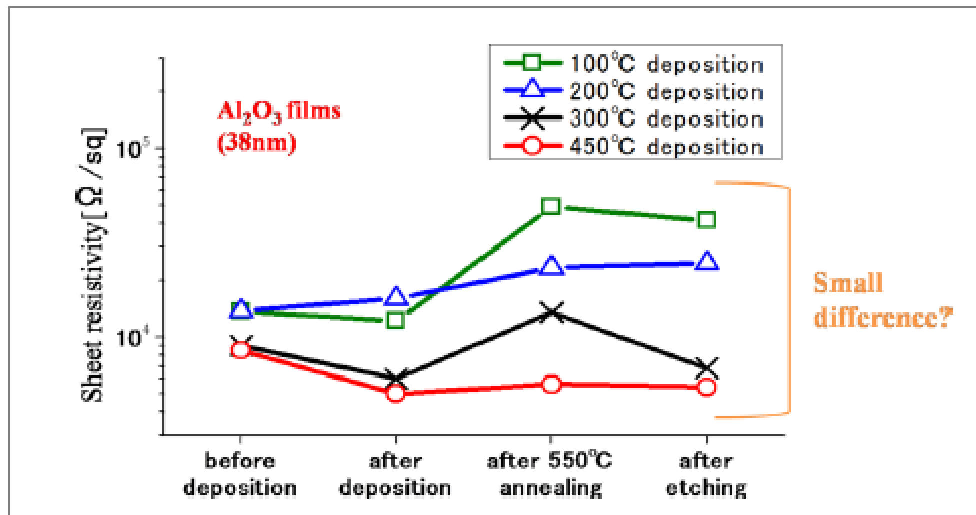

Figure 6: Plot of sheet resistivity for SCD films with 38 nm alumina passivation layers deposited by ALD at temperatures shown, 100-450 °C. Diamond sheet resistivity increased after annealing at 550 °C for all samples except for that with the surface passivation film deposited at 450 °C, suggesting, in this case, true passivation of diamond surface charge carriers [reprinted from[123], Copyright (2014), with the permission of AIP Publishing].

It would be remiss if the temperatures used for ALD of passivation layers correlated to those at which desorption of the respective adsorbates occurred. This does in fact seem to occur in some cases as with lower temperature Al_2O_3 ALD, 80-300 °C, for air adsorbates, whereby temperatures in this range

have been shown to lower I_{DS} and instigate desorption[61,122]. This is no different for NO_2 passivation where a temperature of 150 ^oC seems to both reduce hole sheet concentration by one order of magnitude[67] but also passivate the diamond surface to achieve a stable sheet hole concentration[60].

4.4 Substrate Topography

Substrates for ALD films can range from smooth planar surfaces to high aspect ratio surfaces such as those of particles and 2D materials, producing highly conformal thin films due to the self-limiting nature of the reactions whereby precursors react only with the surface sites and any unreacted precursor is efficiently removed via purging[23,132,133]. The surface roughness of PCD films therefore poses little challenge for this technique although optimization of parameters is essential to any topographical substrate. The thin films produced on the PCD surface will, however, be conformal, and therefore not result in devices with microscopically flat surfaces thus introducing limitations in electronic reliability.

Surface roughness has been associated with unreliability and inefficiency in electronic properties of transistors and capacitors when rough interfaces exist between metal and dielectric (remote surface), and dielectric and semiconductor. Scattering of charge carriers in the transistor inversion layer due to remote surface roughness has been demonstrated by a reduction in charge carrier mobility, caused by the formation of a non-uniform surface potential at rough surfaces[134,135]. It was also shown that rough metal-dielectric interfaces resulted in an additional electrostatic potential across the dielectric, compared to smooth interfaces, an increase in average electric field and decrease in breakdown field[136]. The electric field is higher at the peaks of a rough surface rather than at its valleys due to the increased density of electric charges with aspect ratio, thus a non-uniform electric field distribution at the interface is established and has the effect of scattering charge carriers[134-136]. In addition, the enhanced electric field intensity at the peaks, compared to the valleys and the bulk, can lead to localized electrical breakdown in these areas of the dielectric and proliferate to full breakdown via the opening of conduction pathways[136,137]. Simulations of the electric field distribution of Al film on Ta_2O_5 showed this field intensity at the rough interface of the films and determined that the electronic roughness, defined as the spatial distribution of the local electric field enhancements, increased with surface roughness[137,138]. Local field enhancements were discussed as being electrically active defects, sites of accelerated electrons and those deviating from their trajectory, all of which can lead to dielectric breakdown; more generally, the inhomogeneous field at the interface lowers the barrier height, encouraging electron field emission, impact ionization and bulk conductivity[137,138].

The surface roughness of high-κ films due to conformal ALD and the roughness of the PCD film surface are considerations for both remote surface scattering, which leads to a lower charge carrier mobility, as well as dielectric breakdown due to regions of local field intensities and an overall electric field inhomogeneity at the interface, which lowers the barrier height. Minimizing the roughness of the PCD surface is therefore a valuable endeavour for realizing reliable and efficient diamond devices. The use of polishing techniques for minimizing surface roughness of PCD films is predominant in recent literature as it is a cost-effective option for achieving this property at both the nano and micro levels of surface roughness[139]. Chemical-mechanical polishing using polyurethane/polyester pads and an alkaline

colloidal silica slurry achieved a reduction in surface roughness, from an initial roughness of 18.3 nm to 1.7 nm after 4 hours[140]. Addition of redox agents such as $Fe(NO_3)_3$, $KMnO_4$, $C_2H_2O_4$ and $Na_2S_2O_3$, individually to the silica slurry was shown to accelerate the polishing rate and therefore the rate of roughness reduction, with a starting roughness of 24.5 nm smoothing to 1.8 nm after 2-3 hours[141]. These results are promising for the achievement of smooth surfaces for PCD films, which will directly result in relatively smooth ALD high-κ thin films, due to conformal depositions, thus minimizing current leakage and inhomogeneity in barrier heights for diamond-based transistors. Electrical characterization of such films, used in devices, is needed in literature to determine the influence of surface roughness on performance.

5.0 Diamond-based MOS Devices

5.1 High-κ oxide films in Diamond MOS Devices

The types of films used as gate dielectrics can be constructed with binary and ternary chemistry as well as nanolaminates and the use of buffer layers. Binary metal oxide Al_2O_3 has been the front runner in SiO_2 replacement, having a higher dielectric constant and exhibiting consistency in ALD fabrication, characterization and performance; the persistent investigation of this dielectric has also rendered it ideal for non-Si based electronics[21,23,124,142,143]. ALD of higher κ HfO_2 has also gained momentum in recent years, measuring its performance against the standard, Al_2O_3[4,144-146]. Many other binary layers have been fabricated by ALD for use as gate dielectrics including, Ta_2O_5, AlN, ZrO_2 and BeO[147-151].

Ternary oxides utilize two metal precursors separated by an O precursor in the ALD process, producing films which minimize the undesirable properties of the binary film by the addition of another element in its structure. Hf for example has been incorporated into ternary oxides, $Hf_xSi_{1-x}O$, HfAlO, $HfZrO_4$ and $HfTa_xO_y$, to alleviate the effects of the less than favourable properties of its binary oxide such as low thermal stability, high proclivity for crystallization and low band offset, by combining it with compensating metal oxides[4,152-154]. This is also the purpose of ALD dielectric nanolaminates, where film characteristics are tailored by depositing alternating layers of two metal oxides, the thickness of each layer being defined by the number of ALD cycles for that binary oxide. 10 nm of HfO_2+Ta_2O_5 nanolaminate, where 1 ALD cycle of Ta_2O_5 is deposited after 2 cycles of HfO_2 until a total nanolaminate thickness of 10 nm, exhibited leakage current density and dielectric constant between those of Ta_2O_5 and HfO_2[154].

Buffer layers are typically utilized where the interface between the chosen high-κ and semiconductor surface is poor, thereby minimizing interface state density and leakage currents, and is also fabricated to facilitate high-κ deposition on inert semiconductor surfaces[155]. Insertion of an ALD AlN buffer layer between the Si substrate and ZrO_2 dielectric acted to restrict the formation of an interfacial silicate layer thereby reducing the capacitance equivalent thickness (CET), current leakage and interface state density of their MOS devices[156]. The use of an ALD Al_2O_3 buffer layer demonstrated effective suppression of the leakage current but its lower κ value reduced that of the ZrO_2-Al_2O_3 gate

stack and therefore the CET[156]. The occurrence of leakage currents by charge injection and movement across the dielectric layer is also facilitated by unsuitable VB and CB barriers at the semiconductor-dielectric interface, which are directly affected by κ via its inverse relationship with bandgap[2]. Composite oxides, nanolaminates and buffer layers provide opportunities to manipulate these properties thereby achieving a desired compromise between bandgap and κ value.

Specifically, for diamond substrates, high-κ ALD materials comprise primarily of binary metal oxides, Al_2O_3 being the most explored, although buffer layers have been shown to suppress current leakage of MOS diamond devices (Table 3). Overall, however, few high-κ materials have been investigated for diamond electronics, even fewer on PCD films. In general, it is difficult to compare the characteristics of these individual devices, although attempts will be made to, as they are influenced by a variety of factors which include processing parameters, contacting variables and component size. Table 3 provides a sample for the variety of films used either as passivation layers or gate dielectrics on diamond, in which the prevalence of Al_2O_3[81,124,131,157] is obvious as is the limited use of PCD films, the latter of which has gained momentum in more recent work[107,124]. High-κ films on diamond have included monolayers of AlN[129] (non-oxide) and HfO_2[107,158], multilayers or nanolaminates of HfO_2 and Al_2O_3[159], TiO_2-Al_2O_3 bilayers[160], and Al_2O_3 buffer layers onto which sputter deposition was performed to obtain layers of Ta_2O_5[147], $LaAlO_3$[161], $HfSiO_4$[162] and ZrO_2[163]. The increase in κ is evident when compared to Al_2O_3 which has the lowest value of the group, ranging from 5.4 for a 25 nm film to 8.0 for a 200 nm film[81,158]. The corresponding increase in C is noticed for the higher κ films, as expected from equation (1), ranging from 0.22-0.83 μFcm^{-2} for composite films with κ between 7.8-27.2[18]. As film thickness, t, will also contribute to C because of their inverse relationship (equation (1)), this could be one of the possible reasons for the lower C, 0.11 μFcm^{-2}, for $HfSiO_4$ on Al_2O_3 as a larger C, 0.25 μFcm^{-2}, was achieved in the same investigation for 20 nm of only Al_2O_3 on diamond (not shown)[162]. Another interesting observation is the smaller C of MCD and UNCD, in the range of pF, compared to SCD films in the μF range. The few examples of PCD-based MOS devices will not provide clarity on their capabilities neither can it be achieved solely from device characterization without investigation into interface processing.

Table 3: MOS devices utilizing high-κ films on diamond films

Film	Fabrication technique /temp[√] (°C)	Type of layer[**]	Size, t, l, w[††] (μm)	κ value		Film Character.	Film Thick. (μm)	VB (eV)	CB (eV)	Cap, C / freq, f[‡‡] (μFcm^{-2}) /(kHz)	Leak curr den, J / $V_{(GS)}$[§§] (Acm^{-2})/ (V)	$I_{(DS) MAX}$ /$V_{(GS)}$[***] ($mAmm^{-1}$) /(V)	$V_{(TH)}$[†††] (V)
Al_2O_3[157]	ALD/250	ML	0.02 (t)		MOSCAP	O-SCD B doped	0.59	1.34	0.56	0.13 / 1000	7e^-3 / -5		
Al_2O_3[124]	ALD/200	PL, GO	0.02, 2, 50		MOS diode/ MOSFET	H-PCD	250			0.28 / 1000	e^-6 / -6	-339 / -10	7.4
Al_2O_3[124]	ALD/300	PL, GO	0.02, 2, 50		MOS diode/ MOSFET	H-PCD	250			0.33 / 1000	e^-6 / -6	-85 / -10	4.4
Al_2O_3[131]	ALD/450	PL, GO	(0.01-0.2), 2, 25		MOSFET	H-SCD (001) B doped	0.50					-30 -(-45)/ -4	
Al_2O_3[81]	ALD/250	ML	0.20 (t)	8.0	MOSCAP	O-SCD (100) B doped					e^-1 / -10		
Al_2O_3[18,158,159]	ALD/120	ML	0.025, 4, 150	5.4	MISFET	H-SCD	0.15	2.9	1.2	0.19 / 50	1.1e^-7 / -4		
AlN[129]	ALD/370	PL	0.01, 0.2, 25	7.5	MESFET	H-SCD (100)	0.20					-112 / -2	0.8
HfO_2[18,158]	ALD/120	ML	0.025, 4, 150	12.1	MIS diode/ MISFET	H-SCD	0.15	2.6	2.7	0.39	9.3e^-4		
HfO_2[107]	ALD	PL	0.03 (t)		MISCAP	H-UNCD on Si				0.75e-5 / 1			
HfO_2[107]	ALD	PL	0.03 (t)		MISCAP	F-UNCD on Si				0.40e^-5 / 1			
HfO_2[107]	ALD	PL	0.03 (t)		MISCAP	H-MCD on Si				2.60e^-5 / 1			
HfO_2[107]	ALD	PL	0.03 (t)		MISCAP	F-MCD on Si				1.90e^-5 / 1			
HfO_2-Al_2O_3[159]	ALD/120	MultiL (NLam)	0.032, 4, 150	7.8	MIS diode/ MISFET	H-SCD				0.22 / 50	3.8e^-8	-42 / -8	1.8
$HfSiO_4$-Al_2O_3[162]	SD-ALD/80,250	BiL	(0.052 on 0.020), 15, 100	9.0	MOSFET	H-SCD (001)	0.20			0.11 / 100	e^-7	-25 / -8	2.3
$LaAlO_3$-Al_2O_3[161]	SD-ALD/120	Al_2O_3 BL	(0.027 on 0.004), 10, 150	9.1	MOS diode/ MOSFET	H-SCD (100)		2.9 (1.1 with $LaAlO_3$)	1.2 (1.6 with $LaAlO_3$)	0.26 / 10	e^-8 / -4	-7.5 / -8	-3.6
Ta_2O_5-Al_2O_3[147]	SD-ALD/120	BiL	(0.025 on 0.004), 4, 150	12.7	MIS diode/ MISFET	H-SCD (100)	0.20			0.40 / 50	e^-11	-97.7 / -4	1.3
TiO_2-Al_2O_3[160]	ALD/120	BiL	(0.025 on 0.004), 4, 150	27.2	MOSCAP/ MOSFET	H-SCD	0.15	2.3	4.4	0.83 / 50	2.1e^-5 / -4	-11.6 / -4.5	0.8
ZrO_2-Al_2O_3[163]	SD-ALD/120	Al_2O_3 BL	(0.023 on 0.004), 4, 150	15.4	MISFET	H-SCD (100)		2.9 (0.6 with ZrO_2)	1.2 (1.0 with ZrO_2)	0.31	4.8e^-5 / -4	-72.7 / -7	1.6

[√] Temperatures given are only for ALD; SD-sputter deposition

[**] Designations are as given in the respective articles; ML-monolayer, PL-passivation layer, GO-gate oxide, MultiL- multilayer, NLam-nanolaminate, BiL-bilayer, BL-buffer layer

[††] Size dimensions of high-κ layer; t-thickness, l-length, w-width

[‡‡] Capacitance measurement of device and frequency at which it was measured

[§§] Leakage current density and the applied gate-source voltage, V(GS), at which it was obtained

[***] Maximum drain-source and the applied gate-source voltage, V(GS), at which it was obtained

[†††] Threshold voltage of the device

5.2 Energy Band Alignment and Electronic Manipulation

The properties of dielectric films, which make them viable candidates for use as gate oxides or passivation layers for specific semiconductors, have been addressed in literature[2,164]. Among others, these properties include κ value, film morphology, interface quality, thermodynamic stability, presence of defects and energy band alignment[2,164]. Energy band alignment is of particular importance as it is specific to the combination of high-κ film and semiconductor material, and considers not only their unique bandgaps but also the alignment of the VB and CB, which is directly related to the occurrence of leakage currents due to Schottky emissions[5]. A requirement of the band alignment between the dielectric and the semiconductor is therefore a minimum band offset or barrier of 1 eV at the VB and CB to hinder conduction via emission of holes or electrons, respectively into the oxide[2,5].

Measurement of VB and CB band offsets is typically achieved with photoemission spectroscopy techniques[165,166]. The use of XPS has been instrumental in band alignment determination since its applicability to achieve accurate determination of heterojunction band discontinuities was reported, by using the difference in binding energy (BE) of a reference core level (CL) and that of the VB edge at the interface and in the bulk; precision in locating the VBM from the spectra was noted to significantly influence the accuracy of the method[165]. This technique has since been applied to high-κ films on semiconductor films and substrates, using equation (3) to calculate the VBM[165].

$$\Delta E_{VBM} = (E_{CL} - E_{VBM})_S - (E_{CL} - E_{VBM})_\kappa - \Delta E_{CL} \qquad (3)$$

ΔE_{VBM} is the VB offset at the interface; $(E_{CL} - E_{VBM})_S$ is the difference in BE of the CL and VBM for the bulk semiconductor; $(E_{CL} - E_{VBM})_\kappa$ is the difference in BE of the CL and VBM for the bulk high-κ material; and ΔE_{CL} is the difference in BE of the high-κ CL and the semiconductor CL, measured at the interface, i.e. for a thin, ≤4 nm[157,158], high-κ film on the semiconductor. The VBM for each spectrum is obtained by extrapolating a linear fit for the leading edge of the VB photoelectron spectra to the baseline and analysis is performed subsequent to initial calibration of the CL BE for all samples to obtain a reference position[157,158]. The CBM for both the high-κ film and the semiconductor can subsequently be determined once the respective energy bandgaps are known, the difference in CBMs will be the CB offset, ΔE_{CBM}[158].

Band offsets for high-κ films on diamond are listed in Table 3 and have been calculated from equation (3) using data from XPS measurements. In all cases the dielectrics used, HfO_2, $LaAlO_3$-Al_2O_3 and Al_2O_3 realized a VB offset higher than 1 eV on SCD films, while the CB offset was calculated to be less than 1 eV only for Al_2O_3 on O-treated SCD[157,158,161,163], although it should be noted that this value is dependent on the value of the energy bandgap used. Realization of such a low band offset signifies the presence of a low barrier, which for an n-type diamond film in a normally off MOSFET, permits injection of electrons into the Al_2O_3 thereby trapping charges in the oxide or resulting in a leakage current due to movement of electrons through the oxide and into the metal[157,167]. The incorporation of a buffer layer with suitable band offsets, as in the case of Al_2O_3, can therefore benefit the band alignment with diamond while the higher κ top layer with possibly a lower barrier, such as ZrO_2, retains its function to increase the composite κ value and therefore device performance; the *C* with the ZrO_2 on Al_2O_3 buffer

layer was 0.31 μFcm^{-2} compared to 0.19 μFcm^{-2} for an Al_2O_3 monolayer with the same dimensions[18,168]. A VB offset higher than 1 eV signifies hole confinement and a larger barrier to their tunnelling, in which case p-type diamond films can be utilized for normally off MOSFETs, all other influences on charge carrier energy, such as temperature, being equal. As there are many high-κ materials that can be tested for PCD-based devices, one criterion prior to device fabrication should be the measurement of the band offsets, as this can give justification for further experimentation and anticipated device performance.

Band alignment can be manipulated through high-κ stoichiometry as well as diamond surface species, which relate to interface bonding and states. Computational methods were used to determine the band offsets of TiO_2 on diamond films, having either an O atom interface or a H atom interface, the result was an increase in the VB offset from 0.6 to 1.7 eV with the addition of H[169]. It was also noted that the VB offset for TiO_2 on H-diamond was determined by XPS to be 2.6 eV, the discrepancy possibly due to interface defects[169]. Al_2O_3 on O-terminated diamond was also expected to realize a lower VB offset due to the change in electron affinity imposed by O termination[157]. H-terminated diamond surfaces have NEA as the vacuum level lies below the CBM, whereas oxidation of this surface will result in the vacuum level being located above the CBM and hence a positive electron affinity (PEA)[170]. This difference is due to the dipole formation at the surface; O, having a higher electronegativity than C, will form a surface dipole, with its atoms being the negative pole and those of C being the positive pole, resulting in PEA[94,170]. H however has a lower electronegativity than C creating a surface dipole with H atoms as the positive pole and therefore NEA, a property desirable for conductivity through the CB as it more readily facilitates e^- emission from the diamond surface compared to PEA [94,170]. UV photoemission spectroscopy (UPS) spectra analysis determined that for both B doped and undoped PCD O termination resulted in PEA while H termination resulted in NEA[170]. In addition, the VBM was also manipulated by surface termination, increasing from the as-grown value for both doped and undoped films, but only for the doped films was an increase from -0.6 to -1.4 eV measured for H- and O-terminated surfaces, respectively[170]. It was suggested that the VBM values could be skewed due to localized defect states[170] but such differences due to surface species will have an impact when bonded with a high-κ layer. N, F and Cl diamond surface terminations are also shown to result in PEA surfaces, the value of which can be modulated by the percentage coverage[105,106,171].

A discussion of diamond surface species manipulation can be seen in Section 4.2 Manipulation of Surface Termination Species. In general, changing of the surface ligands can better facilitate chemical reactions with ALD precursors on diamond as well as contribute to its 2DHG surface conduction through the adsorption of molecules as with NO_2[60,124,128,130]. In addition, a compromise with band alignment should now be accommodated as diamond surface O termination has been shown to result in lower VB offsets, as in the case of TiO_2[169], possibly due to the induced PEA or to the introduction of interface states, which are suppressed by H termination resulting in a higher VB offset[94,169]. The benefit derived from the use of ALD for the deposition of high-κ layers on PCD films is the control of initial cycles at atomic levels to minimize or perhaps even prevent the introduction of interface states that will otherwise result in inefficient devices operation and overall poor performance. Literature has shown however that nucleation of some metal oxides by ALD is more uniform with surface O ligands[21,99-101]. The interfacial reaction between the PCD surface species and ALD precursors is therefore a key factor in maximizing charge carrier conductivity in MOSFET devices.

5.3 Diamond MOS Device Performance

Comparison of some performance characteristics are included in Table 3 to demonstrate the types of values achieved for the specific combinations of dielectric and diamond film. Comparison between dielectrics based solely on performance is cautioned against as these values are also dependent on other factors such as diamond film properties and device dimensions. Diamond film conductivity is an important consideration as conductivity due to dopants, such as B, is dependent on concentration, and can be through its bulk or at its surface via a 2DHG, the latter also being the case for undoped diamond with certain surface terminations[60,124]. Device performance is also dependent on passivation layers, which maintain the surface charge as they can extend between the transistor D and S, rather than existing only below the gate contact as with gate dielectric layers[61]. In addition, performance is dimension dependent, evident from the inverse relationship between high-κ t and *C* (equation (1)), and even as it pertains to lateral gate size and distance from the S and D contacts[131,161]. Performance is also dependent on the conditions in which measurements are performed such as temperature, voltage and frequency ranges. It is therefore suggested that the reader obtain any of these details in the specific references of Table 3.

Measurements of device performance include *C*, leakage current density (J) measured through the G at a specific applied voltage (V), maximum current (I_{DSMAX}) flowing between D and S, also measured at a specific V, and threshold voltage, V_{TH}, applied between G and S, which is the V needed to turn an 'off' device 'on', or vice versa. Overall, the *C* values shown in Table 3 have a direct dependence on κ for total film thickness, t in the range 27-36 nm[18,160,161,163]. The largest κ oxide, TiO_2 on Al_2O_3, with value 27.2 contributes the highest *C* of 0.83 μFcm^{-2}[160]. J values are in the range 10^{-8}-10^{-1} Acm^{-2}, with PCD films achieving current densities as small as 10^{-6} Acm^{-2} for Al_2O_3[124]. Higher κ layers do not necessarily result in a lower J but in the case of the HfO_2 monolayer and HfO_2-Al_2O_3 nanolaminate layer, J decreases with the incorporation of Al_2O_3[159]. I_{DSMAX} ranges from -7.5 to -112 $mAmm^{-1}$ for SCD films[129,161] while larger values, -85 to -339 $mAmm^{-1}$ are obtained for PCD substrates[124], indicating the applicability of the latter for electronics, although determination of conduction pathways will enlighten as to the influence of grain boundaries and non-diamond content. Values for V_{TH} for SCD are between -3.6 and 1.8 V[159,161], and 4.4 to 7.4 V for PCD substrates[124].

I_{DSMAX} and V_{TH} measurements are highly dependent on the conductive quality of the diamond film but are also influenced by the high-κ film interface quality, which facilitates charge trapping or leakage. In the case of the SCD examples given here, conductivity is defined by the 2DHG of surface adsorbates or terminations, and the low I_{DSMAX} of -7.5 $mAmm^{-1}$ was therefore explained as being due to a low hole density for H-terminated SCD, compared to those exposed to NO_2 which achieved a higher I_{DSMAX}[68,161]. The PCD samples of Table 3 are also H-terminated, conducting through a 2DHG, and the Al_2O_3 layer was fabricated by ALD at two temperatures, 200 and 300 ^oC[124]. The larger I_{DSMAX} of -339 $mAmm^{-1}$ was discussed as possibly being due to retention of the surface adsorbates responsible for the 2DHG conductivity, at a lower ALD fabrication temperature, and their possible degradation at higher temperatures[124]. Degradation of hole mobility has been recorded for exposure temperatures greater than approximately 126 ^oC on H-terminated diamond[67], providing further evidence for precaution in the choice of ALD parameters.

The UNCD and MCD metal insulator semiconductor capacitors (MISCAPs) are novel amongst the counterparts of Table 3. The investigation of these devices compares the influence of grain size and sp^3 content, and surface terminations. The UNCD MISCAPs recognize a smaller C compared to the MCD MISCAPs by one order of magnitude, explained by the occurrence of leakage current or movement of charge carriers through the larger grain boundary area of the UNCD films thereby resulting in a smaller C[107]. The behaviour of the devices subsequent to F-termination also varied for UNCD and MCD films as F-terminated UNCD exhibited p-type conductivity while that of MCD was n-type, evidenced by an increase in C in the positive V range[107].

In general the V_{TH} is mainly determined by the properties of the charge carrier, such as its density beneath the oxide film[124,161]. The corresponding higher V_{TH}, 7.4 V, for the PCD sample with Al_2O_3 fabricated at 200 °C (Table 3) was explained by the presence of a higher hole density beneath the gate due to retention of surface charges at this lower ALD temperature when compared with a V_{TH} of 4.4 V for Al_2O_3 fabrication at 300 °C[124]. Charge carrier properties at the diamond surface, below the oxide film, are therefore influenced by the high-κ film. Unoccupied energy levels exist in the bandgap of the Al_2O_3 film below the VBM of diamond, enabling the attraction of holes across the interface and therefore the formation of a new 2DHG[124]. Simulated surface charge density values for SCD passivated by Al_2O_3 and HfO_2 films demonstrated a negative charge for the Al_2O_3 film and a positive charge for the HfO_2 film, thereby resulting in different surface passivation properties, and influences on diamond hole transport[125]. Furthermore, the higher SCD hole mobility was found for the Al_2O_3 passivation, attributed to a reduction in interface scattering and charge trapping[125]. The negative V_{TH}, -3.6V, found for $LaAlO_3$-Al_2O_3 describes an enhancement mode operation for the associated MOSFET, that is, one for which there is no current output at V_{GS}=0[18,161]. This mode was reported as resulting from either the disappearance of the adsorbed, negatively charged layer on the diamond surface, or from the formation of positive charges at the high-κ-diamond interface[18].

The examples discussed here of the electrical performance of MOS devices demonstrate the value of high-κ materials for diamond-based devices and the potential that can possibly be achieved for PCD films. Device performance is shown to be sensitive to the high-κ-diamond interface characteristics making the composition of this interface, the diamond surface species and initial reactions of the high-κ layer, crucial factors for control. ALD provides for this atomic layer sensitivity although more thorough characterization and analysis is required to achieve a clearer understanding at these initial reactions. In addition, the heterogeneity of the PCD surface further complicates interface bonding. Investigation of high-κ prospects for PCD films is however necessary to determine their electronic performance and therefore their contribution to cost-effective diamond-based devices.

1 A. I. Kingon, J. P. P. Maria and S. K. Streiffer, *Nature*, 2000, **406**, 1032–1038.

2 J. Robertson and R. M. Wallace, *Mater. Sci. Eng. R Reports*, 2015, **88**, 1–41.

3 N. Biyikli and A. Haider, *Semicond. Sci. Technol.*, 2017, **32**, 093002.

4 Y. Senzaki, K. Choi and P. Kirsch, *AIP Conf. Proc.*, 2005, **788**, 69–72.

5 J. Robertson, *J. Vac. Sci. Technol. B Microelectron. Nanom. Struct.*, 2000, **18**, 1785.

6 R. L. Puurunen, *Chem. Vap. Depos.*, 2014, **20**, 332–344.

7 M. Leskelä and M. Ritala, *Angew. Chemie - Int. Ed.*, 2003, **42**, 5548–5554.

8 S. Fujita, *Jpn. J. Appl. Phys.*, 2015, **54**, 030101.

9 J. Y. Tsao, S. Chowdhury, M. A. Hollis, D. Jena, N. M. Johnson, K. A. Jones, R. J. Kaplar, S. Rajan, C. G. Van de Walle, E. Bellotti, C. L. Chua, R. Collazo, M. E. Coltrin, J. A. Cooper, K. R. Evans, S. Graham, T. A. Grotjohn, E. R. Heller, M. Higashiwaki, M. S. Islam, P. W. Juodawlkis, M. A. Khan, A. D. Koehler, J. H. Leach, U. K. Mishra, R. J. Nemanich, R. C. N. Pilawa-Podgurski, J. B. Shealy, Z. Sitar, M. J. Tadjer, A. F. Witulski, M. Wraback and J. A. Simmons, *Adv. Electron. Mater.*, 2018, **4**, 1–49.

10 J. Millan, P. Godignon, X. Perpina, A. Perez-Tomas and J. Rebollo, *IEEE Trans. Power Electron.*, 2014, **29**, 2155–2163.

11 N. Kaminski, in *13th European Conference on Power Electronics and Applications, 2009.*, 2009, 1–9.

12 J. A. Del Alamo, *Nature*, 2011, **479**, 317–323.

13 T. S. Tripathi and M. Karppinen, *Adv. Mater. Interfaces*, 2017, **4**, 1–16.

14 C. J. H. Wort and R. S. Balmer, *Mater. Today*, 2008, **11**, 22–28.

15 J. J. Gracio, Q. H. Fan and J. C. Madaleno, *J. Phys. D. Appl. Phys.*, 2010, **43**, 374017.

16 S. Shikata, *Diam. Relat. Mater.*, 2016, **65**, 168–175.

17 X. Lu Yuan, Y. Ting Zheng, X. Hua Zhu, J. Long Liu, J. Wei Liu, C. Ming Li, P. Jin and Z. Guo Wang, *Int. J. Miner. Metall. Mater.*, 2019, **26**, 1195–1205.

18 J. Liu and Y. Koide, *Sensors*, 2018, **18**, 813.

19 R. W. Johnson, A. Hultqvist and S. F. Bent, *Mater. Today*, 2014, **17**, 236–246.

20 H. Kim, *J. Vac. Sci. Technol. B Microelectron. Nanom. Struct.*, 2003, **21**, 2231.

21 R. L. Puurunen, *J. Appl. Phys.*, 2005, **97**, 121301-121301–52.

22 H. H. Sønsteby, A. Yanguas-Gil and J. W. Elam, *J. Vac. Sci. Technol. A*, 2020, **38**, 020804.

23 S. M. George, *Chem. Rev.*, 2010, **110**, 111–131.

24 Y. Xie, L. Ma, D. Pan and C. Yuan, *Chem. Eng. J.*, 2015, **259**, 213–220.

25 S. D. Elliott and J. C. Greer, *J. Mater. Chem.*, 2004, **14**, 3246–3250.

26 L. Jin, Y. Li, Z. Hu and J. Chu, *AIP Adv.*, 2018, **8**, 045304.

27 T. J. Larrabee, T. E. Mallouk and D. L. Allara, *Rev. Sci. Instrum.*, 2013, **84**, 014102.

28 J. Sundqvist, H. Högberg and A. Hårsta, *Chem. Vap. Depos.*, 2003, **9**, 245–248.

29 T. Henke, M. Knaut, M. Geidel, F. Winkler, M. Albert and J. W. Bartha, *Thin Solid Films*, 2017, **627**, 94–105.

30 C. Ozgit, I. Donmez, M. Alevli and N. Biyikli, *Thin Solid Films*, 2012, **520**, 2750–2755.

31 R. L. Puurunen, W. Vandervorst, W. F. A. Besling, O. Richard, H. Bender, T. Conard, C. Zhao, A. Delabie, M. Caymax, S. De Gendt, M. Heyns, M. M. Viitanen, M. De Ridder, H. H. Brongersma, Y. Tamminga, T. Dao, T. De Win, M. Verheijen, M. Kaiser and M. Tuominen, *J. Appl. Phys.*, 2004, **96**, 4878–4889.

32 K. Kukli, J. Aarik, A. Aidla, H. Siimon, M. Ritala and M. Leskelä, *Appl. Surf. Sci.*, 1997, **112**, 236–242.

33 D. M. Hausmann, E. Kim, J. Becker and R. G. Gordon, *Chem. Mater.*, 2002, **14**, 4350–4358.

34 S. J. McDonnell and R. M. Wallace, *Jom*, 2018, **71**, 224–237.

35 V. Pore, A. Rahtu, M. Leskelä, M. Ritala, T. Sajavaara and J. Keinonen, *Chem. Vap. Depos.*, 2004, **10**, 143–148.

36 M. Putkonen, P. Sippola, L. Svärd, T. Sajavaara, J. Vartiainen, I. Buchanan, U. Forsström, P. Simell and T. Tammelin, *Philos. Trans. R. Soc. A Math. Phys. Eng. Sci.*, 2018, **376**, 20170037.

37 M. H. Ko, B. Shong and J. H. Hwang, *Ceram. Int.*, 2018, **44**, 16342–16351.

38 Y. Kim, M. S. Kim, H. J. Yun, S. Y. Ryu and B. J. Choi, *Ceram. Int.*, 2018, **44**, 17447–17452.

39 D. Riihelä, M. Ritala, R. Matero, M. Leskelä, J. Jokinen and P. Haussalo, *Chem. Vap. Depos.*, 1996, **2**, 277–283.

40 Q. Xie, Y. L. Jiang, C. Detavernier, D. Deduytsche, R. L. Van Meirhaeghe, G. P. Ru, B. Z. Li and X. P. Qu, *J. Appl. Phys.*, 2007, **102**, 083521.

41 B. Abendroth, T. Moebus, S. Rentrop, R. Strohmeyer, M. Vinnichenko, T. Weling, H. Stöcker and D. C. Meyer, *Thin Solid Films*, 2013, **545**, 176–182.

42 M. E. Dufond, M. W. Diouf, C. Badie, C. Laffon, P. Parent, D. Ferry, D. Grosso, J. C. S. Kools, S. D. Elliott and L. Santinacci, *Chem. Mater.*, 2020, **32**, 1393–1407.

43 M. Kim, W. Kim, T. Lee and H. Kim, *Thin Solid Films*, 2013, **542**, 71–75.

44 M. C. Karunarathne, J. W. Baumann, M. J. Heeg, P. D. Martin and C. H. Winter, *J. Organomet. Chem.*, 2017, **847**, 204–212.

45 S. J. Song, T. Park, K. J. Yoon, J. H. Yoon, D. E. Kwon, W. Noh, C. Lansalot-matras, S. Gatineau, H. Lee, S. Gautam, D. Cho, S. W. Lee and C. S. Hwang, *Appl. Mater. Interfaces*, 2016, **9**, 537–547.

46 N. Yang, S. Yu, J. V Macpherson and Y. Einaga, *Chem. Soc. Rev.*, 2019, **48**, 157–204.

47 J. V Macpherson, *Phys. Chem. Chem. Phys.*, 2015, **17**, 2935–49.

48 D. C. Barbosa, P. R. P. Barreto, V. W. Ribas, V. J. Trava-Airoldi and E. J. Corat, in *Encyclopedia of Nanoscience and Nanotechnology*, ed. H. S. Nalwa, American Scientific Publishers, 2011.

49 E. M. A. Fuentes-Fernandez, J. J. Alcantar-Peña, G. Lee, A. Boulom, H. Phan, B. Smith, T. Nguyen, S. Sahoo, F. Ruiz-Zepeda, M. J. Arellano-Jimenez, P. Gurman, C. A. Martinez-Perez, M. J. Yacaman, R. S. Katiyar and O. Auciello, *Thin Solid Films*, 2016, **603**, 62–68.

50 V. V. S. S. Srikanth, P. Sampath Kumar and V. B. Kumar, *Int. J. Electrochem.*, 2012, **2012**, 1–7.

51 S. Ohmagari, H. Yamada, H. Umezawa, N. Tsubouchi, A. Chayahara and Y. Mokuno, *Diam. Relat. Mater.*, 2018, **81**, 33–37.

52 J. G. Buijnsters, M. Tsigkourakos, T. Hantschel, F. O. V. Gomes, T. Nuytten, P. Favia, H. Bender, K. Arstila, J.-P. Celis and W. Vandervorst, *ACS Appl. Mater. Interfaces*, 2016, **8**, 26381–26391.

53 M. A. Neto, G. Pato, N. Bundaleski, O. M. N. D. Teodoro, A. J. S. Fernandes, F. J. Oliveira and R. F. Silva, *Diam. Relat. Mater.*, 2016, **64**, 89–96.

54 S. Ohmagari, M. Ogura, H. Umezawa and Y. Mokuno, *J. Cryst. Growth*, 2017, **479**, 52–58.

55 A. C. Ferrari and J. Robertson, *Philos. Trans. A. Math. Phys. Eng. Sci.*, 2004, **362**, 2477–2512.

56 P. W. May, W. J. Ludlow, M. Hannaway, P. J. Heard, J. A. Smith and K. N. Rosser, *Diam. Relat. Mater.*, 2008, **17**, 105–117.

57 J. H. T. Luong, B. Male, J. D. Glennon, K. B. Male and J. D. Glennon, *Analyst*, 2009, **134**, 1965–79.

58 O. A. Williams, *Diam. Relat. Mater.*, 2011, **20**, 621–640.

59 Y. A. Mankelevich, M. N. R. Ashfold, D. W. Comerford, J. Ma and J. C. Richley, *Thin Solid Films*, 2011, **519**, 4421–4425.

60 M. Kasu, *Jpn. J. Appl. Phys.*, 2017, **56**, 01AA01.

61 A. Hiraiwa, A. Daicho, S. Kurihara, Y. Yokoyama and H. Kawarada, *J. Appl. Phys.*, 2012, **112**, 124504-1–6.

62 P. Strobel, M. Riedel, J. Ristein and L. Ley, *Nature*, 2004, **430**, 439–441.

63 M. W. Geis, T. C. Wade, C. H. Wuorio, T. H. Fedynyshyn, B. Duncan, M. E. Plaut, J. O. Varghese, S. M. Warnock, S. A. Vitale and M. A. Hollis, *Phys. Status Solidi Appl. Mater. Sci.*, 2018, **215**, 1–14.

64 C. Verona, W. Ciccognani, S. Colangeli, E. Limiti, M. Marinelli and G. Verona-Rinati, *J. Appl. Phys.*, 2016, **120**, 025104.

65 P. Rivero, W. Shelton and V. Meunier, *Carbon N. Y.*, 2016, **110**, 469–479.

66 O. A. Williams and R. B. Jackman, *Semicond. Sci. Technol.*, 2003, **18**, S34–S40.

67 M. Kasu, H. Sato and K. Hirama, *Appl. Phys. Express*, 2012, **5**, 025701.

68 K. Hirama, H. Sato, Y. Harada, H. Yamamoto and M. Kasu, *Jpn. J. Appl. Phys.*, 2012, **51**, 090112.

69 Z. Ren, D. Lv, J. Xu, K. Su, J. Zhang, D. Wang, Y. Wu, J. Zhang and Y. Hao, *Diam. Relat. Mater.*, 2020, **106**, 107846.

70 S. A. O. Russell, L. Cao, D. Qi, A. Tallaire, K. G. Crawford, A. T. S. Wee and D. A. J. Moran, *Appl. Phys. Lett.*, 2013, **103**, 202112.

71 K. Xing, Y. Xiang, M. Jiang, D. L. Creedon, G. Akhgar, S. A. Yianni, H. Xiao, L. Ley, A. Stacey, J. C. McCallum, S. Zhuiykov, C. I. Pakes and D. C. Qi, *Appl. Surf. Sci.*, 2020, **509**, 144890.

72 J. R. Oliveira, O. M. Berengue, J. Moro, N. G. Ferreira, A. J. Chiquito and M. R. Baldan, *Appl. Surf. Sci.*, 2014, **311**, 5–8.

73 P. Ashcheulov, J. Šebera, A. Kovalenko, V. Petrák, F. Fendrych, M. Nesládek, A. Taylor, Z. Vlčková Živcová, O. Frank, L. Kavan, M. Dračínský, P. Hubík, J. Vacík, I. Kraus and I. Kratochvílová, *Eur. Phys. J. B*, 2013, **86**, 443.

74 T. Saito, K. H. Park, K. Hirama, H. Umezawa, M. Satoh, H. Kawarada and H. Okushi, *Diam. Relat. Mater.*, 2005, **14**, 2043–2046.

75 L. Kavan, Z. Vlckova Zivcova, V. Petrak, O. Frank, P. Janda, H. Tarabkova, M. Nesladek and V. Mortet, *Electrochim. Acta*, 2015, **179**, 626–636.

76 V. Mortet, Z. V. Živcová, A. Taylor, M. Davydová, O. Frank, P. Hubík, J. Lorincik and M. Aleshin, *Diam. Relat. Mater.*, 2019, **93**, 54–58.

77 E. Gheeraert, P. Gonon and A. Deneuville, *Diam. Relat. Mater.*, 1993, **2**, 742–745.

78 V. Mortet, L. Kavan, A. Taylor, Z. Vl, D. Machon, O. Frank, P. Hubík and D. Tremouilles, *Diam. Relat. Mater.*, 2018, **88**, 163–166.

79 P. Wurzinger, P. Pongratz, P. Hartmann, R. Haubner and B. Lux, *Diam. Relat. Mater.*, 1997, **6**, 763–768.

80 G. Janssen, W. J. P. van Enckevort, W. Vollenberg and L. J. Giling, *Diam. Relat. Mater.*, 1992, **1**, 789–800.

81 K. K. Kovi, Ö. Vallin, S. Majdi and J. Isberg, *IEEE Electron Device Lett.*, 2015, **36**, 603–605.

82 A. C. Ferrari and J. Robertson, *Phys. Rev. B*, 2000, **61**, 95–107.

83 J. J. Wang, Z. Z. He, C. Yu, X. B. Song, H. X. Wang, F. Lin and Z. H. Feng, *Diam. Relat. Mater.*, 2016, **70**, 114–117.

84 Z. Ren, J. Zhang, J. Zhang, C. Zhang, D. Chen, P. Yang, Y. Li and Y. Hao, *IEEE Electron Device Lett.*, 2017, **38**, 1302–1304.

85 Y. Fu, R. Xu, Y. Xu, J. Zhou, Q. Wu, Y. Kong, Y. Zhang, T. Chen and B. Yan, *IEEE Electron Device Lett.*, 2018, **39**, 1704–1707.

86 S. Michaelson, O. Ternyak, A. Hoffman and Y. Lifshitz, *Appl. Phys. Lett.*, 2007, **90**, 031914.

87 K. Hirama, H. Takayanagi, S. Yamauchi, J. H. Yang, H. Kawarada and H. Umezawa, *Appl. Phys. Lett.*, 2008, **92**, 112107.

88 S. Szunerits and R. Boukherroub, *J. Solid State Electrochem.*, 2008, **12**, 1205–1218.

89 J. H. Park, H. C. P. Movva, E. Chagarov, K. Sardashti, H. Chou, I. Kwak, K. T. Hu, S. K. Fullerton-Shirey, P. Choudhury, S. K. Banerjee and A. C. Kummel, *Nano Lett.*, 2015, **15**, 6626–6633.

90 S. Torrengo, R. Canteri, R. Dell'Anna, L. Minati, A. Pasquarelli and G. Speranza, *Appl. Surf. Sci.*, 2013, **276**, 101–111.

91 F. N. Li, R. Akhvlediani, M. K. Kuntumalla, A. Hoffman and A. Ho, *Appl. Surf. Sci.*, 2019, **465**, 313–319.

92 S. Ghodbane, D. Ballutaud, F. Omnès and C. Agnès, *Diam. Relat. Mater.*, 2010, **19**, 630–636.

93 K. Wei, J. Li, B. Liu, R. Wu, Q. Wei, S. Wu, W. Hu and H. Wang, *Vacuum*, 2020, **172**, 109046.

94 G. Wan, M. Cattelan and N. A. Fox, *J. Phys. Chem. C*, 2019, **123**, 4168–4177.

95 Z. Shpilman, I. Gouzman, E. Grossman, R. Akhvlediani and A. Hoffman, *Appl. Phys. Lett.*, 2008, **92**, 234103.

96 D. Thian, Y. T. Yemane, S. Xu and F. B. Prinz, *J. Phys. Chem. C*, 2017, **121**, 27379–27388.

97 J. F. Mack, P. B. Van Stockum, Y. T. Yemane, M. Logar, H. Iwadate, F. B. Prinz, P. B. Van Stockum, Y. T. Yemane, M. Logar, H. Iwadate and F. B. Prinz, *Chem. Mater.*, 2012, **24**, 4357–4362.

98 S. E. Atanasov, B. Kalanyan and G. N. Parsons, *J. Vac. Sci. Technol. A Vacuum, Surfaces, Film.*, 2016, **34**, 01A148.

99 Y. Zheng, S. Hong, G. Psofogiannakis, G. B. Rayner, S. Datta, A. C. T. Van Duin and R. Engel-Herbert, *ACS Appl. Mater. Interfaces*, 2017, **9**, 15848–15856.

100 J. W. Shin, M. H. Kang, S. Oh and J. An, *Nanotechnology*, 2018, **29**, 195602.

101 S. McDonnell, A. Pirkle, J. Kim, L. Colombo and R. M. Wallace, *J. Appl. Phys.*, 2012, **112**, 104110.

102 X. Wang, Y. Ishii, A. R. Ruslinda, M. Hasegawa and H. Kawarada, *ACS Appl. Mater. Interfaces*, 2012, **4**, 3526–3534.

103 J. Raymakers, K. Haenen and W. Maes, *J. Mater. Chem. C*, 2019, **7**, 10134–10165.

104 D. Zhu, J. A. Bandy, S. Li and R. J. Hamers, *Surf. Sci.*, 2016, **650**, 295–301.

105 M. Chandran, M. Shasha, S. Michaelson and A. Hoffman, *Appl. Phys. Lett.*, 2015, **107**, 2–6.

106 A. K. Tiwari, J. P. Goss, P. R. Briddon, N. G. Wright, A. B. Horsfall, R. Jones, H. Pinto and M. J. Rayson, *Phys. Status Solidi Appl. Mater. Sci.*, 2012, **209**, 1709–1714.

107 J. J. Alcantar-Peña, E. de Obaldia, P. Tirado, M. J. Arellano-Jimenez, J. E. Ortega Aguilar, J. F. Veyan, M. J. Yacaman, Y. Koudriavtsev and O. Auciello, *Diam. Relat. Mater.*, 2019, **91**, 261–271.

108 J. T. Paci, T. K. Minton and G. C. Schatz, *Acc. Chem. Res.*, 2012, **45**, 1973–1981.

109 A. Poghossian, M. H. Abouzar, A. Razavi, M. Bäcker, N. Bijnens and O. A. Williams, *Electrochim. Acta*, 2009, **54**, 5981–5985.

110 X. Jin, L. Si and M. Qu, *Surf. Interface Anal.*, 2019, 1–7.

111 H. B. Man and D. Ho, *Phys. Status Solidi Appl. Mater. Sci.*, 2012, **209**, 1609–1618.

112 J. C. Pinero, D. Araújo, A. Fiori, A. Traoré, M. P. Villar, D. Eon, P. Muret and J. Pernot, *Appl. Surf. Sci.*, 2017, **395**, 200–207.

113 T. T. Pham, M. Gutiérrez, C. Masante, N. Rouger, D. Eon, E. Gheeraert, D. Araùjo and J. Pernot, *Appl. Phys. Lett.*, 2018, **112**, 102103-1–4.

114 P. Strobel, J. Ristein and L. Ley, *Diam. Relat. Mater.*, 2008, **17**, 1362–1366.

115 M. Wang, N. Simon, C. Decorse-Pascanut, M. Bouttemy, A. Etcheberry, M. Li, R. Boukherroub and S. Szunerits, *Electrochim. Acta*, 2009, **54**, 5818–5824.

116 J. Navas, D. Araujo, J. Carlos, A. Sánchez-coronilla, E. Blanco, P. Villar, R. Alcántara, M. Florentin, D. Eon and J. Pernot, *Appl. Surf. Sci.*, 2018, **433**, 408–418.

117 T. Kageura, K. Kato, H. Yamano, E. Suaebah, M. Kajiya, S. Kawai, M. Inaba, T. Tanii, M. Haruyama, K. Yamada, S. Onoda, W. Kada, O. Hanaizumi, T. Teraji, J. Isoya, S. Kono and H. Kawarada, *Appl. Phys. Express*, 2017, **10**, 055503.

118 X. M. Zheng and P. V Smith, *Surf. Sci.*, 1992, **262**, 219–234.

119 Z. Shpilman, I. Gouzman, E. Grossman, L. Shen, T. K. Minton and A. Hoffman, *Appl. Phys. Lett.*, 2009, **95**, 174106.

120 D. Petrini and K. Larsson, *J. Phys. Chem. C*, 2007, **111**, 795–801.

121 H. X. Yang, L. F. Xu, C. Z. Gu, Z. Fang, S. B. Zhang and M. Chshiev, *Surf. Sci.*, 2009, **603**, 3035–3040.

122 H. Ye, M. Kasu, K. Ueda, Y. Yamauchi, N. Maeda, S. Sasaki and T. Makimoto, *Diam. Relat. Mater.*, 2006, **15**, 787–791.

123 A. Daicho, T. Saito, S. Kurihara, A. Hiraiwa and H. Kawarada, *J. Appl. Phys.*, 2014, **115**, 223711-1–4.

124 Z. Ren, G. Yuan, J. Zhang, L. Xu, J. Zhang, W. Chen and Y. Hao, *AIP Adv.*, 2018, **8**, 065026.

125 K. K. Kovi, S. Majdi, M. Gabrysch and J. Isberg, *Appl. Phys. Lett.*, 2014, **105**, 1–6.

126 K. K. Kovi, S. Majdi, M. Gabrysch, N. Suntornwipat and J. Isberg, *ECS Trans.*, 2015, **69**, 61–65.

127 Z. Ren, D. Lv, J. Xu, J. Zhang, J. Zhang, K. Su, C. Zhang and Y. Hao, *Appl. Phys. Lett.*, 2020, **116**, 013503.

128 N. C. Saha and M. Kasu, *Diam. Relat. Mater.*, 2019, **91**, 219–224.

129 D. Kueck, P. Leber, A. Schmidt, G. Speranza and E. Kohn, *Diam. Relat. Mater.*, 2010, **19**, 932–935.

130 A. Hiraiwa, T. Saito, D. Matsumura and H. Kawarada, *J. Appl. Phys.*, 2015, **117**, 215304.

131 H. Kawarada, H. Tsuboi, T. Naruo, T. Yamada, D. Xu, A. Daicho, T. Saito and A. Hiraiwa, *Appl. Phys. Lett.*, 2014, **105**, 013510.

132 X. Liang, G. D. Zhan, D. M. King, J. A. McCormick, J. Zhang, S. M. George and A. W. Weimer, *Diam. Relat. Mater.*, 2008, **17**, 185–189.

133 A. W. Weimer, *J Nanopart Res*., 2019, **21**.

134 S. Saito, K. Torii, Y. Shimamoto, S. Tsujikawa and E. Al, *Appl. Phys. Lett.*, 2004, **84**, 1395.

135 J. Li and T. P. Ma, *J. Appl. Phys.*, 1987, **62**, 4212.

136 Y. Zhao, G. C. Wang, T. M. Lu, G. Palasantzas and J. Hosson, *Phys. Rev. B - Condens. Matter Mater. Phys.*, 1999, **60**, 9157–9164.

137 Y. S. Kim, M. Y. Sung, Y. H. Lee, B. K. Ju and M. H. Oh, *J. Electrochem. Soc.*, 1999, **146**, 3398–3402.

138 M. C. V Lopes, S. G. Dos Santos, M. Hasenack and V. Baranauskas, *J. Electrochem. Soc.*, 1996, **143**, 1021–1025.

139 S. Roy, V. K. Balla, A. K. Mallik, V. G. Ralchenko, A. P. Bolshakov, E. E. Ashkinazi and N.

Dandapat, *Mater. Today Proc.*, 2018, **5**, 9846–9854.

140 E. L. H. Thomas, O. A. Williams, G. W. Nelson, S. Mandal and J. S. Foord, *Carbon N. Y.*, 2014, **68**, 473–479.

141 S. Mandal, E. L. H. Thomas, L. Gines, D. Morgan, J. Green, E. B. Brousseau and O. A. Williams, *Carbon N. Y.*, 2018, **130**, 25–30.

142 J. R. Weber, A. Janotti and C. G. Van De Walle, *J. Appl. Phys.*, 2011, **109**, 033715.

143 F. Werner and J. Schmidt, *Appl. Phys. Lett.*, 2014, **104**, 091604.

144 S. Gierałtowska, Ł. Wachnicki, B. S. Witkowski, M. Godlewski and E. Guziewicz, *Opt. Appl.*, 2013, **43**, 17–25.

145 J. T. Gaskins, P. E. Hopkins, D. R. Merrill, S. R. Bauers, E. Hadland, D. C. Johnson, D. Koh, J. H. Yum, S. Banerjee, B. J. Nordell, M. M. Paquette, A. N. Caruso, W. A. Lanford, P. Henry, L. Ross, H. Li, L. Li, M. French, A. M. Rudolph and S. W. King, *ECS J. Solid State Sci. Technol.*, 2017, **6**, N189–N208.

146 M. H. Cho, Y. S. Roh, C. N. Whang, K. Jeong, S. W. Nahm, D. H. Ko, J. H. Lee, N. I. Lee and K. Fujihara, *Appl. Phys. Lett.*, 2002, **81**, 472–474.

147 J. W. Liu, M. Y. Liao, M. Imura, E. Watanabe, H. Oosato and Y. Koide, *J. Phys. D. Appl. Phys.*, 2014, **47**, 245102.

148 J. Yang, Y. Zhang, Q. Wu, C. Dussarrat, J. Qi and W. Zhu, *IEEE Trans. Electron Devices*, 2019, **66**, 3382–3386.

149 L. Q. Zhang and P. F. Wang, *Jpn. J. Appl. Phys.*, 2018, **57**, 096502 1–3.

150 K. Yim, Y. Yong, J. Lee, K. Lee, H. Nahm, J. Yoo, C. Lee, C. S. Hwang and S. Han, *NPG Asia Mater.*, 2015, **7**, e190.

151 S. M. Lee, Y. Jang, J. Jung, J. H. Yum, E. S. Larsen, C. W. Bielawski, W. Wang, J. Ryou, H. Kim and H. Cha, *Appl. Surf. Sci.*, 2019, **469**, 634–640.

152 N. Ramanan, B. Lee and V. Misra, *Semicond. Sci. Technol.*, 2015, **30**, 125017.

153 R. I. Hegde, D. H. Triyoso, S. B. Samavedam and B. E. White, *J. Appl. Phys.*, 2007, **101**, 074113-1–7.

154 T. Wang and J. G. Ekerdt, *J. Electrochem. Soc.*, 2011, **158**, G185.

155 H. Kim, H. B. R. Lee and W. J. Maeng, *Thin Solid Films*, 2009, **517**, 2563–2580.

156 W. Wang, M. Tsai, Y. Lin, Y. Tsai, H. Lin and M. Chen, *Mater. Chem. Phys.*, 2016, **184**, 291–297.

157 A. Maréchal, M. Aoukar, C. Vallée, C. Rivière, D. Eon, J. Pernot and E. Gheeraert, *Appl. Phys. Lett.*, 2015, **107**, 0–5.

158 J. W. Liu, M. Y. Liao, M. Imura and Y. Koide, *Appl. Phys. Lett.*, 2012, **101**, 1–5.

159 J. Liu, M. Liao, M. Imura, H. Oosato, E. Watanabe and Y. Koide, *Diam. Relat. Mater.*, 2015, **54**, 55–58.

160 J. W. Liu, M. Y. Liao, M. Imura, R. G. Banal and Y. Koide, *J. Appl. Phys.*, 2017, **121**, 224502.

161 J. W. Liu, M. Y. Liao, M. Imura, H. Oosato, E. Watanabe, A. Tanaka, H. Iwai and Y. Koide, *J. Appl. Phys.*, 2013, **114**, 084108.

162 Y. F. Wang, W. Wang, X. Chang, F. Wen, H. N. Abbasi, R. Wang, J. Fu, Z. Liu, D. Zhao and H. X. Wang, *Diam. Relat. Mater.*, 2019, **99**, 1–5.

163 J. W. Liu, M. Y. Liao, M. Imura and Y. Koide, *J. Appl. Phys.*, 2016, **120**, 124504.

164 G. D. Wilk, R. M. Wallace and J. M. Anthony, *J. Appl. Phys.*, 2001, **89**, 5243–5275.

165 E. . Kraut, R. . Grant, J. . Waldrop and S. . Kowalczyk, *Phys. Rev. Lett.*, 1980, **44**, 1620–1623.

166 V. V. Afanas'ev, *Adv. Condens. Matter Phys.*, 2014, **2014**, 301302.

167 J. Robertson, *J. Vac. Sci. Technol. A Vacuum, Surfaces, Film.*, 2013, **31**, 050821.

168 J. Liu, M. Liao, M. Imura, A. Tanaka, H. Iwai and Y. Koide, *Sci. Rep.*, 2014, **4**, 2–6.

169 K. Wu, M. Liao, L. Sang, J. Liu, M. Imura, H. Ye and Y. Koide, *J. Appl. Phys.*, 2018, **123**, 161599.

170 O. Romanyuk, I. Bartoš, I. Gordeev, A. Artemenko, M. Varga, T. Ižák, M. Marton, P. Jiříček and A. Kromka, *Diam. Relat. Mater.*, 2018, **87**, 208–214.

171 J. P. Chou, A. Retzker and A. Gali, *Nano Lett.*, 2017, **17**, 2294–2298.

Chapter 2: Interface Quality of ALD Alumina Films with Polycrystalline Diamond

1.0 Introduction

The renowned properties of diamond propel research for its use in microelectronic devices especially for high frequency, high power and high temperature applications, and for use in harsh environments where these conditions prevail[1]. Diamond films achieve bulk conductivity by doping with B for p-type, and P or N for n-type conductivity[2], but surface conductivities have also been attained via surfaces terminations and adsorbates. Typically, H-terminated diamond surfaces result from cooling in H_2 plasma from temperatures of approximately 800 ^{o}C, subsequent to film growth by CVD techniques[3], and NO_2 adsorbates on H-terminated diamond were shown to enhance film surface conductivity via a 2DHG[4,5]. Surface passivation by ALD Al_2O_3 (alumina) resulted in stabilization of hole concentrations during heating and cooling from room temperature up to 400 ^{o}C[4].

Diamond film MOS devices relying on either surface or bulk conductivity, however, require fabrication of a thin dielectric layer on the film surface, below the metal contact, to control charge carriers and minimize leakage currents. Al_2O_3 is typically used for this layer, having valence and conduction band offsets >1 eV with H-terminated diamond[6], the minimum required for preventing Schottky emission of charge carriers into the oxide band[7]. In addition, Al_2O_3 has been widely researched both practically and theoretically in literature for fabrication of layers a few nanometres thick by ALD, on a host of different substrates having different aspect ratios and surface functional groups[8-11]. In general, the electrical properties of MOS devices are reported, but minimal literature exists for understanding the mechanical stability of the high-κ/diamond interface, which may be dependent on the surface termination of diamond.

Surface ligands of Si and Ge semiconductors have demonstrated differences in nucleation behaviour associated with ALD Al_2O_3. –O and –OH on Si were determined to be reactive toward dissociative chemisorption of Al precursor, trimethylaluminium (TMA), and the presence of mobile H as –OH surface groups maximized the amount of Al deposited in each cycle by successful elimination of CH_4 during TMA exposure[8]. Furthermore, ALD Al_2O_3 on H-terminated Ge and Si exhibited island growth nucleation which resulted in a defective dielectric/semiconductor interface, while ALD Al_2O_3 on an oxidized Ge surface resulted in an Al_2O_3/GeO_x intermixing layer, making a high quality interface with Ge, characterized by low gate leakage, small C-V hysteresis and low interface trap density[10,12].

Manipulation of the diamond surface, as performed for Ge and Si, can therefore provide a path towards optimization of the high-κ/diamond interface. Research has focused on the manipulation of diamond surface terminations to tune the electronic structure of diamond films, and minimize leakage currents through the high-κ/diamond interface. The control of O adsorption onto H-terminated diamond

demonstrated tuneable band bending up to about 360 meV[13], and MOSCAPs utilizing B doped, O-terminated single crystal diamond were shown to be completely gate controlled and demonstrated a non-detectable leakage current[14]. It is apparent however, that diamond surface manipulation may have consequences to both interface mechanical stability and electronic properties, requiring a compromise to be selected. Overall, these results are promising for manipulation of the diamond surface to accommodate high-κ layers in optimized transistors, targeted for niche applications such as, in mechanically stressful environments where electronics are subject to dynamic structural shock, including during spacecraft launch, satellite ejection, re-entry vehicles, deep-well drilling and geothermal exploration[1]. The electronic integrity of the high-κ/semiconductor interface is therefore crucial to these applications in which diamond devices are expected to operate, but also important is the mechanical stability of these interfaces which has yet to be explored.

Nanoindentation analysis has been utilized for determining the mechanical properties of binary oxide and composite nano films[15,16]. It is however also useful for characterizing interfacial toughness especially when the critical limit of delamination can be achieved, identified by the formation of buckles[16]. Chemical bonding at the interface influences the adhesion of the dielectric on the semiconductor since it depends directly on interatomic forces, which also include physical adsorption and electrostatic forces[17,18], attesting to the importance of surface ligands for achieving a chemisorbed, as opposed to a physisorbed, dielectric layer. This type of analysis poses a challenge for the rough, heterogeneous surface of polycrystalline films and has been cautioned against as it tends to underestimate the values of elastic modulus, E and hardness, H, by overestimating the indenter contact area with the film surface[19]. Nanoindentation is performed in this work to determine the adhesive behaviour of alumina thin films, deposited by ALD, on O_2 plasma treated and as-grown surfaces of polycrystalline BDD, thereby analysing the mechanical interfacial integrity of the film. Attempting to induce film delamination by the indenter at different applied loads can reveal this behaviour and the critical load required for interface separation[16]. As the goal of this work does not involve attaining absolute values of E and H, the rough BDD surfaces are used for analysis and the limitations imposed discussed. The novelty of this experimental work therefore lies in the use of an O_2 plasma treatment on the surface of polycrystalline BDD, to enhance its interfacial mechanical stability with AlO films fabricated by ALD, and on the use of nanoindentation analysis to evidence the resultant improvement.

2.0 Experimental Procedure

2.1. Growth of B-doped Diamond Films

Si p-type <100> substrates, approximately 1 cm^2, were cleaned in isopropanol using ultrasonication for 10 minutes, and dried in a stream of compressed air. They were subsequently seeded with diamond particles measuring 40-60 µm; each sample was placed in a separate beaker containing a suspension of 0.5 g diamond particles and 5 ml ethanol, and underwent ultrasonication for 1 hour. The samples were then removed from the diamond particle suspensions and cleaned by rinsing in flowing ethanol, and ultrasonication in ethanol for 2 minutes, twice, each time changing the ethanol.

BDD was grown onto the seeded Si by HFCVD using a custom-built system (Figure 7(A)). Substrates were placed onto the sample stage in the HFCVD chamber, under at least two tungsten filaments; in total five tungsten, 0.3 mm diameter filaments were used in this deposition, and the stage was placed at least 10 mm from the filaments during this first stage of carburization. The chamber was evacuated and 6 % CH_4/H_2 was introduced into the chamber until a pressure of 7.5 kPa was attained. Carburization of the filaments was achieved at 2250 ^{o}C after about 20 minutes. The sample stage was then raised to approximately 6 mm from the filaments and the flow ratio CH_4/H_2 was set to 5 %. The power through the filaments was increased to achieve a substrate temperature of 800 ^{o}C. Diamond growth proceeded for a total of 60 minutes; the B precursor was only introduced during the last 45 minutes of growth. The substrate temperature was maintained between 785-800 ^{o}C, and B precursor and carrier gas flow rates of 0.025 μl/min B_2O_3 in ethanol (10 000 ppm) and 4 ml/min Ar, respectively, were used. At the end of the total one-hour growth, all the gases were turned off except H_2, and the power through the filaments was slowly decreased until zero or until the filaments broke. H_2 was set to zero and the chamber was again evacuated and allowed to cool until room temperature.

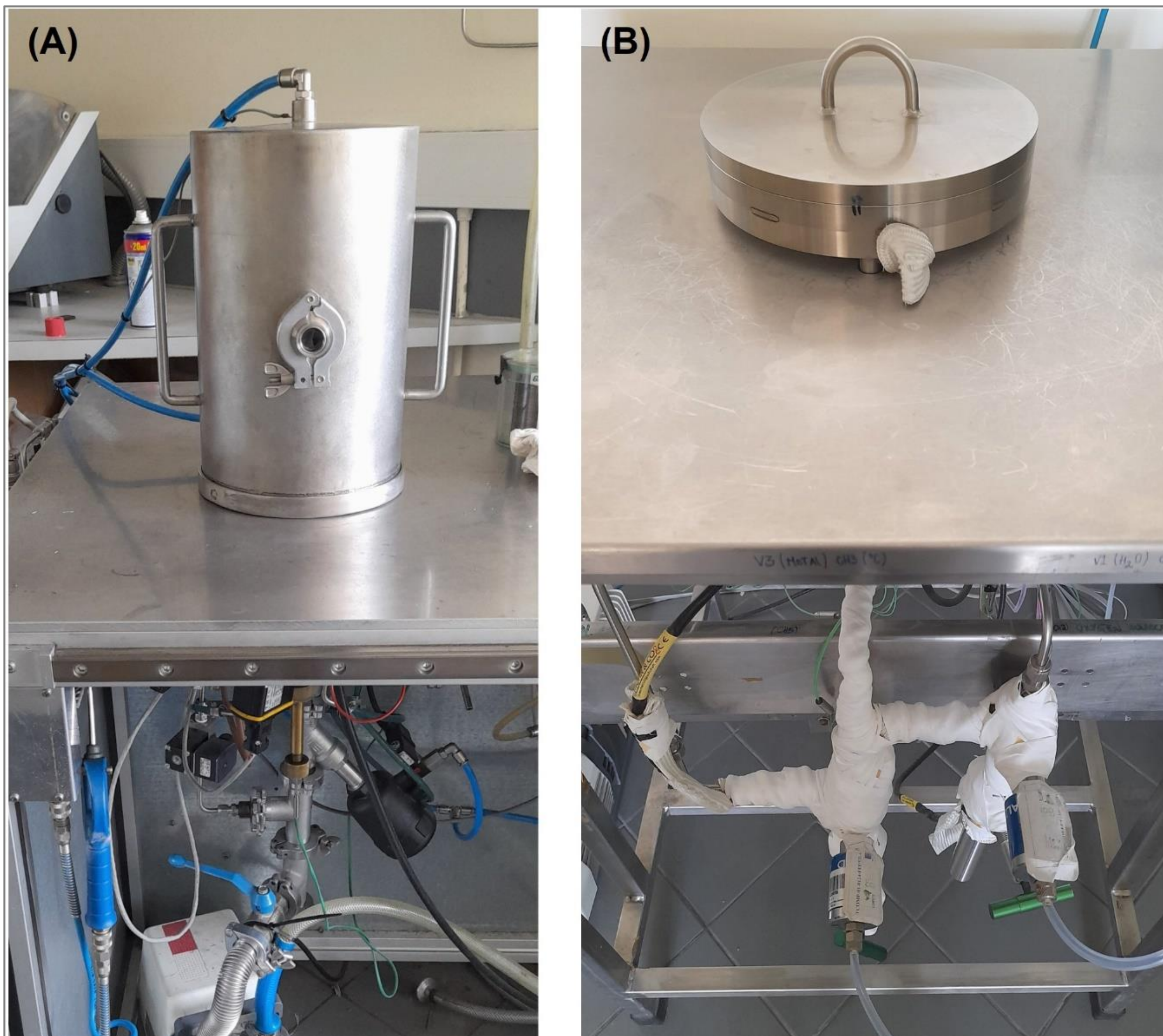

Figure 7: (A) HFVCD and (B) ALD systems at the Department of Materials and Ceramic Engineering at Universidade de Aveiro

2.2. Deposition of Alumina Thin Films by ALD

Some of the as-grown BDD samples were exposed to O_2 plasma at a power of 100 W for 10 minutes (O-BDD), using an EMITECH K1050X Plasma system, with the intention of increasing the quantity of O surface ligands.

O-BDD and H-BDD (as-grown BDD) samples were placed into a custom-built ALD reactor Figure 7(B)) and heated to the deposition temperature of 200 ^{o}C. Piranha surface treated Si substrates were also put into the chamber for use as the control in analysis. TMA (Sigma Adrich, 97%) and deionized water were used as the precursors of Al and O, respectively, and were kept in separate stainless-steel canisters at room temperature. One cycle was defined by 20 s N_2 purging, followed by 4 s TMA exposure (0.05 s of pulse time), 20 s N_2 purging, then 6 s H_2O exposure (0.1 s of pulse time).

1000 cycles were carried out on the O-BDD and H-BDD surfaces, resulting in an alumina thin film on each, henceforth referred to as AlO-O-BDD and AlO-H-BDD, respectively. At the end of the 1000 cycles the precursor gas valves were closed and the chamber purged for 20 cycles. Samples were cooled until room temperature in the chamber.

2.3. Characterization Techniques

Scanning electron microscopy (SEM) was performed by Hitachi S4100 and SU70 systems using accelerating voltages 15-25 kV, to determine film surface morphology and any changes due to surface treatment. It was also used to estimate BDD and alumina film thicknesses.

Raman spectra were acquired for H-BDD samples by a Horiba HR800 micro-Raman system in the back-scattering configuration using the blue line (441.6 nm) of a He:Cd laser, to determine sp^2/sp^3 content and thus film quality.

XPS spectra were acquired for H-BDD and O-BDD to determine the composition of surface elements and ligands. An ultra-high vacuum (UHV) system with a base pressure of 2×10^{-11} kPa was used, equipped with a hemispherical electron energy analyzer (SPECS Phoibos 150), and a monochromatic X-ray source Al Kα (1486.74 eV). High-resolution spectra were recorded at normal emission take-off angle and with a pass energy of 20 eV.

Alumina film thickness was obtained from X-ray reflectometry (XRR) analysis on ALD alumina films on Si substrates, using Philips X'Pert MRD X-ray diffractometer with Cu radiation and a graphite monochromator, for the selection of pure Kα radiation. The X-ray tube was operated at 40 kV and 50 mA. Film crystallinity of ALD alumina on Si was determined by GIXRD analysis, performed on a Philips X'Pert MRD X-ray diffractometer with a Cu anode. Measurements were recorded for 2θ angles between 10–75 ^{o} and scan step of 0.03 ^{o}.

Alumina films on Si were also characterized by Fourier-transform infrared spectroscopy (FTIR) using Bruker Tensor 27 equipment, 1024 scans in the range 4000-350 cm^{-1} with a resolution of 4 cm^{-1}. ATR (attenuated total reflection) mode was used with a Golden Gate diamond accessory. This was done to obtain the chemical bonding and functional groups present in the alumina film.

Nanoindentation was used to determine differences in the mechanical behaviour of the alumina films due to the differences in the interfaces of AlO-H-BDD and AlO-O-BDD. A three-sided pyramidal Berkovich diamond indenter, with a 20 nm edge radius and 65.3^{o} faces from the vertical axis, attached to a fully calibrated TTX-NHT, CSM instruments Nanoindenter, was used for this analysis. The experiments were performed at maximum normal applied loads of 5 mN, 10 mN, 20 mN, 30 mN, 50 mN, 75 mN, 100 mN, 125 mN and 150 mN, with an approach speed of 2000 nm/min and dwell time of 10 s. Further, the indentation impressions were recorded with the aid of an optical microscope, and an AFM, Veeco AFM Multimode Nanoscope (IV) MMAFM-2, with conductive Si cantilevers from Nanosensors, using a nominal force constant 15 N/m probe.

AlO-H-BDD and AlO-O-BDD samples were prepared for cross-section analysis by TEM using mechanical polishing, and Ar+ beam ion milling, using Precision Ion Polishing System (PIPS). Scanning (STEM) and high resolution (HRTEM) analysis were performed using an FEI Talos F200S system. Micrographs were captured with an accelerating voltage of 200 keV. High angle annular dark field

(HAADF) micrographs were also obtained, which exhibits compositional sensitivity proportional to Z^2. Energy dispersive X-ray spectroscopy (EDX) was performed to ascertain the elemental composition and their respective distributions in the samples.

3.0 Results and Discussion

3.1. BDD Thin Films

The HFCVD conditions used for BDD growth resulted in polycrystalline films with an average thickness of 1.6±0.4 μm, as characterized by SEM (Figure 8 (A) and (B)). The measured Raman spectrum is shown in Figure 8(C), the bottom graph is the deconvolution of the curves fitted to the linear baseline adjusted data of the top graph. The characteristic sp^3 hybridized C diamond peak is present at 1332 cm^{-1} and fitted by a Lorentzian component. The asymmetry of this peak is evident in the top scan, and is known to be due to Fano interference which requires interaction between discrete and continuum energy states, in this case, the discrete scattering from the diamond zone centre phonon and that from its valence band continuum, respectively[20,21]. The film also comprises peaks around 1100 and 1470 cm^{-1}, which are considered to be companion peaks due to polymeric sp^2 C species or transpolyacetylene at the grain boundaries; the former has also been associated with the presence of nanocrystalline diamond[22,23]. Peaks at 1350 and 1540 cm^{-1} are known to be allocated to the D and G bands of sp^2 C graphite, respectively. The D band is associated with the breathing modes and therefore presence of sp^2 C atoms arranged in rings, whereas the G band is associated with the in-plane stretching of sp^2 C pairs, which incorporates those of both chain and ring arrangements[24]. The peak at 1610 cm^{-1} has been identified as part of the G band of graphite[23] but also labelled as the D' peak, which merges with the G peak for small grain sizes, and characterizes the loss of 3-dimensional ordering of the film structure[24]. The spectrum also shows a peak centred around 1220 cm^{-1} which coincides with the main maximum phonon density of states for diamond[20], and is predominantly assessed for B incorporation into the diamond lattice, or at least the film[21,23,25]. Peaks at 520 and 970 cm^{-1} are contributions from Si[20] due to the substrate and possibly from impurities incorporated into the film during HFCVD.

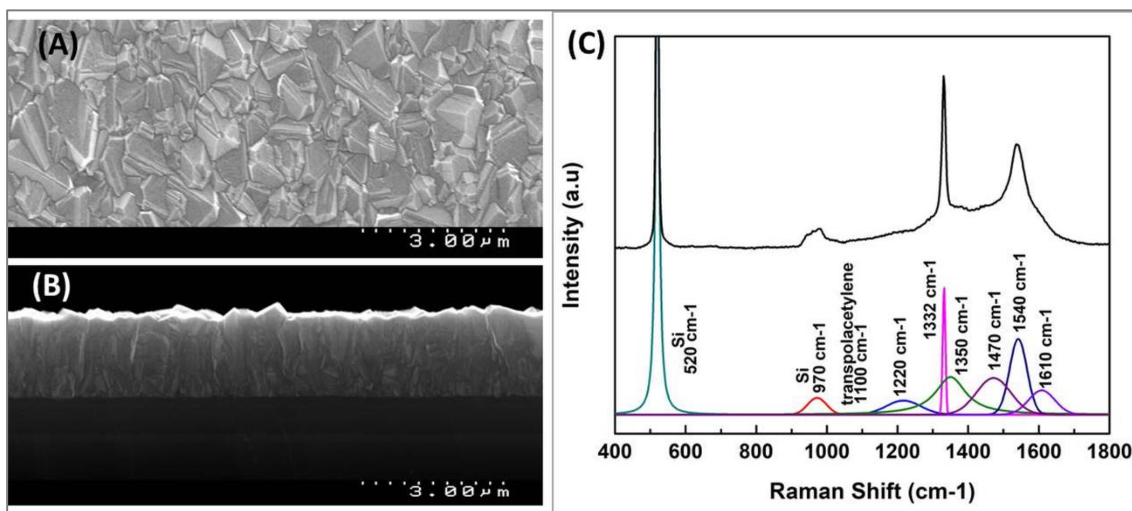

Figure 8: (A) surface image of as-grown BDD showing polycrystalline morphology; (B) cross-section SEM image of as-grown BDD with average thickness in the range 1.6±0.4 µm; (C) Raman spectrum of as-grown BDD identifying film composition which includes, sp^3 C diamond, sp^2 C from D and G bands of graphite, polymeric sp^2 C and B incorporation.

Figure 9 shows XPS spectra and the respective SEM images (inset) before and after BDD film exposure to the O_2 plasma; the latter demonstrates no obvious influence of the treatment on film morphology, so that H-BDD and O-BDD are considered similar in this aspect. XPS measurements were performed to characterize differences in the surface chemical composition of H-BDD and O-BDD. Analysis of the C1s peak prior to deconvolution revealed that for both samples there are two main contributions, one for the BDD structure occurring at a lower binding energy (BE), and the other for its surface ligands at a higher BE. The larger peak occurs around 284.3 eV for H-BDD, and at a higher BE of 284.7 eV for O-BDD, attributed to a non-hydrogenated diamond surface[26]. Shifting of the core level C peak towards higher BE for O-BDD, is caused by the change in oxidation state of C when bonded to O. Compared to C, O is more electronegative and therefore increases the oxidation state of C when bonded. The core level peak of C is therefore shifted to a higher BE because the photo emitted electron experiences greater coulombic interactions with the nucleus of the ion, and must therefore overcome a higher energy to be emitted. In this analysis the C1s peak for O-BDD has been subsequently positioned at 284.3 eV for better comparison of the surface ligands with H-BDD.

The larger C1s peak for both samples can be deconvoluted into 2 contributions, the major is due to C-C/C-H groups from sp^3 hybridized C and other species associated with defects and grain boundaries[27,28], and a smaller contribution at lower BE from sp^2 hybridized graphite, typically assigned to peaks positioned at BEs 0.8–1.3 eV lower than that of sp^3 C[29,30]. Si-C has been shown to occur at lower BE, around 1.7 eV from the sp^3 C peak[31], but this is not evident in the C1s peak. The Si 2p signal however was attained in the wide scan spectrum for both samples (not shown) suggesting that Si from the seeded surface was grown into BDD during HFCVD, into the superficial layers. This incorporation could be the result of etching of the Si by highly reactive plasma during BDD nucleation, resulting in its presence in the diamond structure or graphitic grain boundaries[32,33].

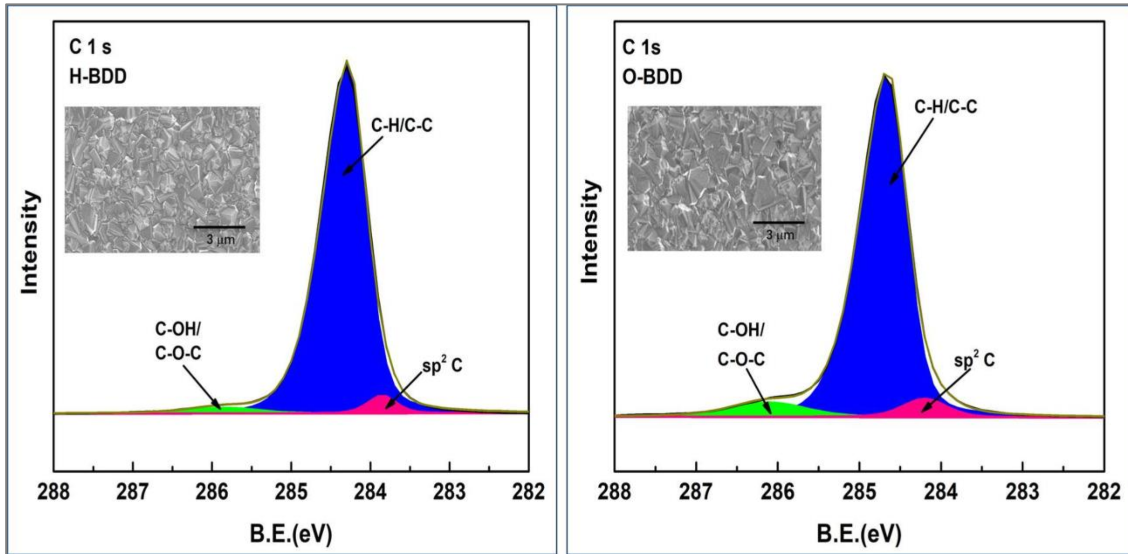

Figure 9: Comparison of H-BDD and O-BDD surfaces by XPS, main contributions are from the structure of BDD, which include C-C/C-H bonding and sp^2 C, and the surface C-OH/C-O-C ligands, which contribute a larger percentage ratio for O-BDD. Inset SEM images demonstrate no change in the morphology due to O_2 plasma treatment.

The C1s contribution occurring at higher BE is shown for both H-BDD and O-BDD. This contribution is due to the surface ligands of BDD from hydroxyl or ether groups, centred at 285.8 eV and 285.7 eV for H-BDD and O-BDD, respectively, within the energy range expected for these groups, 1.2-1.6 eV higher than the C-H/C-C contribution[29,34]. C-OH/C-O-C (ether) surface ligands on H-BDD are likely the result of the BDD growth process, as the use of B precursor, B_2O_3, dissolved in ethanol has been shown to produce some oxygen surface bonds[35]. Adsorbed molecules can also be considered, as there was a duration of 24 hours between BDD growth and XPS measurements although, diamond H-termination, as a result of CVD growth conditions, is known to be stable in air with slow oxidation over time[27].

The C1s peak for O-BDD shows a larger contribution from the C-OH/C-O-C surface ligands. The O_2 plasma treatment of the surface is expected to introduce O bonds on the BDD surface, the type of which varies depending on the crystallographic orientation of the grains at the surface[36,37]. The presence of only one peak suggests that even for an inhomogeneous polycrystalline surface with grain boundaries and defects, only C-OH and/or C-O-C (ether) groups are favoured.

Analysis of the areas under the peaks provides the relative contribution of the C surface ligands to that of the C of the bulk diamond. This is achieved using the equation:

$$\%\,Surface\ ligands = \frac{A_{OH/CO}}{A_{OH/CO}+A_{sp2\ C/CC/CH}} \qquad (4)$$

$A_{OH/CO}$ represents the area contributed by surface ligands, C–OH and C-O-C, and $A_{sp2\ C/CC/CH}$ represents the area contributed by the BDD film structure. It was therefore shown using equation (4)

that the oxygen-based surface ligands contributed approximately 2 % of C in H-BDD, while they accounted for 5 % in O-BDD.

3.1 ALD Alumina Thin Films

Alumina films deposited by ALD conformed to the uneven polycrystalline diamond surface for both AlO-H-BDD and AlO-O-BDD samples, as confirmed by the SEM images of Figure 10. An average thickness of the alumina film after 1000 ALD cycles was determined from SEM analysis to be 146±4 nm. The thickness was also calculated to be 139.27±0.75 nm using the spacing of the Kiessig fringes from XRR analysis (Figure 11(A)), and applying it to an equation derived from Snell's law for a medium-air interface. Although similar, the discrepancy between these two ranges result from differences in the accuracy of the measurement techniques, as well as the differences in the substrate of the alumina films. XRR measurements were performed on relatively flat alumina films on Si substrates, while measurements performed by SEM were done on alumina deposited on BDD films, which, due to the conformal nature of ALD films, meant that the alumina films imitated the roughness of the BDD surface. The error associated with the latter is therefore more significant.

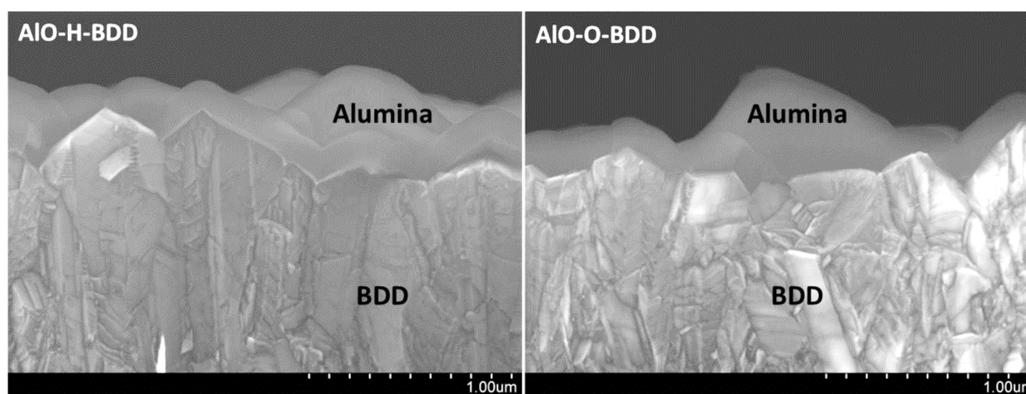

Figure 10: Interface images taken by SEM of ALD alumina on as-grown (left) and surface O_2 plasma functionalized (right) BDD films showing the conformal deposition of the film; average alumina film thickness by SEM was 146±4 nm.

The alumina films were also determined to be amorphous by GIXRD analysis as the diffractogram (Figure 11(B)) exhibited only a peak around 55 ^{o} which is a signal from the Si substrate[38,39]. Chemical composition of the alumina film was investigated by FTIR. The absorption spectrum in Figure 11(C) showed largely the contribution from the fingerprint region at lower wavenumbers. Absorbance peaks at 500 and 550 cm^{-1} are assigned to the stretching modes of octahedral $Al\text{-}O_6$ bonding, those around 775 and 875 cm^{-1} are assigned to the stretching modes of tetrahedral bonds of $Al\text{-}O_4$, while the peak at 609 cm^{-1} is assigned to bending modes of $Al\text{-}O_2$[40-42]. The amorphous nature of the alumina films is synonymous with a short-range order of Al-O bonds so that the presence of octahedral, tetrahedral and other Al-O bonding is expected in the film and evidenced by the FTIR absorbance spectrum. The peak at 1108 cm^{-1} has been associated with the presence of Si-O[43]. Functional

groups in the film are characterized by the absorbance peaks at higher wavenumbers, which are few in the analyzed samples. The peak at 1460 cm^{-1} is assigned to H_2O bridging of Al atoms bonded in AlO_4 or AlO_6[44], and those at 1996 and 2115 cm^{-1}, to terminal carboxyl groups or those covalently bonded to Al[45]. The absorption band around 2300 cm^{-1} is due to the presence of CO_2[40].

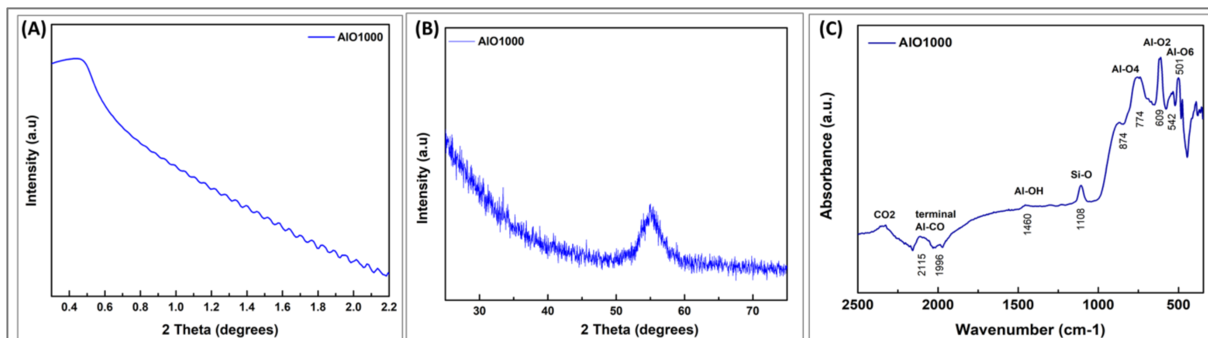

Figure 11: Characterization of alumina film fabricated by 1000 ALD cycles; (A) XRR fringe separation used to calculated alumina film thickness of 139.27±0.75 nm; (B) X-Ray diffractogram exhibits that the ALD alumina film is amorphous and (C) FTIR spectrum revealing film composition of short range order of 2, 4 and 6 coordinated Al-O, and terminal –CO and –OH groups.

3.2 Interfacial Analysis

Strength of adhesion of the alumina film was investigated by nanoindentation analysis. The indentation marks on the samples resulting from six different maximum normal applied loads in the range 30–150 mN, are shown in Figure 12(A); indentations from loads 5–20 mN were omitted since they did not result in obvious differences between the samples. In both samples larger indentation marks are observed with loads ≥100 mN, however circular buckles are only noticed for AlO-H-BDD for applied loads in the range 100-150 mN. The critical load, marking the onset of plasticity for AlO-H-BDD, occurred at 100 mN, and the largest buckle, with a diameter of about 12 μm, resulted from an applied load of 150 mN. In general, AlO-O-BDD exhibited a greater resistance to deformation from the applied loads, evidenced by smaller indentation marks compared to AlO-H-BDD. Nanoindentation performed on bulk alumina have resulted in surface deformations such as shear-induced localized cracking in the vicinity of the indent, shear band formation inside the indentation cavity, and a radial distribution of critical resolved shear stress[46,47], which could explain the formation of buckles. Buckling deformations exhibiting delamination, however, were also argued as being most common on thin films, <5 μm, such as those in this work, as they facilitate bending more readily than thicker films[16,18]. The latter demonstrates a higher bending stiffness, resulting in shear cracking, which may not necessarily propagate along the interface and lead to delamination[18].

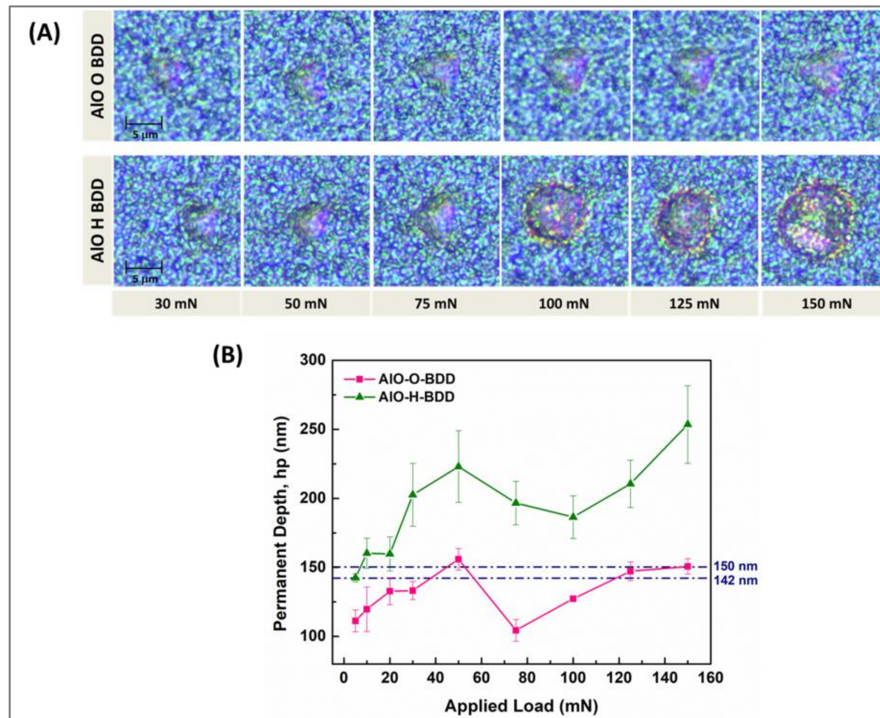

Figure 12: (A) Optical microscope images of indentation marks produced after loading and unloading of loads 30-150 mN onto the respective samples. The top panel shows, from left to right, indentation marks with increasing load strengths on Al-O-BDD while the bottom panel are those for AlO-H-BDD. Each load value is related to its respective top and bottom image and the scale shown holds for all images. (B) Permanent indentation depth, produced by each load in the range 5-150 mN, demonstrates containment in the alumina film or near the interface (dotted lines) for AlO-O-BDD, but beyond the interface for AlO-H-BDD. Each plotted value reflects the mean and standard deviation of three tests performed at the respective maximum normal applied load.

Analysis of permanent indentation depth due to each applied load, confirmed the resistance of AlO-O-BDD to deformation near the interface region. Figure 12(B) provides a graphical representation of the mean permanent indentation depths against the applied loads for both samples. It revealed that across the range of applied loads 5–150 mN, AlO-H-BDD experienced permanent deformation deeper into the sample, compared to AlO-O-BDD. The plastic deformation of AlO-O-BDD was shown to be mainly contained in the 146±4 nm thick alumina film, this range labelled on the graph. Comparatively AlO-H-BDD experienced plastic deformation a further 30-50 nm beyond the alumina film, into the diamond layer, for applied loads less than 100 mN, inclusive, and up to 140 nm beyond the alumina film, for loads greater than 100 mN. These results suggest that exposure to the O_2 plasma facilitated interface elasticity preventing plastic deformation into the BDD film, thereby enabling recovery even after displacements near 1500 nm, shown for the load-displacement curve for 150 mN in Figure 13(A). Further, the presence of an interface region less than 100 nm beyond the measured thickness of the alumina film, could explain the abrupt increase in permanent deformation depths of AlO-H-BDD, for loads larger than 100 mN.

Measurements of elastic indentation modulus, E, and indentation hardness, H, for the samples used in this work, which could have explained to some extent, the deformation behaviour of the

respective films, are complicated by the fact that polycrystalline diamond has a rough surface, and since ALD results in conformal coatings deposited with a constant growth per cycle, the alumina layer mimics the topography of the diamond surface, confirmed by SEM images. E and H are both dependent on the contact area of the indenter on the sample and, for topographical surfaces, there are discrepancies between the real and apparent contact areas. This is because the protruded portions or peaks of the rough surface are more easily deformed by the edges of the indenter tip, thereby deforming an apparently higher contact area[19]. Over and under estimations in the projected contact area due to surface topography therefore prevent accuracy in the values of E and H[19]. Theoretically, it is expected that E and H of the two composite samples will be influenced by the combined properties of the alumina film, BDD film and the Si substrate, with the extent of their relative contributions being dependent on indentation depth[48]. Variations in the exhibited properties of BDD films are apparent in literature, as E for BDD films has been reported in the range 325-600 GPa[28,49], and H for nanocrystalline BDD was determined be between 90-45 GPa for low to highly B doped diamond[28]. Variations in these properties are exacerbated by contributions from grain size, surface topology[19], and B doping[50]. The presence of B atoms is known to reduce the stiffness and hardness of single crystal and polycrystalline diamond because of the lower bond energy, 322.9 kJ mol^{-1}, for B-C, compared to the C-C bond energy of 357.5 kJ mol^{-1} [28,50].

The load-displacement curve for the indentation test which resulted in the maximum permanent depth obtained for AlO-H-BDD, with application of 150 mN, is shown in Figure 13 (A); for comparison, the curve for AlO-O-BDD corresponding to this test, is also shown. The load results in a higher maximum contact depth and permanent indentation depth for AlO-H-BDD, compared to AlO-O-BDD, with differences of 100 nm and 130 nm, respectively. Load-displacement curves for applied loads of 125 and 100 mN for AlO-H-BDD are shown in Figure 13(B) and (C), while the corresponding curves for AlO-O-BDD are shown in Figure 13(D) and (E). The obvious difference in the curves, comparing the two samples, is the larger permanent indentation depth on AlO-H-BDD, as a result of the applied loads. In general, the curves do not reveal large differences such as the presence of discontinuities relating to fractures in the films. A clear difference in the indentation marks and permanent deformation of the samples, when subjected to the 150 mN load, warranted a deeper analysis.

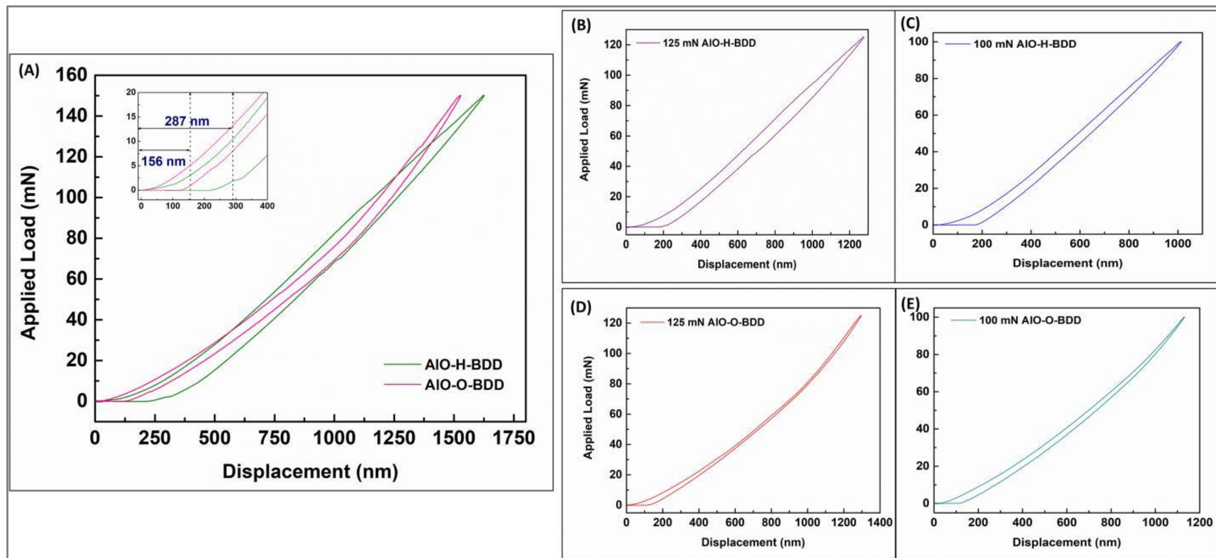

Figure 13: (A) Load-Displacement curve for the maximum normal applied load of 150 mN. Sample displacement results in no major inconsistencies that would identify depths of fractures or delamination; the inset graph demonstrates that the permanent indentation depth occurred deeper into the BDD film for AlO-H-BDD compared to AlO-O-BDD. The permanent depth of 287 nm attained for AlO-H-BDD, was the maximum achieved for all the tests performed at 150 mN. Load-displacement curves for applied loads of 125 and 100 mN, for AlO-H-BDD and AlO-O-BDD, are shown in (B) and (C), and (D) and (E), respectively.

AFM analysis of the residual nanoindentation marks (Figure 14) resulting from the application and removal of the 150 mN load on both samples, highlighted differences in behaviour of the two samples. The circular buckle formed due to loading and unloading of the indenter at 150 mN on AlO-H-BDD (Figure 14(A)) showed film delamination up to an approximate height of 1 μm, covering a maximum radius of approximately 6 μm, from the centre of the indent. The effect of this load on AlO-O-BDD (Figure 14(B)) is a residual nanoindentation mark of the Berkovich tip, about 4 μm long (Figure 14(C)), without delamination, resulting from deformation of the alumina layer. These results are not conclusive in determining the interface from which the film delaminates as it could be due to alumina delamination from the alumina-BDD interface or the composite film delamination from the BDD-Si interface.

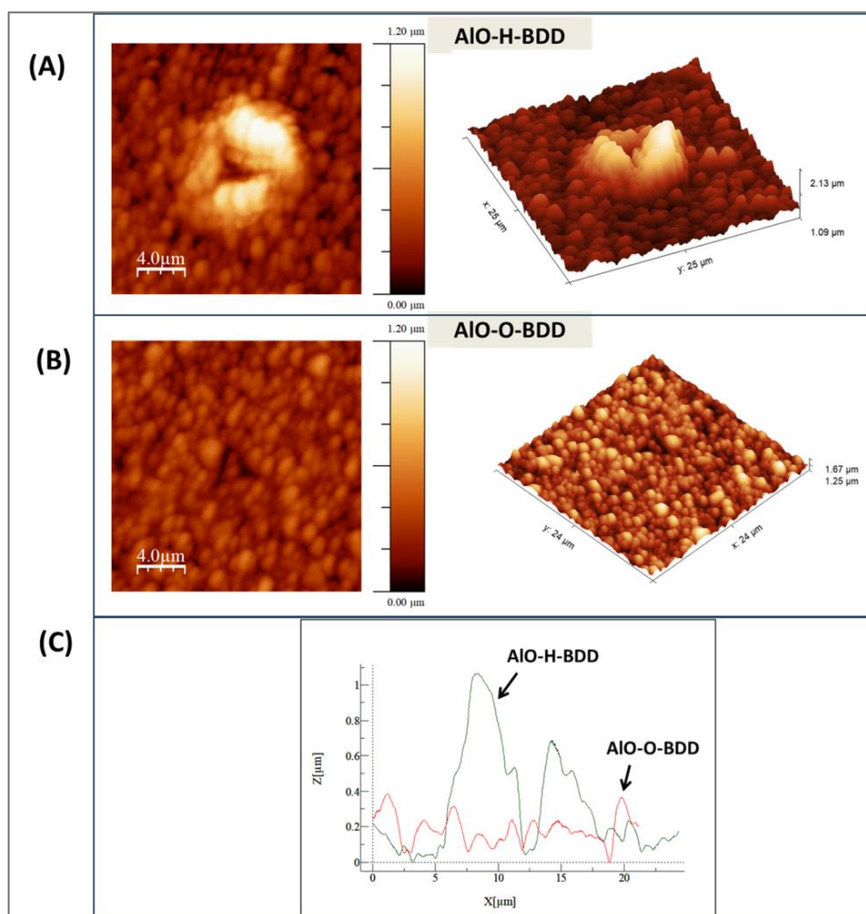

Figure 14: AFM images of (A) AlO-H-BDD and (B) AlO-O-BDD with planar and 3D views of the respective indentation marks resulting from loading and unloading of 150 mN. Only a residual indentation mark of the Berkovich tip is shown on the AlO-O-BDD surface when the load is removed, while a circular buckle is formed on the AlO-H-BDD surface showing film delamination. (C) Demonstrates the height (Z) and radius (X) of the areas of film delamination experienced by AlO-H-BDD and is compared to the less deformed AlO-O-BDD surface.

HRTEM analysis was performed to observe the interfaces of AlO-H-BDD and AlO-O-BDD (Figure 15(A) and (B), respectively). The BDD-Si interface for both samples contained an amorphous layer comprising Si, C and O, confirmed by the graph of Figure 15(C). These elements are attributed to the presence of sp^3 C, Si, Si-O, and Si-C which forms from the carburization of Si when exposed to the reactive CVD plasma[51-53]. The EDX analysis of the alumina-BDD interface (Figure 16) showed that Al, O and C are present in their respective regions for both AlO-H-BDD and AlO-O-BDD. Adherence of the alumina film to the BDD film, for AlO-O-BDD, was sufficient to withstand the polishing and ion milling processes of TEM sample preparation, but this behaviour was not replicated for AlO-H-BDD, which instead experienced cohesive detachment near the BDD surface with a layer of alumina <100 nm remaining on the surface. This could be the effect that is noticed with the indentation at 150 mN for AlO-H-BDD, where delamination occurs due to this failure in cohesive strength.

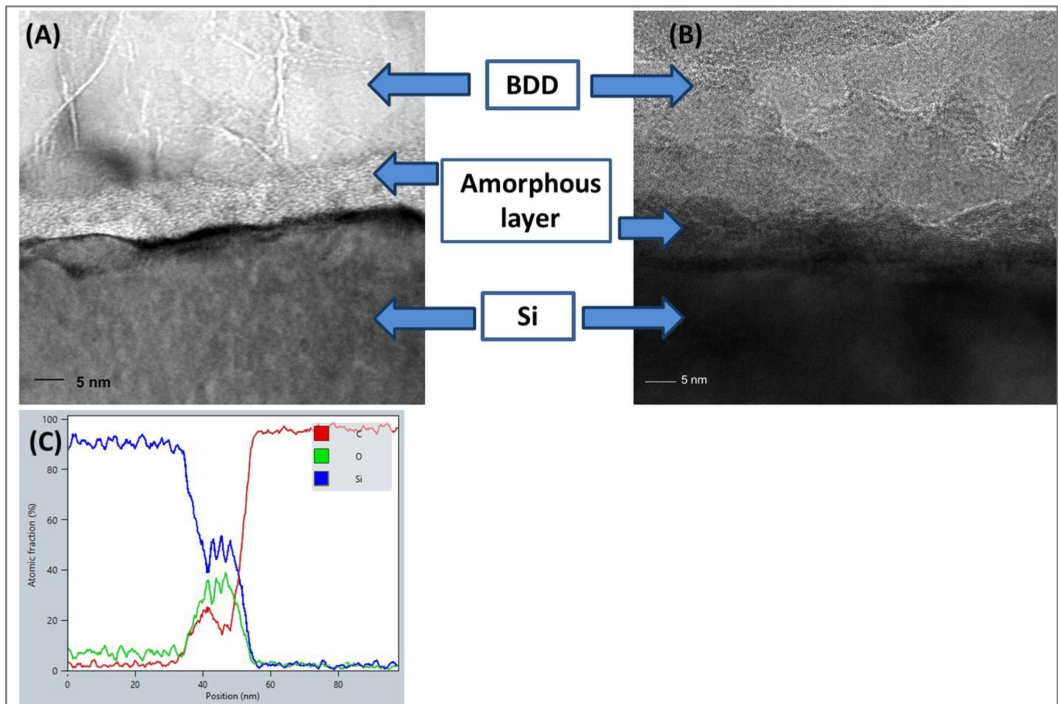

Figure 15: HRTEM micrographs of the BDD-Si interface are shown in (A) for AlO-O-BDD and (B) AlO-H-BDD, an amorphous layer at the interface is present for both samples comprising Si, O and C, determined from the EDX analysis, shown in (C) for AlO-O-BDD.

Alumina film delamination was not apparent from the load-displacement curves due to the absence of discontinuities, which are usual signs of delamination. It is possible that the delamination occurred upon load application or load removal, thus explaining its absence in the load-displacement curve. Literature has discussed, both theoretically and experimentally, that the onset of plasticity in films may occur prior to discontinuities, manifested instead as minor or nanoscale plasticity events, many times unobservable, in the curve, and brought on primarily by the behaviour of defects or dislocations in films, in response to the indenter[54-56]. Structural defects and dislocations in the alumina or polycrystalline BDD films can be propagated upon indentations, and depending on the type of defect and grain orientation, they can vary in their behaviour, as has been demonstrated for other types of films[55,56]. These behaviours include, movement towards the surface, collapse and propagation away from the indenter, or propagation towards and under the indenter forming a dislocation lock, which can decrease the occurrence of a large load drop by confining the dislocation activity[46,55]. This can therefore be a possible explanation, that delamination of the alumina film of AlO-H-BDD occurred due to incipient plasticity of either the alumina or BDD film, the effects of which were minor events, possibly due to the movement of dislocations or shear-induced, localized crack propagation. This effect is prevented in AlO-O-BDD, for the range of applied loads, because of the enhanced interfacial integrity and elasticity imparted by the O_2 plasma treatment, which minimized plastic deformation of the films, evident from the load-displacement curves.

Explanation of the differences in the adhesive and cohesive strengths of the alumina film requires consideration of two influencing factors, the nature of the BDD surface and the reaction kinetics

involved in alumina film ALD. BDD surface moieties were elucidated using XPS, which showed that the main difference was the percentage ratio of surface O bonds to C, with 3 % more present on O-BDD compared to H-BDD. The reaction kinetics involved in initial ALD cycles are therefore influenced by this difference in surface moieties, as chemisorption of TMA and H_2O in ALD half cycle reactions is heavily dependent on the surface species, which changes from those solely on the substrate, to those on the substrate and deposited film, then finally to the species only on the deposited film, as deposition progresses in random deposition and island growth modes[9].

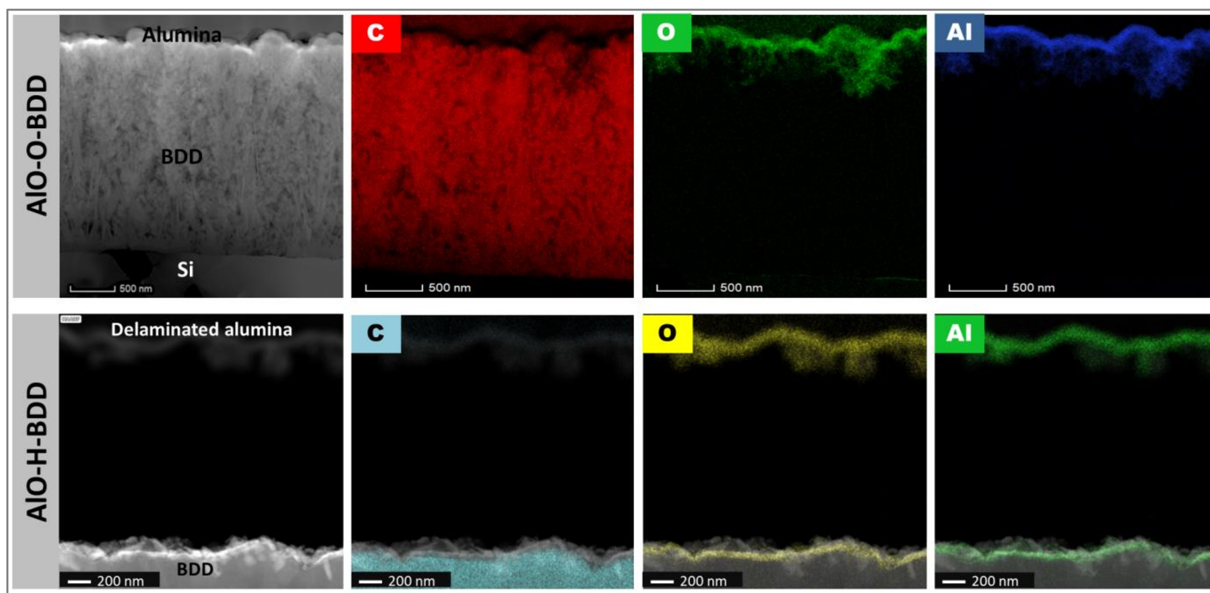

Figure 16: STEM-HAADF micrographs and corresponding EDX images are shown in for AlO-O-BDD in the top panel and AlO-H-BDD in the bottom panel; the first image is the STEM-HAADF image of the respective samples and subsequent images are those showing the areas of the sample where C, O and Al are present. The alumina film is adhered to the BDD film in AlO-O-BDD whereas the majority of the alumina film has delaminated from the BDD surface due to loss of cohesive strength.

A predominant H-terminated surface of other substrates has been shown to be relatively inert to reactions of TMA and H_2O[9,10,12]. Lower growth per cycle rates exhibited in the first few ALD cycles resulted in island growth of alumina thin films on H-terminated Si[9,12] and Ge[10]. This was explained by TMA favouring reactions with surface oxygen defect sites and dangling bonds rather than Si-H or Ge-H surface species[9,10,12]. Polycrystalline-associated and B defects, and few O ligands present on H-BDD, therefore accommodate the initial reaction with TMA during initial cycles. Further proliferation is then permitted by removal of the surrounding surface H, through reactions with CH_3 groups during ALD purging, thereby allowing sites for –OH ligands from the H_2O precursor for reaction with TMA in subsequent cycles. This resulting island growth is defined by film non-uniformity in the first few chemisorbed layers[10,12] and can therefore be the source of weakness demonstrated in AlO-H-BDD, leading to alumina film delamination due to loss of cohesive strength close to its interface with BDD. In contrast, O-terminated surfaces are shown to adsorb a greater quantity of TMA molecules, with Al bonding directly to surface O[9,10]. Increasing the quantity of O surface ligands by exposure to O_2 plasma

has the effect of adding mainly -OH and -O-C (ether) groups[35-37] which serve as favourable sites for TMA adsorption, resulting in uniform Al-O bonding at the interface. This would explain the better adhesive strength of the alumina film to BDD for AlO-O-BDD and its resistance to delamination.

4.0 Conclusions

The mechanical interfacial integrity of alumina films on as-grown and O_2 plasma treated polycrystalline BDD films has been investigated in this body of work. Exposure to the plasma was shown by XPS to functionalize the BDD surface by increasing the percentage ratio of C–OH and C-O-C ligands, compared to the as-grown BDD surface. Nanoindentation analysis demonstrated that for the range of loads applied, AlO-H-BDD experienced plastic deformation deeper into the BDD film while that for AlO-O-BDD was contained in the alumina film or near the alumina-BDD interface. The critical load for AlO-H-BDD was 100 mN, determined by the formation of circular buckles. AFM images of the indentation marks confirmed film delamination at a height of 1 μm due to applied load of 150 mN to AlO-H-BDD; film delamination was not observed for AlO-O-BDD. Delamination was not apparent for the load-displacement curves, which was theorized as possibly being due to its occurrence upon load application or removal, and as a result of incipient plasticity of the alumina or BDD film due to the behaviour of film defects or dislocations. TEM analysis suggested that stresses applied to AlO-H-BDD during sample preparation resulted in delamination of the alumina film close to its interface with BDD, because of a loss in cohesive strength. This occurs as island growth mode is adopted during initial ALD cycles due to the low percentage ratio of O moieties on the H-BDD surface, resulting in film non-uniformity close to the interface. The higher O concentration results in more active sites for TMA adsorption resulting in a uniformly bonded interface for AlO-O-BDD.

This study permits a better understanding of the mechanical stability of ALD alumina dielectric thin films on BDD semiconducting films, for use in microelectronics operating in mechanically stressful environments such as during spacecraft launch, deep well drilling and geothermal exploration. The technique of nanoindentation is shown to be advantageous for determining the interfacial integrity of these films and can therefore be utilized as a simple and fast test for mechanical stability especially where surface functionalization is necessary for electronic properties.

1 J. Y. Tsao, S. Chowdhury, M. A. Hollis, D. Jena, N. M. Johnson, K. A. Jones, R. J. Kaplar, S. Rajan, C. G. Van de Walle, E. Bellotti, C. L. Chua, R. Collazo, M. E. Coltrin, J. A. Cooper, K. R. Evans, S. Graham, T. A. Grotjohn, E. R. Heller, M. Higashiwaki, M. S. Islam, P. W. Juodawlkis, M. A. Khan, A. D. Koehler, J. H. Leach, U. K. Mishra, R. J. Nemanich, R. C. N. Pilawa-Podgurski, J. B. Shealy, Z. Sitar, M. J. Tadjer, A. F. Witulski, M. Wraback and J. A. Simmons, *Adv. Electron. Mater.*, 2018, **4**, 1–49.

2 N. Yang, S. Yu, J. V Macpherson and Y. Einaga, *Chem. Soc. Rev.*, 2019, **48**, 157–204.

3 P. W. May, M. N. R. Ashfold and Y. A. Mankelevich, *J. Appl. Phys.*, 2007, **101**, 053115.

4 M. Kasu, *Jpn. J. Appl. Phys.*, 2017, **56**, 01AA01.

5 H. Kawarada, H. Tsuboi, T. Naruo, T. Yamada, D. Xu, A. Daicho, T. Saito and A. Hiraiwa, *Appl. Phys. Lett.*, 2014, **105**, 013510.

6 J. W. Liu, M. Y. Liao, M. Imura and Y. Koide, *Appl. Phys. Lett.*, 2012, **101**, 1–5.

7 J. Robertson and R. M. Wallace, *Mater. Sci. Eng. R Reports*, 2015, **88**, 1–41.

8 S. D. Elliott and J. C. Greer, *J. Mater. Chem.*, 2004, **14**, 3246–3250.

9 R. L. Puurunen, *J. Appl. Phys.*, 2005, **97**, 121301-121301–52.

10 Y. Zheng, S. Hong, G. Psofogiannakis, G. B. Rayner, S. Datta, A. C. T. Van Duin and R. Engel-Herbert, *ACS Appl. Mater. Interfaces*, 2017, **9**, 15848–15856.

11 S. McDonnell, A. Pirkle, J. Kim, L. Colombo and R. M. Wallace, *J. Appl. Phys.*, 2012, **112**, 104110.

12 R. L. Puurunen, W. Vandervorst, W. F. A. Besling, O. Richard, H. Bender, T. Conard, C. Zhao, A. Delabie, M. Caymax, S. De Gendt, M. Heyns, M. M. Viitanen, M. De Ridder, H. H. Brongersma, Y. Tamminga, T. Dao, T. De Win, M. Verheijen, M. Kaiser and M. Tuominen, *J. Appl. Phys.*, 2004, **96**, 4878–4889.

13 G. Wan, M. Cattelan and N. A. Fox, *J. Phys. Chem. C*, 2019, **123**, 4168–4177.

14 T. T. Pham, M. Gutiérrez, C. Masante, N. Rouger, D. Eon, E. Gheeraert, D. Araùjo and J. Pernot, *Appl. Phys. Lett.*, 2018, **112**, 102103-1–4.

15 T. Jõgiaas, R. Zabels, A. Tamm, M. Merisalu, I. Hussainova, M. Heikkilä, H. Mändar, K. Kukli, M. Ritala and M. Leskelä, *Surf. Coatings Technol.*, 2015, **282**, 36–42.

16 A. Kleinbichler, M. J. Pfeifenberger, J. Zechner, N. R. Moody, D. F. Bahr and M. J. Cordill, *Jom*, 2017, **69**, 2237–2245.

17 K. L. Mittal, *Electrocompon. Sci. Technol.*, 1976, **3**, 21–42.

18 J. Chen and S. Bull, *J. Phys. D. Appl. Phys.,* 2011, **44**, 034001.

19 V. Cech, T. Lasota, E. Palesch and J. Lukes, *Surf. Coatings Technol.*, 2015, **261**, 114–121.

20 E. Gheeraert, P. Gonon and A. Deneuville, *Diam. Relat. Mater.*, 1993, **2**, 742–745.

21 V. Mortet, L. Kavan, A. Taylor, Z. Vl, D. Machon, O. Frank, P. Hubík and D. Tremouilles, *Diam. Relat. Mater.*, 2018, **88**, 163–166.

22 A. C. Ferrari and J. Robertson, *Philos. Trans. A. Math. Phys. Eng. Sci.*, 2004, **362**, 2477–2512.

23 P. W. May, W. J. Ludlow, M. Hannaway, P. J. Heard, J. A. Smith and K. N. Rosser, *Diam. Relat. Mater.*, 2008, **17**, 105–117.

24 A. C. Ferrari and J. Robertson, *Phys. Rev. B*, 2000, **61**, 95–107.

25 J. R. Oliveira, O. M. Berengue, J. Moro, N. G. Ferreira, A. J. Chiquito and M. R. Baldan, *Appl. Surf. Sci.*, 2014, **311**, 5–8.

26 M. Wang, N. Simon, C. Decorse-Pascanut, M. Bouttemy, A. Etcheberry, M. Li, R. Boukherroub and S. Szunerits, *Electrochim. Acta*, 2009, **54**, 5818–5824.

27 J. V Macpherson, *Phys. Chem. Chem. Phys.*, 2015, **17**, 2935–49.

28 J. G. Buijnsters, M. Tsigkourakos, T. Hantschel, F. O. V. Gomes, T. Nuytten, P. Favia, H. Bender, K. Arstila, J.-P. Celis and W. Vandervorst, *ACS Appl. Mater. Interfaces*, 2016, **8**, 26381–26391.

29 J. I. B. Wilson, J. S. Walton and G. Beamson, *J. Electron Spectros. Relat. Phenomena*, 2001, **121**, 183–201.

30 F. N. Li, R. Akhvlediani, M. K. Kuntumalla, A. Hoffman and A. Ho, *Appl. Surf. Sci.*, 2019, **465**, 313–319.

31 S. A. Barve, S. S. Chopade, R. Kar, N. Chand, M. N. Deo, A. Biswas, N. N. Patel, G. M. Rao, D. S. Patil and S. Sinha, *Diam. Relat. Mater.*, 2017, **71**, 63–72.

32 M. G. Donato, G. Faggio, G. Messina, S. Santangelo, M. Marinelli, E. Milani, G. Pucella and G. Verona-Rinati, *Diam. Relat. Mater.*, 2004, **13**, 923–928.

33 K. S. Pal, A. K. Mallik, N. Dandapat, N. R. Ray, S. Datta, S. Bysakh and B. K. Guha, *Bull. Mater. Sci.*, 2015, **38**, 537–549.

34 P. Strobel, J. Ristein and L. Ley, *Diam. Relat. Mater.*, 2008, **17**, 1362–1366.

35 M. A. Neto, G. Pato, N. Bundaleski, O. M. N. D. Teodoro, A. J. S. Fernandes, F. J. Oliveira and R. F. Silva, *Diam. Relat. Mater.*, 2016, **64**, 89–96.

36 R. E. Thomas, R. A. Rudder and R. J. Markunas, *J. Vac. Sci. Technol. A Vacuum, Surfaces, Film.*, 1992, **10**, 2451.

37 L. Ostrovskaya, V. Perevertailo, V. Ralchenko, A. Dementjev and O. Loginova, *Diam. Relat. Mater.*, 2002, **11**, 845–850.

38 M. Broas, O. Kanninen, V. Vuorinen, M. Tilli and M. Paulasto-Kröckel, *ACS Omega*, 2017, **2**, 3390–3398.

39 V. V. Afanas'ev, A. Stesmans, B. J. Mrstik and C. Zhao, *Appl. Phys. Lett.*, 2002, **81**, 1678–1680.

40 J. M. Reyes, M. P. Ramos, C. Zu, W. C. Arriaga, P. R. Quintero and A. T. Jacome, *J. Electrochem. Soc.*, 2013, **160**, 201–206.

41 J. T. Gaskins, P. E. Hopkins, D. R. Merrill, S. R. Bauers, E. Hadland, D. C. Johnson, D. Koh, J. H. Yum, S. Banerjee, B. J. Nordell, M. M. Paquette, A. N. Caruso, W. A. Lanford, P. Henry, L. Ross, H. Li, L. Li, M. French, A. M. Rudolph and S. W. King, *ECS J. Solid State Sci. Technol.*, 2017, **6**, N189–N208.

42 A. A. Dameron, D. Seghete, B. . Burton, S. D. Davidson, A. S. Cavanagh, J. . Bertrand and S. M. George, *Chem. Mater.*, 2008, **20**, 3315–3326.

43 R. Katamreddy, R. Inman, G. Jursich and A. Soulet, *J. Electrochem. Soc.*, 2007, **10**, C701–C706.

44 A. C. Dillon, A. W. Ott, J. D. Way and S. M. George, *Surf. Sci.*, 1995, **322**, 230–242.

45 G. Socrates, *Infrared and Raman characteristic group frequencies*, John Wiley & Sons, Ltd, West Sussex, 3rd edn., 2004.

46 M. Bhattacharya and A. K. Mukhopadhyay, *ISRN Ceram.*, 2012, **2012**, 1–9.

47 W. G. Mao, Y. G. Shen and C. Lu, *Scr. Mater.*, 2011, **65**, 127–130.

48 A. Fischer-Cripps, *Surf. Coatings Technol.*, 2006, **200**, 4153–4165.

49 X. Wang, X. Shen, J. Gao and F. Sun, *Carbon N. Y.*, 2017, **117**, 126–136.

50 X. Liu, Y. Y. Chang, S. N. Tkachev, C. R. Bina and S. D. Jacobsen, *Sci. Rep.*, 2017, **7**, 1–7.

51 P. Wurzinger, P. Pongratz, J. Gerber and H. Ehrhardt, *Diam. Relat. Mater.*, 1996, **5**, 345–349.

52 X. Jiang, K. Schiffmann and C. P. Klages, *Phys. Rev. B*, 1994, **50**, 8402–8410.

53 Y. Tzou, J. Bruley, F. Ernst, M. Ruhle and R. Raj, *J. Mater. Res.*, 1994, **9**, 1566–1572.

54 M. R. Maughan and D. F. Bahr, *Mater. Res. Lett.*, 2014, **3**, 58–64.

55 I. Salehinia, S. K. Lawrence and D. F. Bahr, *Acta Mater.*, 2013, **61**, 1421–1431.

56 A. M. Minor, S. A. S. Asif, Z. Shan, E. A. Stach, E. Cyrankowski, T. J. Wyrobek and O. L. Warren, *Nat. Mater*, 2006, **5**, 697–702.

Chapter 3: Fabrication of Tantalum Oxide Films by ALD Using PDMAT and H_2O

1.0 Introduction

ALD of films with high-κ have been studied for use in (sub)microelectronic devices, which include, MOS capacitors and field effect transistors[1–3], as well as for resistive switching random access memory (RAM) devices[4,5]. High-κ layers in these applications adopt the role of passivating surface charges and/or concentrating charge carriers in the semiconducting bulk thus preventing the leakage of charge carriers across the dielectric. In addition, a high κ value is theoretically advantageous for offsetting the size constraints of small MOS devices, this is because as devices get smaller, the area of the oxide decreases thereby decreasing its capacitive ability but use of materials with high κ values acts to increase the capacitance (equation (1)) or concentration of charges thus preventing the electric breakdown of the oxide and minimizing current leakage across the semiconductor-dielectric interface[6].

ALD as a film deposition technique is advantageous for fabricating thin (<10 nm), conformal films, utilizing relatively low temperatures and separation of precursors during cyclic reactions, and is therefore utilized for (sub)microelectronic layers. To achieve ideal ALD film deposition, strides are made towards the realization of self-limiting and saturating reactions via exploration of a variety of precursors chemistries, deposition temperatures, exposure and purging durations, as well as the use of plasmas and manipulation of cycle definitions. These efforts are necessary and cajoled by factors such as system limitations, surface terminations, high aspect ratio substrates and desired film thickness.

Ta_2O_5 films engineered by ALD have employed a variety of Ta precursors such as, Ta halides (TaI_5, $TaCl_5$), Ta ethoxide ($Ta_2(OC_2H_5)_{10}$) and pentakisdimethylamido Ta ($Ta(N(CH_3)_2)_5$, PDMAT), used together with O precursors, H_2O, ozone and O_2[7-10]. Alkylamide precursors, such as PDMAT, have been studied for their reaction mechanisms with O precursors as well as various surfaces such as Si and GaAs[11-13]. At low temperatures dissociation of this family of precursors typically occurs through metal-ligand scission, due to its lower energy barrier compared to that of N-C[13]. Alkylamides have also been associated with the etching of native surface oxides through the dimethylamine ligand thereby resulting in the creation of abrupt interfaces[12,14]. PDMAT comprises one Ta atom bonded to 5 N atoms each of which are then bonded to 2 methyl (CH_3) groups. Endothermic peaks for PDMAT heated in an N_2 environment at atmospheric pressure, 760 Torr, were shown to occur at 160 ^oC, while that heated at 0.6 Torr occurred at 80 ^oC[15]. Melting of the precursor was determined to start from temperatures as low as 50 ^oC, while the temperature of evaporation was 184 ^oC at 760 Torr and 106 ^oC at 0.6 Torr[15]. Furthermore, it was suggested that both melting and evaporation occurred at these evaporation temperatures, with the rate of evaporation exceeding that of melting[15]. Thermal studies of PDMAT also revealed that from 60 ^oC the principal molecule present, displaying the highest partial pressure, was

$TaN_4C_8H_{24}$; decomposition of this molecule occurred around 212 °C[16]. The PDMAT molecule, $TaN_5C_{10}H_{30}$, exerted the second highest pressure but was shown to start decomposing around 70 °C[16], close to that recorded at 80 °C for the endothermic peak at 0.6 Torr[15]. Decomposition of PDMAT around 212 °C, and continuing at temperatures up to 400 °C, gave rise to a variety of other molecules, predominantly, HNC_2H_6 and H_2O, the latter from impurities in the precursor, as well as smaller dimethylamido Ta molecules[16].

In the few studies which have explored the ALD saturation parameters for PDMAT and H_2O, the ALD window was determined to lie between 200-250 °C[11]. In this range, reference is made to the decomposition of the PDMAT precursor around 212 °C, as discussed above, as well as the presence of various smaller Ta molecules, although the highest vapour pressure is shown to be due to HNC_2H_6[16]. Reported values of the resulting ALD GPC in this temperature range varied between 0.85 Å/cycle and 0.65 Å/cycle[9,11]. More recent research revealed even lower GPCs, approximately 0.5 Å/cycle for temperatures up to 300 °C[1,17]. It should also be noted that the PDMAT precursor is heated to various temperatures across publications, ranging from 65-120 °C[9,11,12,17,18], a parameter likely to affect the resulting GPC, especially when it exists as solid particles, as is the case for PDMAT. Precursors are generally required to be volatile and thermally stable, so that even solid precursors should pose no problem once their dose is sufficiently large so as to saturate the surface of the sample[19]. The challenge therefore arises in knowing the temperature, or range thereof, that permits a sufficiently large dose without causing precursor decomposition.

The utilization of Ta_2O_5 as a dielectric film signifies the importance of its dielectric constant, κ. Factors which have been shown to influence this value are film thickness, crystallinity, and density, which may be related to ALD conditions such as deposition temperature[2,20]. In general, reported κ values for Ta_2O_5 films, fabricated by ALD, range from 18-28[2,9,17,20]. As-deposited films were shown to be amorphous, exhibiting crystallinity upon annealing at temperatures from about 700 °C[2,20]. Ta_2O_5 films have also been fabricated in multilayers or nanolaminates with other dielectric oxides such as, Al_2O_3, HfO_2 and ZrO_2, to permit the achievement of tailored properties including, mechanical, morphological and κ value, typically arriving at a compromise between those of the individual oxide films[2,17,21-23]. Ta_2O_5 bilayers with Al_2O_3, for example, displayed κ values between those of pure Ta_2O_5 and Al_2O_3, and realized an increase in κ after annealing at 800 and 900 °C[2].

Specific to diamond MOS devices such as diodes or transistors, Ta_2O_5 has rarely been utilized, and in the few publications that have explored its capabilities, films have been fabricated by sputter deposition onto SCD surfaces[3,24,25]. The resulting MIS diodes were shown to display leakage currents of 10^{-8} A/cm^2 for as deposited Ta_2O_5 and 10^{-2} A/cm^2 for crystallized Ta_2O_5 obtained via annealing at 800 °C, although the crystalized film presented a higher κ of 29 and a higher capacitance, C, of 15.3 pF[25]. It was explained that the under-performance of as-deposited Ta_2O_5 in terms of κ and C was due to the presence of bulk defects in film in the form of excess O, rather than the presence of interface defects with SCD[25]. Ta_2O_5 films have also been investigated in concert with Al_2O_3 buffer layers on the SCD surface, which resulted in an overall lower κ of 12.7, when the both oxides are taken into consideration[3]. Despite this value, a low interfacial charge trap density was confirmed, together with a leakage current of 10^{-11} A[3].

This report presents the fabrication of tantalum oxide (TaO) films by ALD using PDMAT and H_2O. By employing various ALD parameters for each film, deposition behaviour is anaylzed with

respect to deposition temperature and H_2O exposure, and film properties are investigated by XRD and AFM to explain deviations is expected behaviour. In addition, discussion, pertaining to the challenges associated with ALD of TaO films, specifically those with the PDMAT precursor which exists as solid particles, is provided. Overall, therefore, the aim of this work is to understand the TaO film growth by ALD and under the chosen parameters as this will permit their optimal use as high-κ dielectrics for diamond MOS devices. It is apparent that while fabrication of TaO films by ALD has been reported in literature, the results presented here and the challenges faced in obtaining them, underscore differences in growth behaviours, demonstrating incongruities in attempts at reproduction. This study is thus necessitated to highlight these inconsistencies and expand the general understanding for ALD TaO films.

2.0 Experimental Procedure

2.1. TaO Film Fabrication by ALD

TaO films were deposited by ALD on p-type Si (100) substrates. The substrates were pre-treated with piranha solution that is, H_2SO_4 and H_2O_2 in the ratio 3:1, for 30 minutes. Pentakis(dimethylamido) tantalum (PDMAT) was used as the Ta source while H_2O was used as the O source. An ALD cycle was described by the duration of open valve (Ta)–purge (N_2)–open valve (O)–purge (N_2), thus deposition parameters were 0.2 s–20 s–0.3 s–30 s. Prior and subsequent to deposition the chamber was purged with 100 sccm N_2 gas; during deposition N_2 was utilized as both carrier and purging gas and set at 50 sccm. To determine the influence of chamber temperature, depositions were performed at 250, 260, 270 and 280 ^{o}C. In addition, saturation was investigated by varying the duration of H_2O exposure: 0.1, 0.3, 0.4, 0.5 s, at a deposition temperature of 270 ^{o}C. The PDMAT cannister was set between 120-130 ^{o}C and that for H_2O was maintained at room temperature with the valve heated to 100 ^{o}C.

2.2. TaO Film Characterization

TaO films were characterized by X-ray fluorescence (XRF) and X-ray reflectivity (XRR), both carried out at the Department of Solid-State Sciences, COCOON, Ghent University, Ghent, Belgium. XRF was performed using a Bruker Artax system with a Mo X-ray source, incident at an angle of 5 ^{o}, and a silicon drift detector, positioned perpendicular to the sample. XRR was performed in a Bruker D8 system, equipped with a Cu Kα source and a point detector, and was used to determine correlation to the XRF technique. Ta loading for XRF is measured via the Lα line at 8.14 keV, the peak counts are summed for both Ta and Si signals to achieve normalized intensities (Ta/Si).

GIXRD analysis was performed to determine the crystallinity of the as-deposited films. Measurements were made on a Philips X'Pert MRD X-ray diffractometer with a Cu anode and were recorded for 2θ angles between 15 and 70°, a scan step of 0.2 ° and an angle of incidence of 0.5 ^{o}.

The surface topography of the TaO films was imaged by AFM using a Ntegra Prima setup (NT-MDT) in tapping mode, under ambient conditions. A Si cantilever (Nanosensor PPP-NCHR) with a spring constant of $k \approx 42\ N \cdot m^{-1}$ and tip radius <10 nm was used. Surface roughness was determined as root-mean-square value (R_q).

SEM was performed using a Hitachi S4100 system with accelerating voltages 15-25 kV, to determine the presence of TaO films on the diamond film surfaces.

3.0 Results and Discussion

XRF spectra were obtained for TaO films deposited at temperatures from 250-280 ^{o}C, shown in Figure 17(a). The peak at 8.2 eV is due to the Lα spectral line of Ta, at which the resulting spectra have been normalized. Taking the Ta/Si ratio of intensities of the spectrum for each deposition temperature, normalized for 100 cycles, the graph (blue) of Figure 17(b) is obtained. The intensity is shown to be a minimum at an ALD temperature of 270 ^{o}C, while higher Ta loading is measured for 260 and 280 ^{o}C. Also shown is the graph (green) of the ALD GPC variation with deposition temperature, obtained by XRR, which follows closely to the XRF intensities. This result validates the reliability of the techniques for measuring Ta loading and film proliferation. The lowest GPC, of 0.13 nm/cycle, was measured at 270 ^{o}C, while a GPC of 0.24 nm/cycle was measured for films deposited at 280 ^{o}C.

The occurrence of saturation was subsequently investigated for depositions at 270 ^{o}C, the temperature at which the minimum GPC and Ta loading were obtained. This lies in a higher ALD temperature window than that reported in literature for PDMAT Ta_2O_5 films, 200-250 ^{o}C; the range for which constant but minimum GPCs were realized[11]. It is worth noticing in Figure 17(b) that the GPC at 250 and 260 ^{o}C is approximately constant at 0.20 nm/cycle and therefore likely characterizes a narrow ALD window for the tested range. It is also interesting that the graph of Figure 17(b) resembles that for ALD of TiO_2 films by TDMAT, the same chemical family of precursor as that used for Ta, and H_2O, in which GPC values across temperature ranges from 120 to 350 ^{o}C decreases until a minimum followed by an increase, so that no constant GPC ALD window is defined[26,27]. This occurrence is explained by a change in the number of active surface sites with temperature making it possible to achieve saturation of these fewer or greater number of temperature dependent sites and realize lower or higher GPCs, respectively[26,28]. Nevertheless, films were deposited at 270 ^{o}C for H_2O valve opening durations (referred to as 'exposure') of 0.1, 0.3 and 0.4 s, while that for PDMAT remained at 0.2 s, the minimum Ta exposure at which a film was realized. This comparison between TiO and TaO films are made here as there are fewer reports which detail the ALD growth behaviour of TaO films using PDMAT and H_2O.

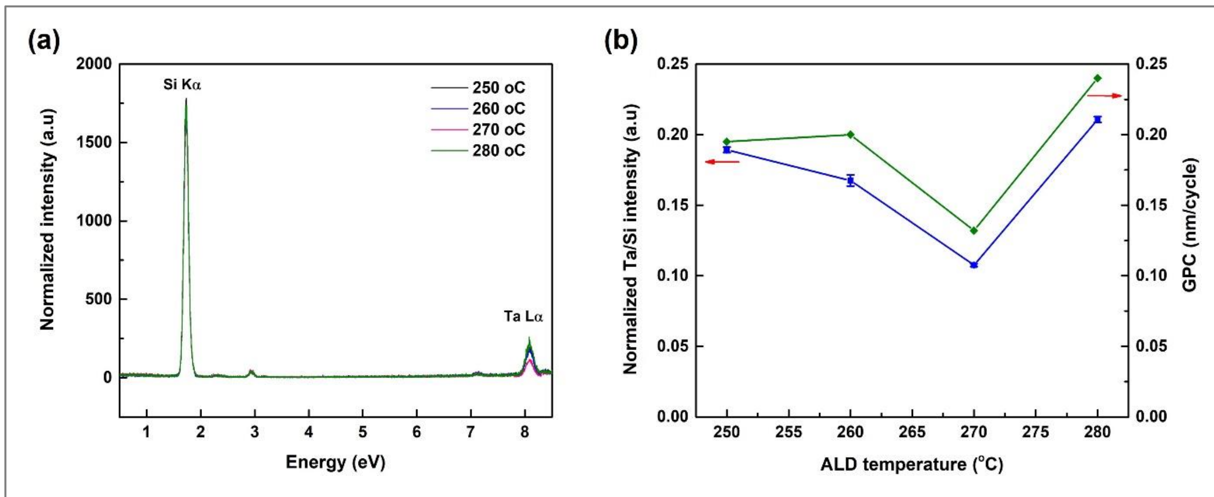

Figure 17: (a) XRF spectra for films deposited at ALD temperatures, 250, 260, 270, 280 °C, showing Si Kα and Ta Lα intensities, normalized for 100 cycles; (b) graph of Ta/Si intensity variation with deposition temperature (blue graph), and film growth per cycle (GPC) variation with deposition temperature (green graph) obtained by XRR measurements.

XRF spectra for films deposited at various H_2O exposures are shown in Figure 18(a), and the corresponding graphs of Ta/Si intensities versus H_2O exposure, in Figure 18(b) (blue). Films with H_2O exposure of 0.3 s exhibited the lowest Ta loading and GPC while those deposited at exposures of 0.1 and 0.4 s demonstrated higher Ta loading, reiterated in their GPC value of 0.22 nm/cycle obtained by XRR. The general trend of the graphs together with the GPC range from 0.13-0.22 nm/cycle, highlight a varied GPC for the tested range of exposures. Reasons for this are discussed further in this section.

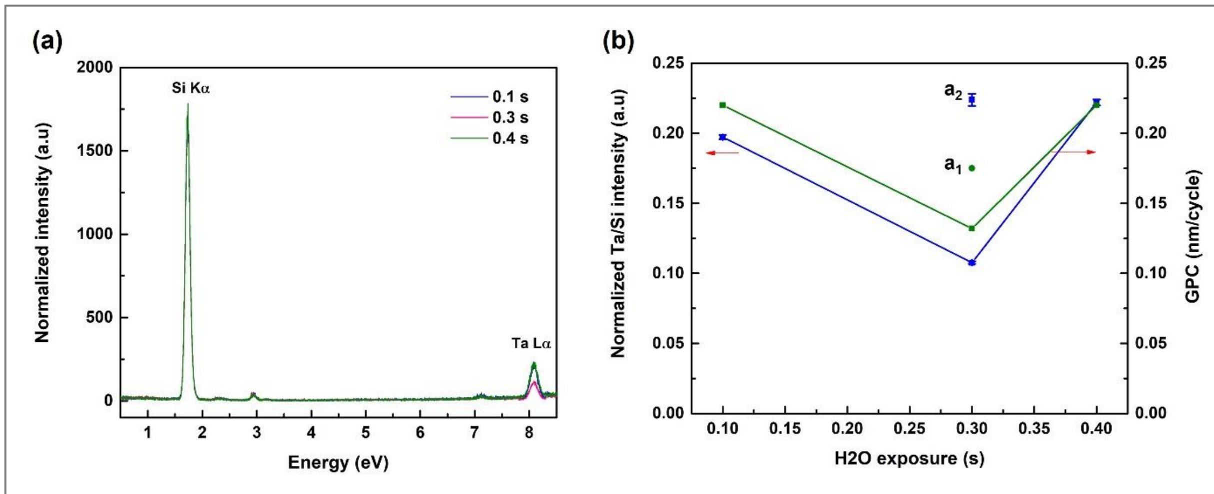

Figure 18: Graphs for identifying saturation parameters at ALD temperature of 270 °C; (a) XRF spectra showing peak intensities for Si Kα and Ta Lα, normalized for 100 cycles, for films deposited at exposures 0.1, 0.3, 0.4 s; (b) graph showing variation of Ta/Si intensity with H_2O exposure (blue) from XRF spectra in (a), and variation of GPC with H_2O exposure (green) from XRR analysis; points a_1 and a_2 are the respective GPC and Ta/Si intensity for TaO films deposited at 0.3 s exposure until a thickness of 3.5 nm.

In general, the films analysed possessed thicknesses from 20-44 nm, resulting from 100-250 ALD cycles, but plotted data was normalized for 100 cycles, in the case of XRF intensities, and for 1 cycle to attain GPC. The high correlation between XRR and XRF data for intensities not normalized for the number of ALD cycles, represented in Figure 19, ascertains reliability of the techniques, with thinner films displaying lower Ta/Si loading and thicker films having higher loading. The trendline of Figure 19 defines ideal correlation with an intercept at (0,0), and therefore shows some discrepancy between film thickness and Ta/Si intensity, possibly explained by differences in film density. In other words, thicker films realizing lower Ta loading than expected may be less dense, while thinner films with higher Ta loading may be more dense.

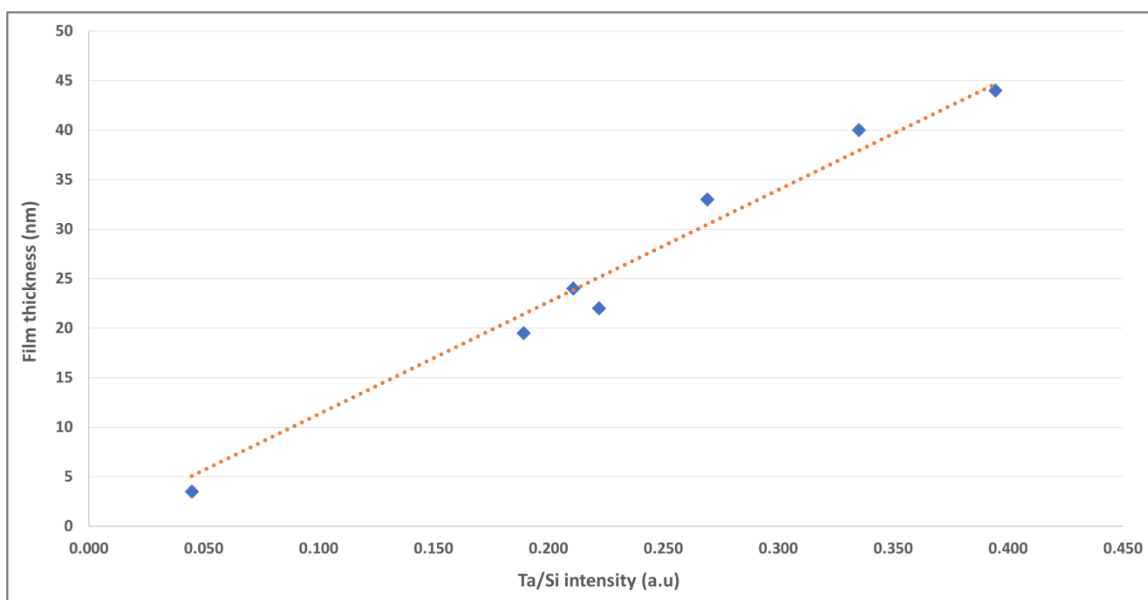

Figure 19: Graph showing correlation between XRR and XRF techniques for measurement reliability of ALD TaO films; while there is a high correlation between film thickness and Ta/Si intensity, discrepancies exist which can be explained by differences in film density

XRF and XRR measurements were thus repeated at 0.3 s H_2O exposure for fewer cycles, that is, thinner films of 3.5 nm. It is identified in Figure 18(b) as point a_1 for GPC, and a_2 for the corresponding Ta/Si intensity. It was found that a_1 yielded a higher GPC, 0.18 nm/cycle, than its thicker (33 nm) counterpart with 0.13 nm/cycle, and a_2 revealed higher Ta loading when normalized for 100 cycles. This difference in GPC with film thickness for the 0.3 s exposure can be explained by differences in film proliferation during initial cycles where reactions are more influenced by the substrate surface, compared to reactions occurring only on the film surface after a sufficient number of cycles has elapsed. The GPC of the 3.5 nm film is higher during initial cycles due to the high number of active sites, those permitting precursor reactions, on the piranha-treated Si surface, however, as the film proliferates the number of surface sites may decrease so that the lower GPC of the 33 nm film may therefore be the result of fewer active sites on the TaO surface. Differences in GPC over the number of cycles are reiterated in the graphs of Figure 20. The additional point for 100 cycles, 14 nm, highlights a decrease

in GPC over the number of cycles, in Figure 20(a), while Figure 20(b) shows that there is an approximately linear dependence of film thickness on the number of ALD cycles. Non-linear growth during the first few cycles, or nucleation stage of ALD, has been discussed in literature for TiO_2 films, citing differences in active surface sites and changes in the resulting surface energies as reasons for the occurrence[29,30]. Further, it was mathematically shown that the maximum film thickness realized in one ALD cycle was determined by the number of these available sites on the film surface, which are limited by steric hindrances due to the volumetric size of the precursors[31]. It is therefore understood that over time as the film grows, occurrences of steric hindrance can decrease the number of available sites and thus the GPC.

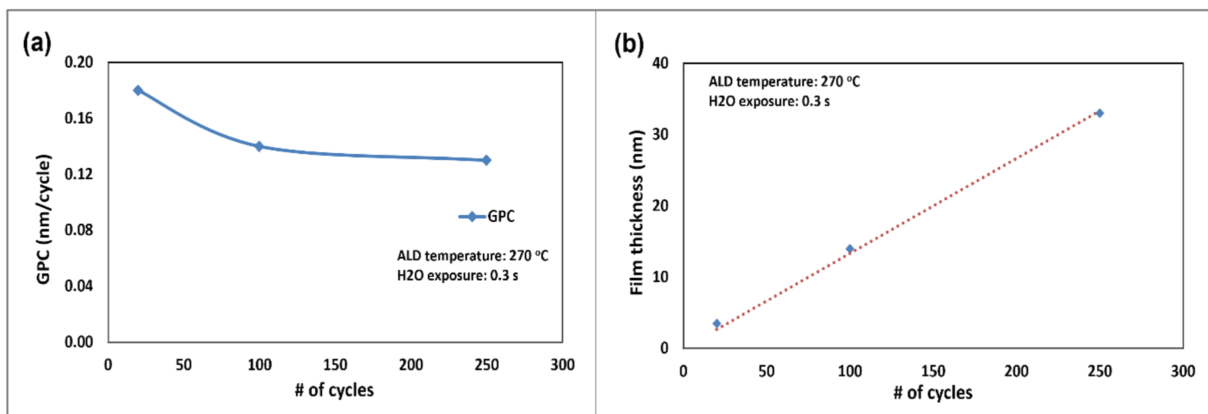

Figure 20: (a) GPC and (b) film thickness variation with number of ALD cycles, obtained by XRR, for TaO films deposited at 270 °C with H_2O exposure of 0.3 s and PDMAT exposure of 0.2 s.

Considering these results, both normalized Ta/Si intensities and GPC values are shown to be sensitive to the film thickness, that is, whether this thickness resulted from ALD conditions at which a constant GPC has already been attained; otherwise, comparisons are made among samples with over or underestimated GPCs and intensities. Analysis of samples already displaying the constant GPC therefore provides a more accurate trend for ALD window and saturation studies, departure from which may be a contributor for discrepancies related to this work as threshold values have not been studied, although we expect that 20-44 nm films may not present overly large variations across parameters. Specifically for the measurements presented here, however, failure to achieve clearly identified saturating conditions is perhaps more influenced by the chosen parameters and challenges with the PDMAT precursor rather than film thicknesses.

Analysis of ALD saturation conditions was carried out for films deposited at 270 °C, a temperature which does not seem to lie in the ALD window, and at which PDMAT may be subjected to decomposition. The temperature dependent graph of Figure 17(b) reveals an almost constant GPC for films grown at 250 and 260 °C, and a lower GPC for those at 270 °C, which suggests that the ALD window possibly occurs between 250-260 °C, for the explored temperature range; the reported ALD window for Ta_2O_5 films using PDMAT and H_2O is 200-250 °C[11]. Caution is exercised here in defining the ALD window without an understanding of GPC values for films grown here at even lower temperatures, <250 °C. In addition, the theory that TaO growth may occur in the same way as that of

TiO films whereby surface saturation is achieved although GPC decreases with increasing temperature, because of the fewer number of active surface sites available at higher temperatures[26,28], is invalidated here since saturation was not observed at 270 ^oC in the graph of Figure 18(b). Non-ideal reaction behaviour which lies out of the ALD window, taken to be between 250-260 ^oC, is therefore attributed to desorption or loss of surface species, and/or precursor decomposition[10,32]. In cracking studies of PDMAT performed in an ultra-high vacuum Ar environment, the highest partial pressure was found to be exerted by $TaN_4C_8H_{24}$ molecules while the second highest was exerted by $TaN_5C_{10}H_{30}$, that is, the PDMAT molecule[16]. The latter demonstrated a steady decrease in partial pressure from 70 ^oC, due to thermal cracking processes, while decomposition of the former began around 212 ^oC and continued rapidly until 400 ^oC[16]. This precursor decomposition, and thus appearance of new and varied molecules, occurring in the range tested for our TaO films, 250-280 ^oC, could explain the lower, and subsequent higher, GPC for depositions at 270 and 280 ^oC, respectively. The lower GPC at 270 ^oC could be the result of a greater influence of the PDMAT partial pressure decrease which leads to unreacted surface sites, while the increase in GPC at 280 ^oC would then be due to the greater influence of PDMAT decomposition, giving rise to new molecules such as, $TaN_3C_6H_{18}$ and $TaN_2C_4H_{14}$[16], which would change surface energies.

To better understand the effect of H_2O exposure on film growth, and thus the behaviour of the saturation graphs, samples were characterized using GIXRD (Figure 21). Film properties for H_2O exposures, 0.1-0.5 s, are exhibited in Figure 21(a) and are shown to be primarily amorphous. It should also be noted that peak contributions may be masked because of the film thickness, nevertheless, films grown at 0.3 s exhibited a small peak at 27 ^{o} while those at 0.5 s show some structural ordering near 26 and 55 ^{o}. The result for the 0.3 s exposure was confirmed by analysis of thicker films grown under the same conditions, demonstrating a sharper peak of higher intensity also near 27 ^{o} (Figure 21(b)), together with other smaller peaks at 32, 55 and 56 ^{o}, all due to diffractions from Ta_2O_5 phases; the strong signal at 54 ^{o} is attributed to the Si (311) signal caused by the orientation of the sample when measured. It is therefore concluded that an increase in H_2O exposure from 0.1 to 0.3 s has the effect of introducing crystallinity into the films. This result was also observed for ALD Ta_2O_5 films grown from $TaCl_5$ and H_2O, where the XRD signal intensity increased with an increase in H_2O exposure[33]. It was also explained that the longer exposure time facilitated surface migration of the molecules, forming larger islands and promoting two-dimensional growth, thereby improving film crystallinity[33]. An increase in the crystalline phase, however, accompanied a higher GPC[33], which is contrary to the results in this work where the more crystalline film from the 0.3 s exposure exhibited the lowest GPC.

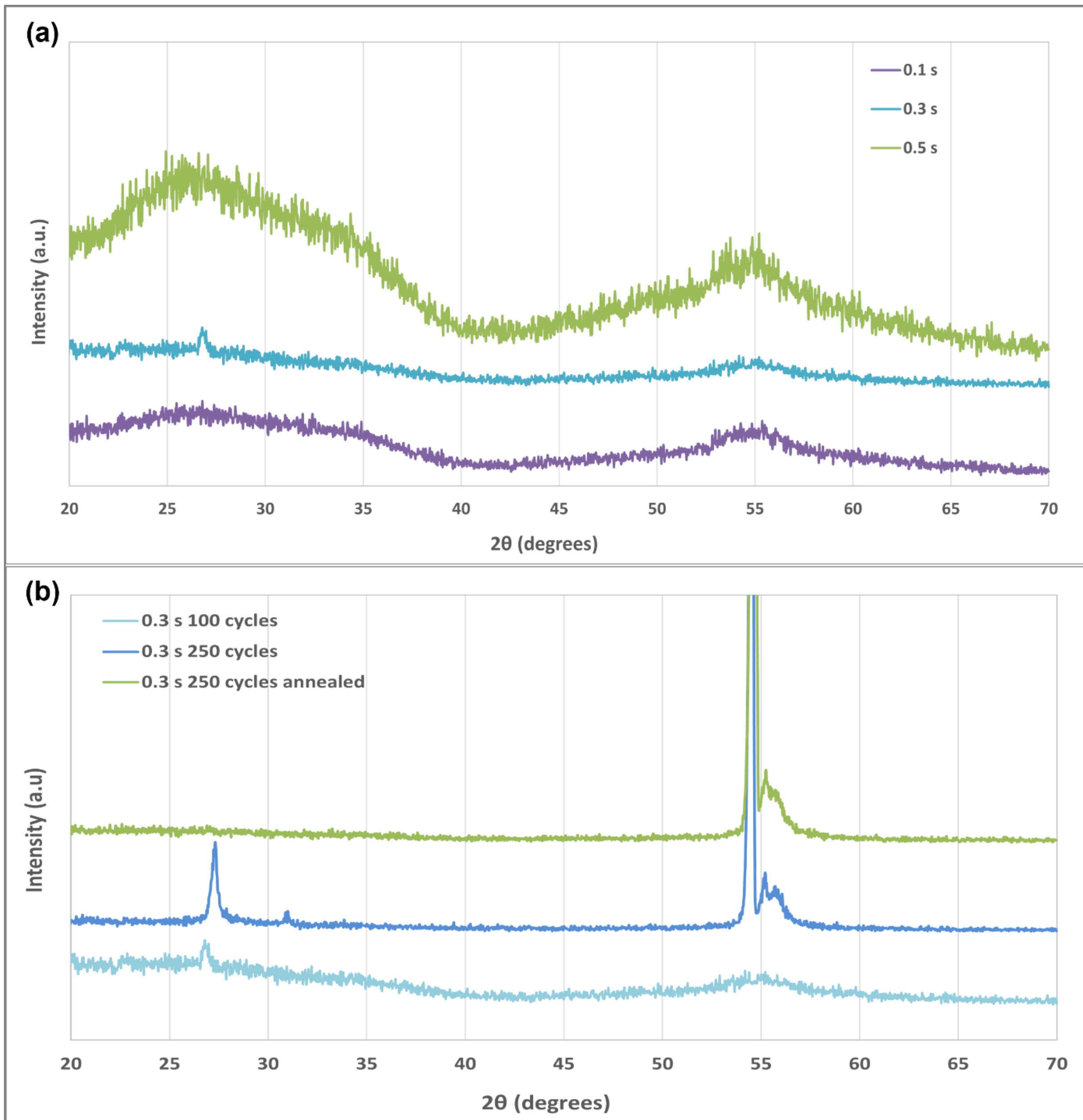

Figure 21: XRD diffractograms of films deposited at (a) 0.1-0.5 s H_2O exposures, and (b) 0.3 s H_2O exposures for 100 and 250 cycles, with the diffractogram also shown for the latter annealed at 600 ^oC in a N_2 atmosphere. The film at 0.1 s exposure is amorphous while that at 0.3 s begins to show δ-Ta_2O_5 crystal phase, confirmed by the thicker film at 0.3 s, and with a preferred orientation upon annealing.

Films grown at 0.3 s for 250 cycles were further annealed at 600 ^oC in a N_2 environment, to characterize the Ta_2O_5 phase present at the onset of crystallinity. Its diffractogram revealed ordering of the crystal phase towards a preferred orientation, evidenced by the disappearance of the peaks at 27 and 32°, characteristic of the as-deposited film, and a merging of the peaks at 55 and 56 ^{o}, although overlapped by the Si signal. It is not expected that annealing at 600 ^oC will form completely crystalline

films, as reports in literature have generally identified temperatures above 600 ºC, as low as 660 ºC[34] and more likely at 700 ºC[34-36], for the crystallization of Ta_2O_5 films. The effect of annealing at 600 ºC therefore acts to start the formation of an ordered structure over a longer range, hence the presence of only one peak. Two Ta_2O_5 phases are typically discussed in literature, hexagonal δ-Ta_2O_5 and orthorhombic β-Ta_2O_5, as they both exhibit diffraction patterns with similarly positioned intense peaks. It is therefore difficult to differentiate these phases only by their peaks and, as there are few intense peaks in the diffractograms of Figure 21, their identification is further complicated. β-Ta_2O_5 has however, typically been associated with crystallinity resulting from annealing over 700 ºC, while δ-Ta_2O_5 is indexed for lower temperatures[33-36]. It is thought that δ-Ta_2O_5 occurs as a metastable intermediate phase, forming preferably at relatively low temperatures where crystal growth is just initiated, but may also be due to film impurity incorporation and departure from stoichiometric films[33]. The crystal phase identified in this work is therefore suggested to be that of δ-Ta_2O_5, based on these arguments.

Analysis of the 0.3 s sample was performed by AFM (Figure 22), establishing a low surface roughness of 0.28 nm.

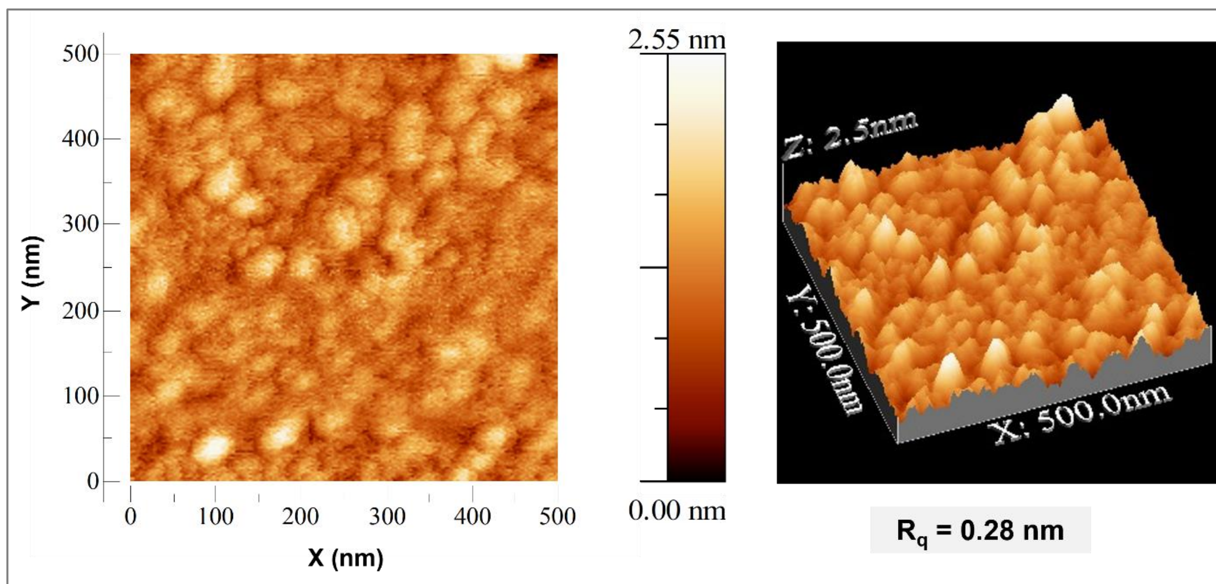

Figure 22: Surface topography of 0.3 s TaO films at 270 ºC, obtained by AFM.

Complementary to the discussion provided, is the challenge contributed by the PDMAT precursor, specifically the inconsistency in its exposure. It was noticed during depositions, occasions for which a chosen set of parameters, initially resulting in the deposition of a film, failed to achieve this outcome when repeated. Further investigation revealed alleviation of this occurrence by increasing the temperature of the PDMAT cannister, thus PDMAT of a newly filled cannister was heated to 120 ºC but to maintain film deposition after a few experiments, heating needed to be increased between 130-140 ºC. When film depositions could no longer be achieved and the cannister opened, the contents, initially

orange-coloured particles, was instead comprised of few, smaller black particles. Studies in literature have reported on the thermal behaviour of PDMAT when heated at atmospheric pressure, 760 Torr, and at 0.6 Torr[15]. Endothermic peaks were obtained at 160 and 80 ^oC for 760 and 0.6 Torr, respectively, with simultaneous melting and evaporation occurring, for the respective pressures, at 184 and 106 ^oC[15]. In addition, a study of the thermal behaviour of PDMAT after being heated at 150 ^oC for 6 h, showed that the temperature of evaporation increased to 216 ^oC at 760 Torr, suggested as being due to a change in the molecular structure upon initial heating[15]. In terms of the challenges faced in this work with PDMAT these reported values provide an explanation for our observations.

Firstly, the heating temperature of 120 ^oC is justified for the pressure inside the precursor cannister as, while it was not measured, it may lie between 80 and 760, resulting from the PDMAT vapour pressure from heating as well as that supplied by the N_2 gas used as the carrier for the precursor. Heating of PDMAT to 120 ^oC was said to produce a vapour pressure of at least 1 Torr[9]. Furthermore, deposited films were obtained when PDMAT was heated to 120 ^oC, while heating at lower temperatures, 65-110 ^oC, reported in literature[11,12,17], was unsuccessful in obtaining deposited films for our system. Secondly, as it was necessary to increase the PDMAT temperature after successive experiments, in order to achieve sufficient vapour pressure to realize depositions, it is expected that this initial heating may have changed the molecular structure of the precursor thereby increasing its temperature of evaporation, as reported in literature[15]. It is likely that since the PDMAT solid comprised of non-uniformly sized particles, continual heating, melting, evaporating and cooling may have led to uneven particle decomposition so that the residue consists of completely burnt particles as well as some that are only partially melted; an increase in temperature therefore provides the required energy for these partially melted particles to further decompose. In addition, the presence of the residue suggests that yield from the precursor is not ideal. This was confirmed in literature by a final PDMAT weight loss after heating of approximately 75 % for new precursor and 60 % for a previously heated precursor sample[15].

Another consideration for ALD is the effect of the PDMAT behaviour on its exposure. Ideally, once a sufficiently high vapour pressure is attained to saturate the surface of the sample, a solid precursor can be utilized[19]. In this work N_2 is used as a purging as well as precursor carrier gas so that it aids in delivering the PDMAT to the chamber by building sufficient vapour pressure in the cannister to remove the precursor. In general, the 50 sccm N_2 flow chosen for film deposition was sufficient for delivery of both precursors, evidenced by the presence of the TaO films. The challenge presented by the changes in PDMAT evaporation temperature with successive heating and cooling cycles, however, could impact film growth. It is assumed that by increasing the PDMAT temperature sufficient vapour enters the chamber, saturating the sample surface, but this may not necessarily be the case as precursor melting and evaporation in the cannister occurs unevenly. In situ measurements such as those from a quartz crystal microbalance (QCM) has typically been used to measure mass uptake during precursor and ALD cycles[37,38], and can thus clarify the ability of PDMAT to deliver sufficient vapour for surface saturation. The QCM can also be utilized to determine the consistency of precursor mass uptake over the duration of the ALD deposition. It is believed that this type of study is necessary for this Ta_2O_5 system of fabrication but for now it is left to the category of future work.

Finally, as the purpose of fabricating TaO films by ALD was for their use as high-κ dielectric films on PCD surfaces for MOS devices, depositions were performed on PCD surfaces. Figure 23 shows the SEM images for TaO films deposited for the various H_2O vapour exposures 0.1, 0.3 and 0.4 s, on

as-grown PCD films, for 200, 100 and 100 cycles, respectively. The scale used makes it difficult to effectively compare the GPCs with those obtained in the graph of Figure **18**(b) but the TaO films are shown to be continuous, and conformal to the PCD surface. This result demonstrates that continuous films of approximately 20-30 nm can be achieved on the PCD surface by ALD, enabling its use in MOS structures at least from the perspective of fabrication.

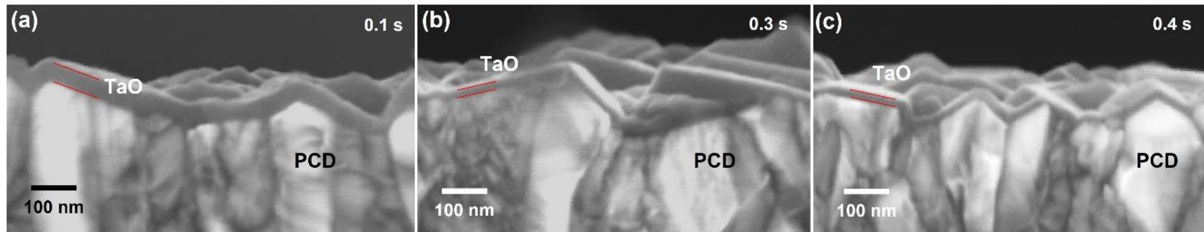

Figure 23: TaO films on as-grown PCD surfaces deposited with different H_2O exposure times 0.1 s, 0.3 s, and 0.4 s, for 200, 100 and 100 ALD cycles, respectively.

4.0 Conclusions

TaO films were deposited by ALD using precursors, PDMAT and H_2O, in the range 250-280 ^oC and with H_2O exposures, 0.1-0.4 s. The results showed that films deposited at 270 ^oC displayed the lowest GPC of 0.13 nm/cycle, which was explained by the lower partial pressure of PDMAT and thus loss of surface species at this temperature, while films deposited at the other temperatures realized higher GPCs of approximately 0.20 nm/cycle. The increase in GPC from 270 to 280 ^oC was attributed to decomposition of the PDMAT precursor. Saturation studies performed for various H_2O vapour exposures, 0.1-0.4 s, at 270 ^oC determined that the lowest GPC occurred for the 0.3 s exposure. In addition, XRD studies showed that films grown under these conditions displayed an obvious δ-Ta_2O_5 crystalline phase, compared to films at other exposures.

Discussion of the deviation from saturation and overall film properties for depositions at 270 ^oC centred on the behaviour of the PDMAT precursor both in the cannister and the chamber. Based on studies in literature, it is concluded that at 270 ^oC the PDMAT partial pressure decreases in the chamber, contributing to fewer surface sites and lower GPCs. In accordance with the observations made with respect to the behaviour of the solid PDMAT particles in the cannister, however, it is believed that inconsistencies in exposure may also stem from the uneven heating and thus decomposition to the vapour phase, of the solid particles. Furthermore, continual heating, melting, evaporating and cooling seemed to change the molecular structure of the precursor thereby necessitating increases in cannister temperature from 120 to 140 ^oC in successive depositions so that TaO films could be attained. These challenges are believed to be central to the understanding of ALD TaO films utilizing PDMAT.

Finally, continuous and conformal TaO films, 20-30 nm, were achieved on PCD surfaces by ALD as demonstrated by SEM images. This result highlights the ability of this oxide-semiconductor combination to be successfully fabricated and thus explored for MOS devices.

1 S. Korkos, N. J. Xanthopoulos, M. A. Botzakaki, C. Drivas, S. Kennou, S. Ladas, A. Travlos, S. N. Georga and C. A. Krontiras, *J. Vac. Sci. Technol. A*, 2020, **38**, 032402.

2 S. W. Smith, K. G. McAuliffe and J. F. Conley, *Solid. State. Electron.*, 2010, **54**, 1076–1082.

3 J. W. Liu, M. Y. Liao, M. Imura, E. Watanabe, H. Oosato and Y. Koide, *J. Phys. D. Appl. Phys.*, 2014, **47**, 245102.

4 K. V Egorov, Y. Yu, A. M. Markeev and O. M. Orlov, *Appl. Surf. Sci.*, 2015, **356**, 454–459.

5 Y. Abbas, A. S. Sokolov, Y. Jeon, S. Kim, B. Ku and C. Choi, *J. Alloys Compd.*, 2018, **759**, 44–51.

6 A. Jaggernauth, J. C. Mendes and R. F. Silva, *J. Mater. Chem. C*, 2020, **8**, 13127–13153.

7 I. Reklaitis, E. Radiunas, T. Malinauskas, S. Stanionytė, G. Juška, R. Ritasalo, T. Pilvi, S. Taeger, M. Strassburg and R. Tomašiūnas, *Surf. Coatings Technol.*, 2020, **399**, 126123.

8 J. Sundqvist, H. Högberg and A. Hårsta, *Chem. Vap. Depos.*, 2003, **9**, 245–248.

9 D. M. Hausmann, P. De Rouffignac, A. Smith, R. Gordon and D. Monsma, *Thin Solid Films*, 2003, **443**, 1–4.

10 K. Kukli, M. Ritala and M. Leskela, *J. Electrochem. Soc.*, 1995, **142**, 1670–1675.

11 W. J. Maeng and H. Kim, *Electrochem. Solid-State Lett.*, 2006, **9**, 191–194.

12 T. Gougousi and L. Ye, *J. Phys. Chem. C*, 2012, **116**, 8924–8931.

13 J. C. F. Rodríguez-Reyes and A. V. Teplyakov, *Chem. - A Eur. J.*, 2007, **13**, 9164–9176.

14 S. Klejna and S. D. Elliott, *Chem. Mater.*, 2014, **26**, 2427–2437.

15 H. Koyama, S. Tanimoto, K. Kuroiwa and Y. Tarui, *Jpn. J. Appl. Phys.*, 1994, **33**, 629–628.

16 P. Violet, I. Nuta, C. Chatillon and E. Blanquet, *Rapid Commun. Mass Spectrom*, 2010, **24**, 2949–2956.

17 J. Li, J. Wu, J. Liu and J. Sun, *Nanoscale Res. Lett.*, 2019, **14**.

18 T. Partida-Manzanera, J. W. Roberts, T. N. Bhat, Z. Zhang, H. R. Tan, S. B. Dolmanan, N. Sedghi, S. Tripathy and R. J. Potter, *J. Appl. Phys.*, 2016, **119**, 025303.

19 M. Leskela and M. Ritala, *Thin Solid Films*, 2002, **409**, 138–146.

20 T. Henke, M. Knaut, M. Geidel, F. Winkler, M. Albert and J. W. Bartha, *Thin Solid Films*, 2017, **627**, 94–105.

21 T. Jõgiaas, R. Zabels, A. Tamm, M. Merisalu, I. Hussainova, M. Heikkilä, H. Mändar, K. Kukli, M. Ritala and M. Leskelä, *Surf. Coatings Technol.*, 2015, **282**, 36–42.

22 T. Wang and J. G. Ekerdt, *J. Electrochem. Soc.*, 2011, **158**, G185.

23 M. Jenkins, D. Austin, K. E. Holden, D. Allman and J. Conley, *IEEE Trans. Electron Devices*, 2019, **66**, 5260–5265.

24 J. Liu, S. Cheng, M. Liao, M. Imura, A. Tanaka, H. Iwai and Y. Koide, *Diam. Relat. Mater.*, 2013, **38**, 24–27.

25 S. Cheng, L. Sang, M. Liao, J. Liu, M. Imura, H. Li and Y. Koide, *Appl. Phys. Lett.*, 2012, **101**, 1–6.

26 B. Abendroth, T. Moebus, S. Rentrop, R. Strohmeyer, M. Vinnichenko, T. Weling, H. Stöcker and D. C. Meyer, *Thin Solid Films*, 2013, **545**, 176–182.

27 E. . Skopin, K. Abdukayumov, P. Abi Younes, M. Anikin, H. Roussel, J. L. Deschanvres and H. Renevier, *Thin Solid Films*, 2021, **723**, 138591.

28 Q. Xie, Y. L. Jiang, C. Detavernier, D. Deduytsche, R. L. Van Meirhaeghe, G. P. Ru, B. Z. Li and X. P. Qu, *J. Appl. Phys.*, 2007, **102**, 083521.

29 D. Thian, Y. T. Yemane, S. Xu and F. B. Prinz, *J. Phys. Chem. C*, 2017, **121**, 27379–27388.

30 J. Dendooven, S. Pulinthanathu Sree, K. De Keyser, D. Deduytsche, J. A. Martens, K. F. Ludwig and C. Detavernier, *J. Phys. Chem. C*, 2011, **115**, 6605–6610.

31 J. W. Lim, J. S. Park and S. W. Kang, *J. Appl. Phys.*, 2000, **87**, 4632–4634.

32 S. M. George, *Chem. Rev.*, 2010, **110**, 111–131.

33 K. Kukli, M. Ritala, R. Matero and M. Leskela, *J. Cryst. Growth*, 2000, **212**, 459–468.

34 Q. Lv, M. Huang, S. Zhang, S. Deng, F. Gong, F. Wang, Y. Pan, G. Li and Y. Jin, *Coatings*, 2018, **8**, 150.

35 L. Enríquez, V. Sosa, F. Gamboa, I. Perez and C. Iv, *J. Alloys Compd.*, 2017, **712**, 303–310.

36 N. Kumar, A. P. Tiwari and J. Kumar, in *2nd International Symposium on Physics and Technology of Sensors*, IEEE, 2015, 214–218.

37 J. Cai, Z. Ma, U. Wejinya, M. Zou, Y. Liu, H. Zhou and X. Meng, *J. Mater. Sci.*, 2019, **54**, 5236–5248.

38 M. Reinke, Y. Kuzminykh and P. Hoffmann, *J. Phys. Chem. C*, 2016, **120**, 4337–4344.

Chapter 4: ALD of Titanium Oxide Films and their Energy Band Alignment with Polycrystalline Diamond

1.0 Introduction

Much investigation has been expended on the realization of TiO_2 films by ALD via a selection of various Ti and O precursors and deposition temperatures. Common Ti precursors include Ti halides such as $TiCl_4$ and TiI_4[1-4], Ti tetraisopropoxide (TTIP)[5-7] and tetrakis(dimethylamido) Ti (TDMAT)[7-10]. In general, TiO_2 films resulting from TDMAT and H_2O precursors, describe the tendency of a decreasing GPC with increasing temperature but a maintained surface saturation, explained by the presence of fewer active surface sites with increasing temperature and thus a decrease in GPC[7,9,11]. This deviation from a characteristic ALD window, typically defined by a constant GPC across a temperature range, is a revealing insight in ALD understanding, the occurrence of which has been clarified in literature[9,11,12]. Nevertheless, analysis of surface species saturation, described by a constant GPC, has been reported for TiO_2 film proliferation for temperatures as low as 50 ºC[11] and between 120-150 ºC[9]. Among the differences leading to these results, is the TDMAT temperature, 30 ºC for the former and 75 ºC for the latter[9,11]. In addition, a higher temperature of 250 ºC was also reported to lie in the ALD window[13]. GPC values realized for TiO_2 films, deposited by TDMAT and H_2O, range from 0.33 – 1.4 Å/cycle[7,9,11,13].

The TDMAT molecule comprises a central Ti atom bonded to four N atoms, each of which are then bonded to 2 methyl (CH_3) groups. Its decomposition has typically been investigated via substrate surface reactions, from which it was determined that decomposition is primarily due to surface adsorption at temperatures < 200 ºC; more specifically, the TDMAT molecule is thought to react with a surface in a pre-adsorbed state which facilitates reaction with H, attached to C or N in TDMAT, to release one dimethylamine thus permitting the remaining Ti intermediary to adsorb to the surface[14,15]. At these ‘low’ temperatures, dimethylamine is found to be the major product of decomposition followed by methane[15]. TDMAT decomposition rates at surfaces are also shown to increase at temperatures > 200 ºC, accompanied by gas phase reactions as other decomposition pathways compete with surface reactions[15]. This decomposition was thought to result from metallacycle formation of the Ti-C-N ring resulting from the transfer of a proton to a dimethylamino group, together with β-hydride elimination reactions[14]. In addition, for temperatures > 260 ºC, Arrhenius parameters, activation energy and preexponential factor, were shown to be consistent with gas phase unimolecular decomposition of a complex molecule, while those for lower temperatures described an activated adsorption process[14]. On the other hand, surface decomposition of pure dimethylamine was experimentally shown to occur above 275 ºC[15].

TiO_2 thin films are advantageous in (sub)microelectronic applications, especially as dielectric layers in MOS devices because of their relatively high dielectric constant, κ. ALD films, with

thicknesses < 20 nm, obtained from Ti precursor TDMAT were reported as exhibiting κ values between 25-80[16-19]. The general tendency of an inversely proportional relationship between κ and energy bandgap, E_g, dictates that a high-κ dielectric displays low E_g, which is indeed the case for TiO_2, having exhibited a low E_g of 3.2-3.7 eV[17,20,21]. High-κ TiO_2 films can therefore facilitate current leakage across the oxide-semiconductor interface due to its small E_g, rendering the film unsuitable for this application. These leakages are, however, alleviated by using TiO_2 in tandem with other dielectrics having larger E_g, such as Al_2O_3 or HfO_2, which create larger band offsets at the semiconductor interface. The result is a nanolaminate or gate stack in which a compromise is realized between E_g and κ[19,22]. Interfacial layers resulting from TiO_2 deposition and annealing parameters were also shown to modulate film E_g[21]. In addition, electronic transport within amorphous TiO_2 films further complicates MOS structure conductivity but can be controlled by deposition parameters. TiO_2 electronic transport was demonstrated as being due to the presence of Ti^{3+} defects, incorporated during ALD, increases in which led to increased n-type conductivity[23], while p-type conductivity was measured for films with a large number of Ti vacancies[24]. This result may thus confound the source of leakage current across the TiO_2-semiconductor interface, whether due to TiO_2 film conductivity or energy band alignment.

The utilization of TiO_2 as a gate dielectric or passivation layer specifically for diamond MOS electronic devices is rare. Liu et al. have reported on its use, in concert with Al_2O_3, as a bilayer gate dielectric for single crystal diamond MOSFETs and MOSCAPs[25]. A leakage current of 2.1E-5 Acm^{-2} was obtained at -4 V and a maximum drain–source current, I_{DS}, of -11.6 $mAmm^{-1}$ was measured[25]. In addition, it was determined that the valence band offset (ΔE_V) for this bilayer dielectric with H-terminated diamond was 2.3 eV, sufficient for preventing the uncontrolled passage of charge carriers across the dielectric[25]. DFT calculations performed for anatase TiO_2 on single crystal (100) diamond concluded the presence of interface states, which were shown to be suppressed by the prevalence of H-terminations on diamond[26]. These terminations also acted to increase the ΔE_V from 0.6 to 1.7 eV[26]. Despite few incidences in the study of TiO_2 dielectrics for diamond-based electronics, electrical characterization of FETs employing them has been reported for organic and high-electron-mobility semiconducting materials[17,19].

The work presented here explores the fabrication of TiO films on PCD by ALD with the overall aim of determining their energy band alignment. The heterogeneous nature of the PCD surface, characterized by sp^3 C and sp^2 C from graphite and polymeric chains, with predominant H-terminations for as-grown films, together with a variety of crystallographic orientations and grain boundaries[27], has not previously been studied for its surface modifications upon exposure to ALD precursors for TiO films, neither has the energy band alignment of TiO films on PCD been determined. This study therefore presents the fabrication of TiO films by ALD utilizing precursors, TDMAT and H_2O, over a variety of parameters, and uses this understanding of film growth by a particular set of conditions to analyze reactions on the PCD surface, thus determining the energy band structure of the two films in contact. In addition, it examines the quality of the TiO-H-PCD interface with respect to the band alignment and TiO film composition. This work thus enriches the discussion pertaining to the application of TiO films as high-κ dielectrics for PCD MOS devices.

2.0 Experimental Procedure

2.1. TiO Film Fabrication by ALD

TiO films were fabricated on p-type Si (100) substrates by ALD with tetrakis(dimethylamido) titanium (TDMAT)and H_2O precursors. The substrates were pre-treated with piranha solution, H_2SO_4 and H_2O_2 in the ratio 3:1, for 30 minutes. An ALD half cycle was described by the duration of open valve–exposure (residence)–purge. The TDMAT half cycle was therefore 0.2 s–4 s–20 s, and that for H_2O, 0.07 s–4 s–30 s. N_2 gas was used as the precursor carrier and purging gases and set at 40 sccm during deposition; purging of the chamber prior and subsequent to depositions was performed for N_2 at 100 sccm. To determine temperature dependence, films were deposited at temperatures 180-220 ^{o}C for 400 cycles. TDMAT was maintained at 70 ^{o}C, the H_2O valve at 90 ^{o}C, while its canister remained at room temperature, and the line temperatures set to 100 ^{o}C to prevent precursor condensation. To determine saturation conditions, the chamber temperature was set to 210 ^{o}C and the exposure time for TDMAT and H_2O was varied between 2-8 s.

2.2. TiO Films on PCD Surfaces

2.2.1 *Growth of PCD Films by HFCVD*

Si p-type <100> substrates, approximately 1 cm^2, were cleaned in isopropanol using ultrasonication for 10 minutes then dried in a stream of compressed air. They were subsequently seeded with diamond particles measuring 40-60 µm; each sample was placed in a separate beaker containing a suspension of 0.5 g diamond particles and 5 ml ethanol, and underwent ultrasonication for 1 hour. The samples were then removed from the diamond particle suspensions and cleaned by rinsing in flowing ethanol, and ultrasonication in ethanol for 2 minutes, twice, each time changing the ethanol.

B-doped PCD films were grown onto the seeded Si by HFCVD using a custom-built system. Substrates were placed onto the sample stage in the HFCVD chamber, under at least two tungsten filaments; in total five tungsten, 0.3 mm diameter filaments were used in this deposition, and the stage was placed at least 12 mm from the filaments during this first stage of carburization. The chamber was evacuated and 6 % CH_4/H_2 was introduced into the chamber until a pressure of 7.5 kPa was attained. Carburization of the filaments was achieved at 2250 ^{o}C after about 20 minutes. The sample stage was then raised to approximately 6 mm from the filaments and the ratio CH_4/H_2 was set to 5 %. The power through the filaments was increased to achieve a substrate temperature of 800 ^{o}C and diamond growth proceeded for a total of 60 minutes. The substrate temperature was maintained between 785-800 ^{o}C, and B precursor and carrier gas flow rates of 1.0 µl/min B_2O_3 in ethanol (10 000 ppm) and 4 ml/min Ar, respectively, were used. At the end of the total growth, lasting 1 h, all the gases were turned off except H_2, and the power through the filaments was slowly decreased until zero or until the filaments broke.

2.2.2 *ALD TiO films on PCD*

As-grown (H-PCD) films were placed into the ALD chamber and TiO films were deposited at 200 °C for TDMAT half cycle was therefore 0.2 s–4 s–20 s, and that for H_2O, 0.07 s–4 s–2 0 s, with all other conditions set as in Section 2.2.

2.3. Characterization Techniques

The resulting TiO films on Si were characterized by XRF and XRR as described in Section 2 of Chapter 3 for TaO films. The Ti loading was instead obtained by consideration of the Ti Kα and Ti Kβ signals at 4.51 keV and 4.93 keV, respectively. Similarly, the sum of counts for both peaks were considered for Ti intensities and normalized with respect to the Si signal.

SEM images were obtained using Hitachi S4100 with accelerating voltages 15‑25 kV.

XPS measurements were carried out at the Nova School of Science and Technology, Department of Materials Science, Universidade Nova de Lisboa in Lisbon, Portugal. They were performed using Kratos Axis Supra with monochromatic Al Kα x-ray source. Survey (wide scan) scans used an x-ray power of 180 W and pass energy of 160 eV, while detailed scans were done with 225 W x-ray power and 10 eV pass energy.

3.0 Results and Discussion

3.1. Fabrication of Titanium Oxide Films

The XRF spectra of Figure 24(a) in accordance with the corresponding graph of Figure 24(b) demonstrate the change in Ti loading of the resulting films with respect to deposition temperature. Figure 24(b) takes into consideration both the Si (not shown) and Ti Kα emissions to better represent the Ti loading with respect to the Si substrate. The graph shows that Ti loading decreases from 180 to 190 °C, after which it exhibits an overall increase. There is a noted discrepancy from 210 to 220 °C where Ti/Si intensities remain higher than those at 190 and 200 °C, although it decreases from 210 to 220 °C. This could be attributed to film non-uniformity as different colourations of individual TiO_2 films, evidencing uneven film thicknesses, had been observed. It is expected that Ti loading is positively correlated to GPC, as was evidenced in Figure 19 of Chapter 3 in the graph of film thickness with Ta/Si intensity for TaO films, thus the graph of Figure 24(b) may also be taken to represent the GPC trend across the temperature range. High GPC values are known to occur at both low and high ALD temperatures for TiO_2 films deposited by TDMAT and H_2O, hence the particular trend of a decreasing GPC with increasing temperature until a minimum, followed by a subsequent increase, is commonly reported[9,11,28]. The higher Ti loading at 180 °C is thus expected, due to a higher GPC, as is the successive increase in GPC from 200 °C; this minimum value for GPC corresponds to that experimentally obtained in literature[28]. At lower temperatures, high GPC values have been related to the presence of more surface species, which succumb to desorption at higher temperatures, giving rise to lower GPC values[11],

demonstrated here between 180-190 °C. Further increases in temperature, beyond that of precursor decomposition realizes a departure from self-limiting behaviour and thus an increase in GPC[11,29]. TDMAT decomposition rates have been shown to increase with temperatures >200 °C, leading to both surface and gas phase reactions, as opposed to only surface reactions at lower temperatures[15]. It is likely that this explains the results presented here, where the GPC increases for depositions carried out at temperatures >200 °C.

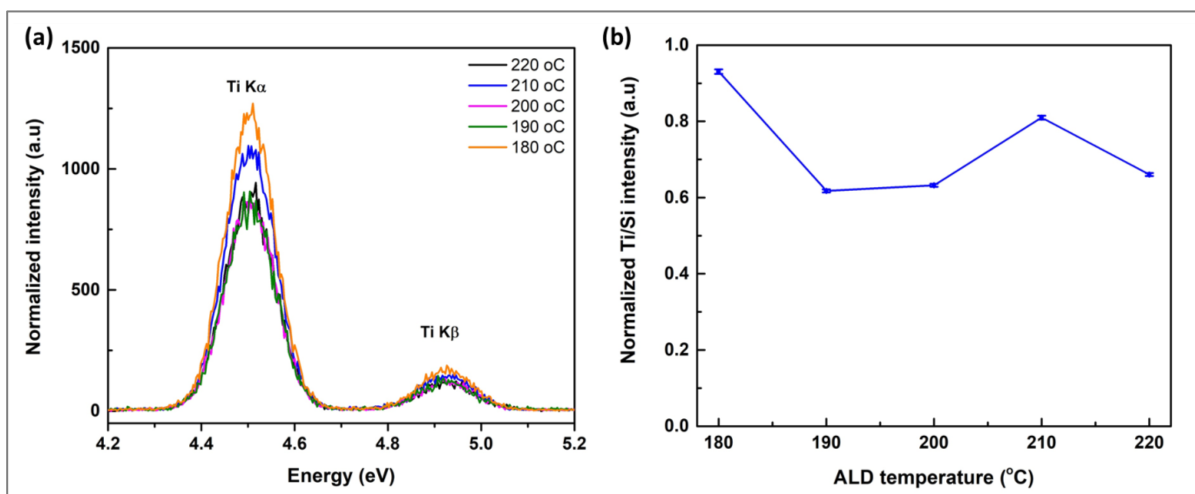

Figure 24: (a) XRF spectra showing Ti signals, normalized for 400 cycles, for TiO films deposited at ALD temperatures 180 – 220 °C, with precursor residence times of 4 s each; (b) graphically represents the normalized Ti/Si intensities obtained for the films across the temperature range, thus demonstrating the Ti loading with respect to ALD temperature.

Subsequent experiments performed at 210 °C are shown in Figure 25(a) and (b) and highlight the conditions for precursor saturation. It should be noted that the exposure duration here refers to residence time, the time for which the precursor is forced to remain in the chamber succeeding its pulse. It was introduced into the ALD cycle to increase the time given to precursor surface migration, thus aiming to optimize surface saturation without increasing the amount of precursor, i.e., the pulse time. The residence time was set to be equal for both precursors, while the pulse times for TDMAT and H_2O were set at 0.2 and 0.07 s, respectively, however, saturating conditions seem to be approximated near residence times of 8 s. This suggests that for the precursor doses entering the chamber, a residence time of at least 8 s is needed to complete surface reactions, although it is not clear to which precursor, TDMAT or H_2O, this requirement belongs, as they are changed together. Despite the same dose of precursors being delivered to the chamber, the higher Ti loading at 3 and 4 s residence durations substantiates the influence of this parameter, imposed by at least one of the precursors. In general, shorter exposure times can be associated with limitations to precursor molecule surface migration, and incomplete surface reactions[30]. Another explanation lies in the TDMAT decomposition at this temperature, greater than 200 °C[15], and the possible requirement of a longer residence time to homogenize the surface as reactions may no longer be self-limiting. Interestingly, the Ti loading for the 8 s residence time at 210 °C is close to that for depositions at 200 and 220 °C.

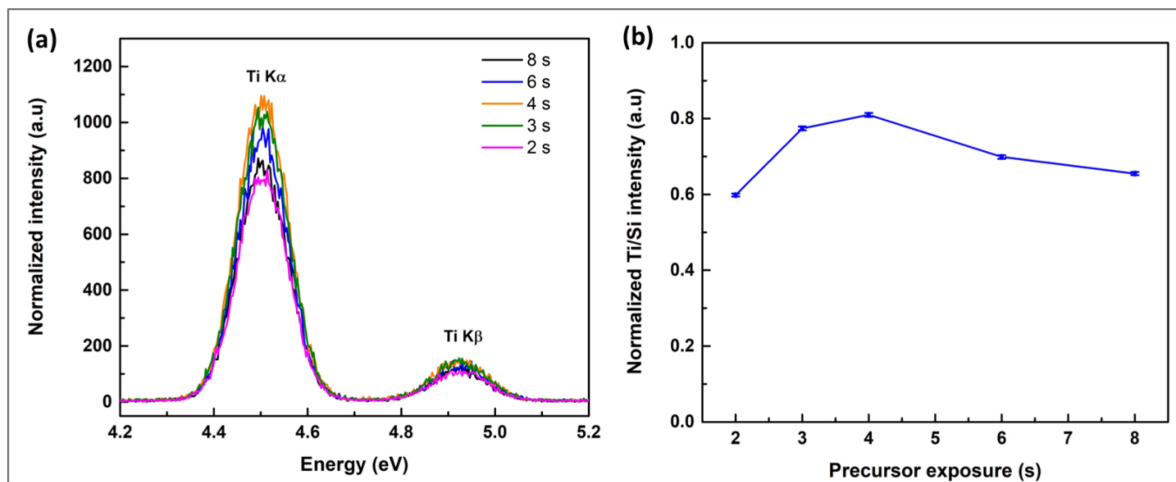

Figure 25: (a) XRF spectra showing Ti signal for TiO films deposited at precursor residence times 2- 8 s at 210 °C; (b) graphical representation of the Ti/Si intensity obtained for films across the residence durations, thus highlighting parameters for saturation.

Investigation of the decomposition of TDMAT in an N_2 environment concluded a 'drastic' increase in its conversion rate with temperatures exceeding 205 °C, and identified the presence of 'new' species in measured infrared spectra, arising from additional decomposition pathways[15]. It is therefore considered for this work that at 210 °C TDMAT decomposes to form a variety of surface species which may not proceed as self-limiting reactions. The residence time, however, seems to influence these reactions, with a higher Ti loading related to fast but incomplete reactions and low surface migration at 4 s residence times, while longer durations, such as for 8 s, possibly favours species migration, complete surface reactions, even if not self-limiting, and an overall homogeneous surface species.

3.2. XPS Analysis of TiO Films

TiO films grown at 200 °C with 4 s residence times were analyzed by XPS (Figure 26). These ALD parameters were chosen as they resulted in films with a relatively consistent Ti loading over the investigated temperature range, and also because the reported increase in conversion rate of TDMAT was determined to occur at temperatures >205 °C[15].

The wide scan spectrum showed the presence of N, around 400 eV, suggesting that a small amount of N from the amine groups of TDMAT precursor remains in the film. ALD half reactions involving the $-Ti(N(CH_3)_2)_3$ surface species are known to progress through the reaction of $-N(CH_3)_2$ with H_2O, resulting in the proliferation of TiO_2 as shown in reaction (1)[11], where * denotes surface species. The second half reaction with TDMAT is given in reaction (2)[11]. As such, the removal of N is ideal for attaining stoichiometric films.

$$TiO_2\text{-}O\text{-}Ti(N(CH_3)_2)_3^* + 2H_2O \rightarrow TiO_2\text{-}TiO_2\text{-}OH^* + 3\ TiN(CH_3)_2 \quad (1)$$

$$TiO_2\text{-}OH^* + Ti(N(CH_3)_2)_4 \rightarrow TiO_2\text{-}O\text{-}Ti(N(CH_3)_2)_3^* + NH(CH_3)_2 \quad (2)$$

Ti, O and C peaks were present in the XPS spectrum, and their individual contributions identified. The Ti2p doublet (Figure 26(b)) was fitted with one major peak each for $Ti2p_{1/2}$ and $Ti2p_{3/2}$, centred at 464.7 and 459.0 eV, respectively, for C 1s centred at 285.3 eV, while a small shoulder contribution at 457.9 eV is shown for Ti^{3+} phases, although not present for $Ti2p_{1/2}$, or Ti oxynitride groups[31,32]. The Ti2p doublet is due to spin-orbit splitting which occurs for an unpaired e^- present in p (as is the case for Ti), d or f orbitals, that is, those possessing angular momenta. The coupling between the spin and orbital momenta can be either parallel or anti-parallel, depending on the orientation of the e^- spin, with the latter having a lower total momentum but higher binding energy (BE). The doublet is thus representative of the two possible e^- spin states. In addition, degeneracy states exist for those having the same total angular momentum but different orientations in space, such that their magnetic quantum number changes. There are 4 states with a total momentum of 3/2, and 2 with a total momentum of 1/2 for p-orbital degeneracy, thus the doublet peak area ratio, obtained from the peak area of $Ti2p_{1/2}$ and $Ti2p_{3/2}$, should ideally by 1:2, and was determined to be 0.49 (approximately 1:2) for these TiO films.

Deconvolution of the O1s peak (Figure 26(c)) identified lattice O, Ti-O, at 530.4 eV, O-H bonds at 531.6 eV either adsorbed or due to the termination from the ALD reaction with H_2O precursor, and a small peak at 533.8 eV due to surface contamination in the form of O-C/O-(CH) bonds[7,32-34]. Adsorbed or terminating hydroxide groups are typically reported in literature for the peak at 531.6 eV, although it also been associated with an intrinsic component of the film or a natural asymmetry of the O1s signal[33]. The respective atomic concentrations, X_j, were calculated using equation (5), where A_j is the peak area of element j and S_j is its sensitivity factor. The atomic percentage of Ti, calculated from the $Ti2p_{3/2}$ peak, was determined to be 21.3 %, and that for O from the Ti-O lattice peak was 57.4 %. The Ti:O ratio therefore deviates from 1:2, which is expected for TiO_2 stoichiometry, signifying that the ALD conditions resulted in O-rich films with a ratio of 1:2.7. In addition, N accounted for about 5 % of the TiO lattice and the remaining 16 % from C surface contamination, although some could be contained in the film in the form of C-H and C-O bonds.

$$X_j = (A_j/S_j)/\sum (A_j/S_j) \quad (5)$$

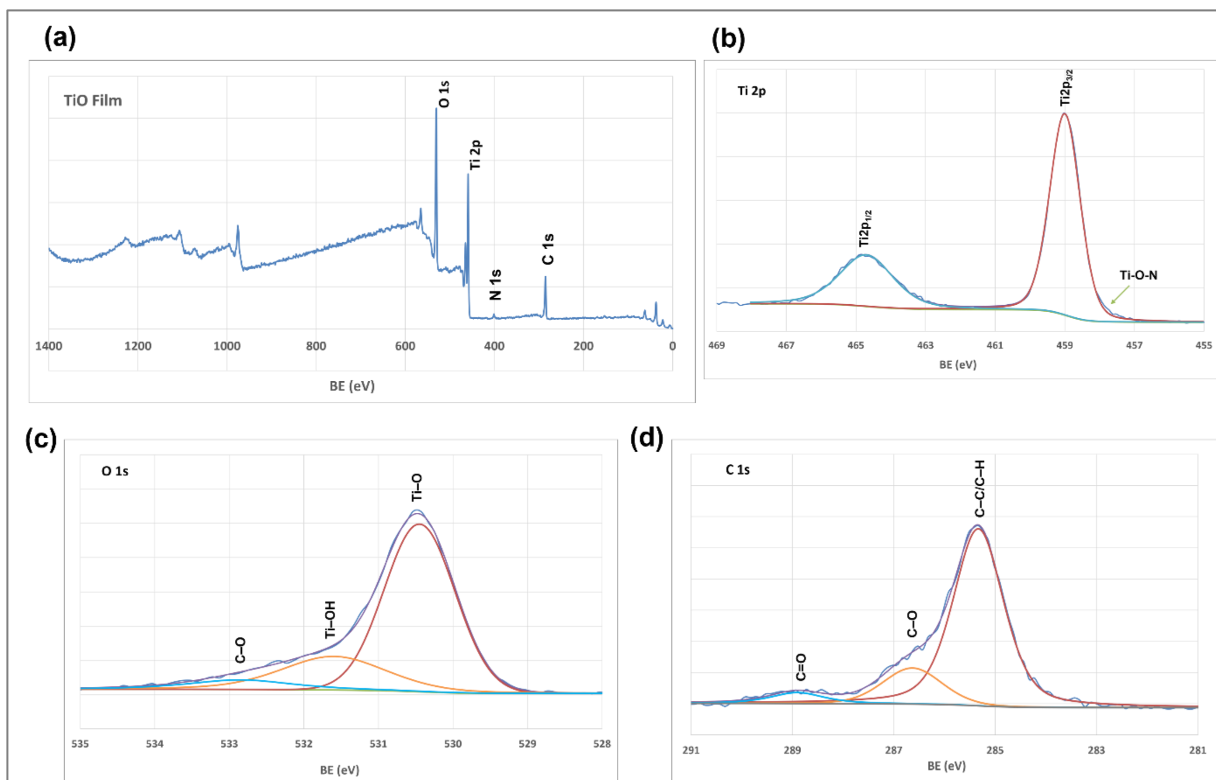

Figure 26: XPS spectra of TiO films deposited at 200 °C with 4 s precursor residence times; (a) widescan spectrum; (b) Ti2p doublet; (c) O1s peak showing lattice Ti-O and smaller contributions from O-H and O-C; (d) C1s peak showing contributions from C surface contamination as well as from unreacted precursor.

O contaminant ligands, resulting from parameter-dependent film growth mechanisms, are known to remain in TiO films. Studies of ALD TiO_2 films using TDMAT have shown 16 % O contaminant ligands for ALD at 90 °C, and, while considered to be almost negligible, have demonstrated their removal by annealing[7]. Moreover, films deposited at temperatures of 250 and 300 °C were found to be O-rich while those at 200 °C were the closest to stoichiometric[35]. The films analyzed by XPS were grown at 200 °C and were thus expected to be close to stoichiometric however, the introduction of precursor residence times of 4 s, the effect of which was not studied in this work, may have an influence in establishing high O incorporation.

3.3. Energy band alignment of TiO with H-PCD

TiO films were deposited onto H-PCD surfaces by ALD at 200 °C with precursor residence times of 4 s. H-PCD films are known to exhibit surface H-terminations, as they are cooled in H_2 plasma from temperatures of approximately 800 °C, subsequent to diamond film growth by CVD

techniques[27,36]. Figure 27 shows an image taken by SEM of the TiO film on PCD, revealing it to be continuous and conformal to the rough PCD surface.

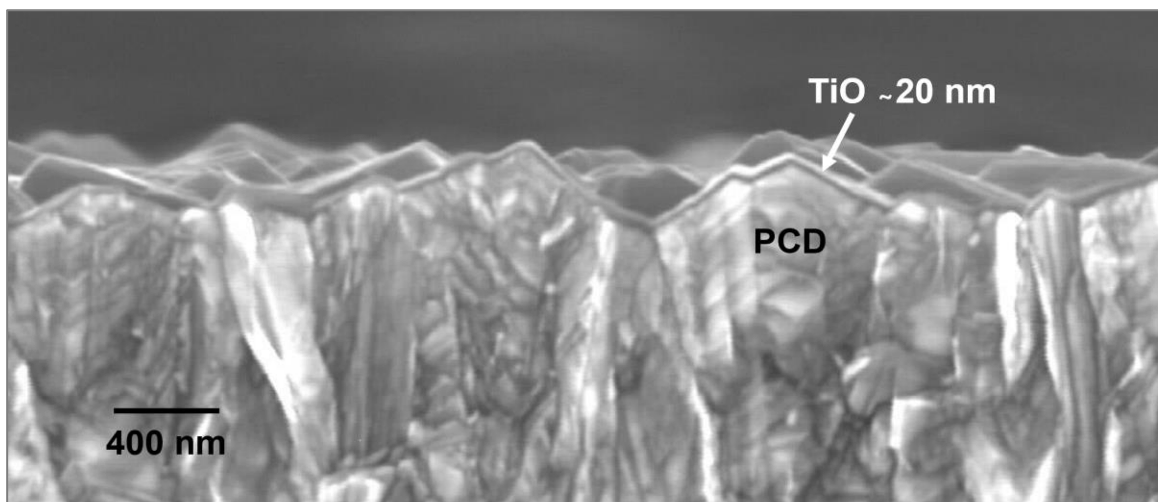

Figure 27: SEM micrograph showing ALD TiO film, approximately 20 nm, on a PCD surface

To fulfill the requirements for the calculation of energy band alignment using XPS analysis, XPS measurements were performed for three samples, a TiO film, 100 nm, a PCD film, 1 μm thick, and a sample with 2 nm TiO on PCD; this last sample was done to obtain the change in core level BEs at the interface; more discussion about this calculation, using the Kraut method[37], is given below. XPS analysis of the TiO film was presented in the previous section thus, what follows in this section is the XPS analysis for the H-PCD film and its surface modification upon exposure to the ALD precursors which give rise to a 2 nm TiO film.

3.3.1 Modification of the H-terminated PCD Surface by TiO Precursor Exposure

The XPS spectra for the H-PCD film are shown in Figure 28. The wide scan displays a large contribution for C1s and a much smaller contribution from O1s (Figure 28(a)). Deconvolution of the C1s peak shows sp^3 C, the primary contribution of the PCD structure, at 284.1 eV, and sp^2 C, which must be present due to the presence of graphite, grain boundaries and defects in PCD films, is seen at 283.7 eV. The peak at 284.7 eV is due to CH_x ($x > 1$) associated with the PCD surface and subsurface structure[38] as well as polymeric chains, while that at 285.5 eV is attributed to C-OH/C-O-C bonds from surface contamination or due to the growth process[27], typically occurring 1.2-1.6 eV higher than sp^3 C[39,40], and substantiating the presence of the O1s contribution. As-grown PCD films doped with B by the precursor, B_2O_3, were determined to possess a small amount of O surface ligands resulting from the O species in the gas mixture[41]. The H-PCD films analyzed here were also B doped using this precursor and as such they are expected to display some O surface ligands.

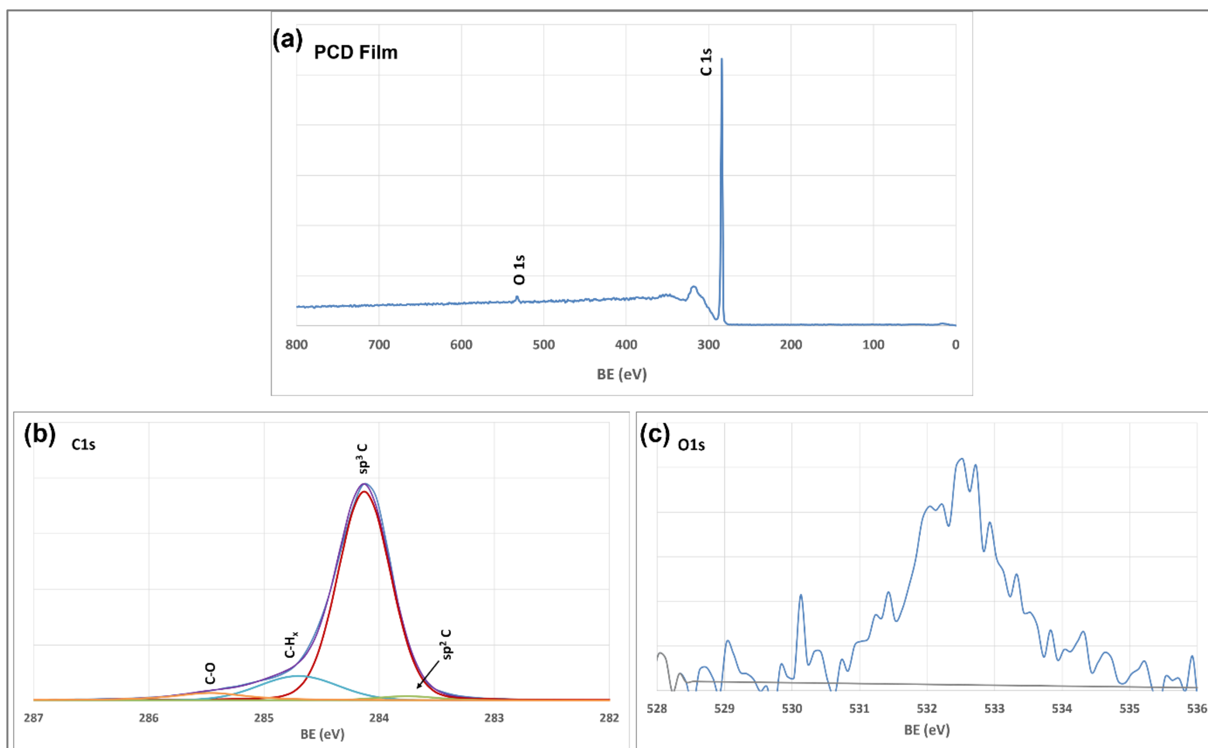

Figure 28: XPS spectra of PCD films showing (a) widescan with C1s and O1s peaks; (b) C1s peak, deconvoluted to show 4 contributing peaks; (c) small O1s contribution.

To identify interface contributions which lead to band bending, a sample of 2 nm TiO film on the H-PCD surface was analyzed by XPS (Figure 29). The widescan spectrum of Figure 29(a) shows contributions from Ti, C, O and N, with a stronger O1s signal compared to the PCD surface due to the presence of the TiO film. The Ti2p spectrum (Figure 29(b)) displays characteristic contributions from its doublet, $Ti2p_{1/2}$ and $Ti2p_{3/2}$, centred at 465.0 and 459.2 eV, respectively, for sp^3 C centred at 284.2 eV. The doublet peaks are located 0.2-0.3 eV higher than those of the 100 nm TiO film, and there are also additional smaller contributions at 458.2 and 460.7 eV, attributed to Ti^{3+} bonding[32], more present at the interface by more than twice the amount; 1.2 % in the 100 nm film compared to 2.7% for the 2 nm film. This can be explained by the heterogeneity of the PCD surface and hence the variety of bonds that may be formed during initial ALD cycles. Additionally, the O1s and C1s peaks of Figure 29(c) and (d), respectively, also validate sample heterogeneity signals originating from both the PCD surface as well as the nano-thin TiO film. O1s exhibits a major peak at 530.7 eV from Ti-O and a small peak at 531.7, necessitated by the fitting, attributed to Ti^{3+}. The broad O-H peak, centred at 532.2 eV, is due to lattice Ti-OH or surface terminations, as was seen with the 100 nm TiO film but also likely has contributions from the PCD surface upon reactions with the H_2O precursor, as C-OH. O-C and O=C groups at 533.4 and 536.5 eV, respectively, are also attributed to the PCD surface-precursor reactions. The O1s peak of the PCD film (Figure 28(c)) was measured to be a minor contribution but with the thin TiO film the change in the PCD surface with O exposure is better understood.

The C1s peak of Figure 29(d) further elucidates the changing PCD surface; peaks at 283.8, 284.2 and 284.7 eV correspond to structures of the PCD film, attributed to sp^2 C, sp^3 C and CH_x ($x > 1$) species, respectively, while those at 285.4, 286.7 and 289.2 eV arise from the changing surface. It should be noted that Ti-C bonds, which would have been present at BEs lower than Ti-O, were not measured in any of the spectra, signifying that the H-terminated PCD surface must then realize initial bonding through the minority O terminations of C-O, measured in the C1s spectrum at 285.4 eV, and present on the surface of the PCD film. TDMAT is thought to react with a surface in a pre-adsorbed state whereby one dimethylamine ligand is removed so that adsorption occurs via the Ti intermediary[14,15], and thus can be the case here for reaction with C-O groups, where C is dissociated in the reaction.

The difference between the C1s contribution from the uncoated H-PCD surface and that with 2 nm TiO film is the presence of the higher BE peaks of carbonyl (C=O) and carboxyl (HO-C=O) groups at 286.7 and 289.2 eV, respectively. This means that these groups originate from ALD precursor reactions with the PCD surface. Carbonyl and carboxyl groups are commonly measured on diamond surfaces exposed to O and have also been correlated with the specific diamond facet orientations[42-45]. It can therefore be proposed that upon exposure to H_2O in the ALD half cycle, at 200 ^oC and with a 4 s exposure, the formation of C=O bonds are facilitated through O reactions with neighbouring -H and -OH surface terminations, much like in the formation of ketones and aldehydes from alcohol oxidation. In contrast, carbonyl groups, coexistent with ether groups on oxidized (110) and (100) surfaces, are argued as being due to transitions from adsorbed peroxide (C-O-O-C) structures as well as an increase in the bond order of C-O with exposure to atomic O[42,45]. In both of these cases the extent of surface coverage tends to influence the particular mix of resulting surface bonds[42,45].

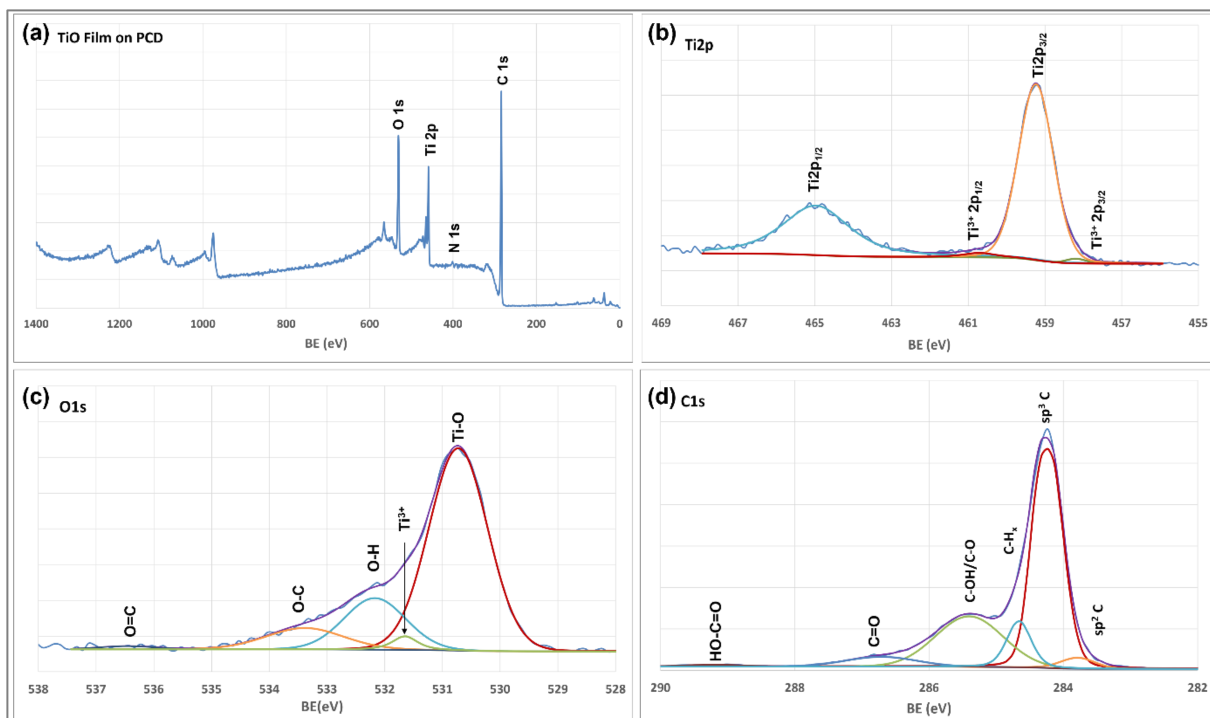

Figure 29: XPS spectra of 2 nm TiO films on PCD surface showing (a) widescan with C1s, O1s, Ti2p and N1s peaks identified; (b) Ti2p peak, deconvoluted to show both stoichiometric TiO_2 peaks as well as small Ti^{3+} contributions; (c) O1s peak primarily from Ti-O and (d) C1s peak showing contributions from the PCD structure as well as its changing surface with H_2O and TDMAT exposure.

The Ti2p signal and Ti-O peak from O1s verify proliferation of the TiO film from TDMAT and H_2O, principally from reactions (1) and (2). The range of PCD surface O bonds, however, may explain the presence of the Ti^{3+} phase apparent in Ti2p, not seen in the 100 nm TiO film. In addition, the Ti:O ratio was calculated to be 1:3.2, which suggests that, like its thicker counterpart, it is also O-rich but even more so, especially considering the presence of the Ti^{3+} phase. In the case of the heterogeneous PCD surface, with respect to surface energy, and the variety of C and O surface bonds attained from precursor exposure, the introduction of a precursor residence time may be pragmatic for assisting molecule surface migration and saturation, but it does not seem to curtail O incorporation.

3.3.2 Determination of the TiO-H-PCD Energy Band Alignment

Energy band alignment analysis was performed according to the Kraut method which determines heterojunction band discontinuities by considering the differences between the core level binding energies (BE) and valence band edges of the films on either side of the interface[37]. Band discontinuities arise because of a disruption in the charge distribution at the interface, relative to the distribution deeper into the bulk, whether caused by the presence of another material, or vacuum interface[37]. In this case, the interface is that of TiO-PCD, and the valence band discontinuity, ΔE_V, is given by equation (6), a more specific modification of equation (3):

$$\Delta E_V = \left(E_{CL}^{PCD} - E_V^{PCD}\right) - \left(E_{CL}^{TiO} - E_V^{TiO}\right) - \{E_{CL}^{PCD}(i) - E_{CL}^{TiO}(i)\} \quad (6)$$

E_{CL}^{PCD} – BE of core level (CL) peak for PCD film; (i) denotes BE for CL at interface
E_V^{PCD} – valence band edge of PCD film
E_{CL}^{TiO} – BE of core level (CL) peak for TiO film; (i) denotes BE for CL at interface
E_V^{TiO} – valence band edge of TiO film

The valence band offset, ΔE_V, is calculated from equation (6) and Table 4 summarizes the E_V and core level energies, E_{CL}, obtained from the individual XPS spectra, previously discussed, used for the band alignment calculations. In addition, Figure 30(a)-(c) shows the E_V values obtained for each sample by obtaining linear fits for both the background and the initial rise in energy for the spectrum and taking their point of intersection[46-48]. E_V for the TiO film on PCD surface was calculated to be 3.06 eV, while the band bending at the PCD surface was determined to be 0.13 eV, derived from the difference between ΔE_{CL} for PCD at the interface and its E_V in the bulk. A diagrammatic representation of the band alignment is thus provided in Figure 30(d) with the calculated values highlighted and bandgap energies for diamond and TiO obtained from references[13,25]. PCD band bending, by 0.13 eV, is represented as a downward bend due to the p-type conduction of B doping. Theoretical and experimental values of ΔE_V for TiO on H-terminated single crystal diamond, reported in literature, range from 0.6-2.6 eV[26,49], lower than the 3.06 eV calculated for our films. The introduction of H on the diamond surface however, was thought to increase band offsets, and is also dependent on the particular C structures and TiO phases in contact[26,50], which may provide an explanation for the larger ΔE_V. TiO_2 (001)/C (100) heterostructures with and without H terminations, for example, exhibited theoretical ΔE_V in the range 2.3-4.1 eV[26], and TiO_2 phases, rutile and anatase, were shown to display different electron affinities and ionization potentials due to differences in chemical bonding and coordination environments, thus varying their energy band structures[50]. The 3.06 eV ΔE_V reported here can therefore be due to the influence of the high O content or mixed Ti^{4+} and Ti^{3+} TiO films, in addition to the heterogeneous H-PCD surface.

Table 4: Measured and calculated values for the core level and valence band BEs, E_{CL} and E_v, respectively, for determination of the valence band offset (ΔE_V)

Sample	Measured data			Calculated data					
	E_{CL} (eV)		E_V (eV)	E_{CL} - E_V (eV)		ΔE_{CL} (i) (eV)		ΔE_V (eV)	PCD band bending (eV)
	Ti 2p	sp^3C		Ti 2p	sp^3C	Ti 2p	sp^3C		
TiO 100nm	459.00		3.17	455.83					
PCD Film		284.08	0.21		283.87				
TiO2nm-PCD	459.23	284.21	3.27			3.40	0.34		
								3.06	**0.13**

Notably, the band alignment diagram of Figure 30(d) also reveals a 0.11 eV separation between the CBM of TiO and the VBM of PCD, which may have implications for interface quality. Based on the XPS characterization of the films, two sources of conduction can be understood, the first is due to that of the TiO films and the second due to the interface. The presence of Ti^{3+} in TiO films has been linked to film conductivity due to the formation of a defect band above the VBM[23,51]. Furthermore, the presence of O vacancies, energetically favourable for formation in amorphous TiO films, and due to the Ti^{3+} phase, was thought to function as a hole transfer channel responsible for film conductivity[51]; this property was also argued as being due to small polaron or variable range hopping between Ti^{3+} and Ti^{4+} sites[23,52]. In this work the thin TiO films on the PCD surface contained Ti^{3+} together with over stoichiometric TiO_2, meaning that an O deficient phase, possibly due to O vacancies, as well as O rich phase coexist. It is therefore expected that, at least in these 2 nm of TiO with the H-PCD interface, recombination or even conduction may occur. In addition, the p-type conductivity of the PCD films, by B-doping, may provide opportunities for conductivity across the interface facilitated by the 0.11 eV offset between the CBM of TiO and VBM of PCD, but whether it appears as recombination of h^+ and e^- over only a few monolayers thus preventing conductivity into a thicker TiO film, or as a continuous conduction channel across both films, due to the excess O (holes) in TiO, requires further investigation, and would elucidate the integrity of the TiO-PCD interface for MOS devices.

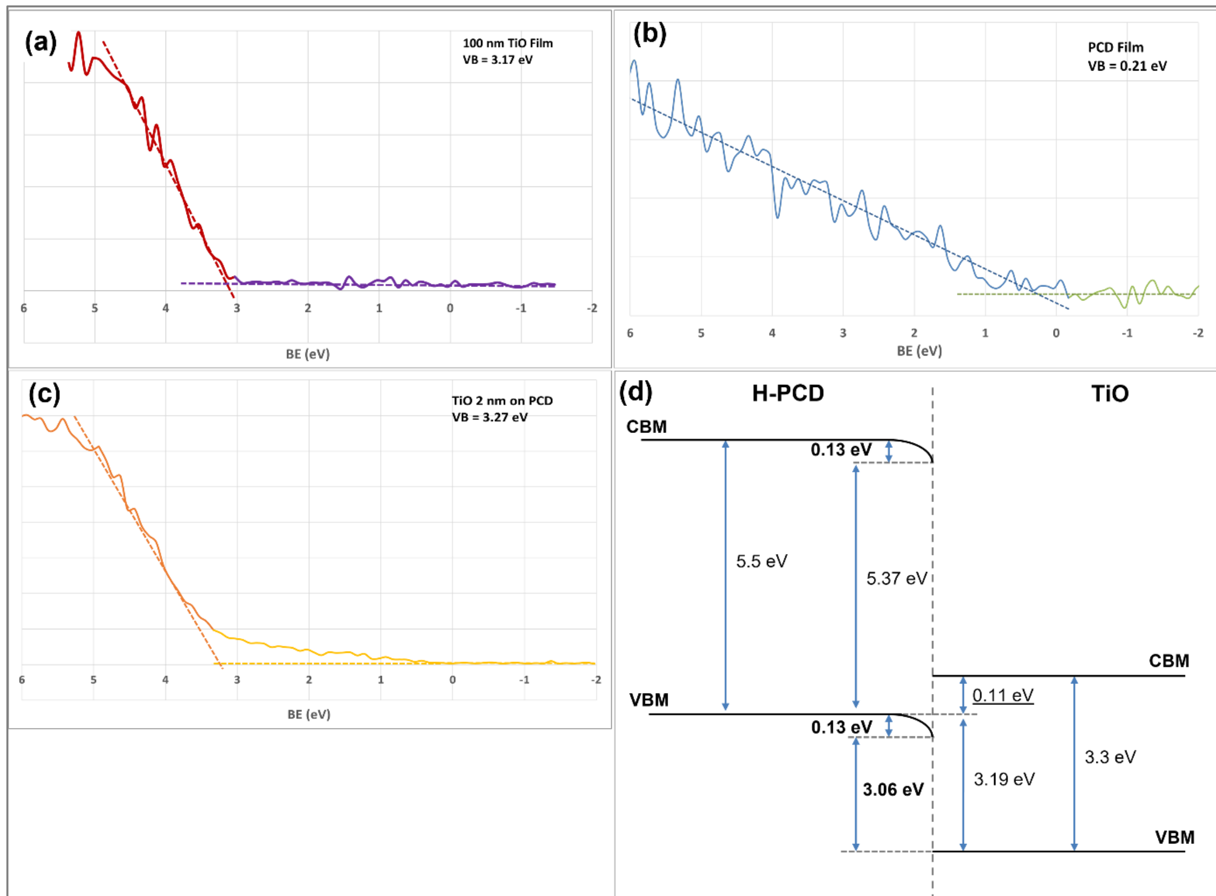

Figure 30: Valence band determinations from XPS spectra for (a) 100nm TiO film, (b) PCD film and (c) 2 nm TiO film on PCD; (d) represents the energy band alignment of TiO and H-terminated PCD, where CBM and VBM are conduction band minimum and valence band maximum, respectively. ΔE_V and PCD band bending, 3.06 eV and 0.13 eV, respectively, are highlighted.

4.0 Conclusions

ALD TiO_2 films demonstrated expected film growth behaviour across the tested temperature range 180-220 ^oC, with an initial decrease in Ti loading until 200 ^oC, where an increase in Ti intensity was realized, and continued for higher temperatures. This was thought to be related to the TDMAT decomposition rates, reported in literature, which were shown to increase above 200 ^oC. The introduction of a residence time, from 4-8 s, for both TDMAT and H_2O resulted in a variation in Ti loading despite constant precursor pulses, for depositions carried out at 210 ^oC. The more constant Ti loading occurred nearer to 8 s suggesting that at least this amount of time was needed to obtain a homogenized surface.

The TiO films used for energy band alignment determination were therefore deposited at 200 ^oC with 4 s residence times. In general, the TiO films measured by XPS were O rich, giving rise to TiO_{2+x} stoichiometry. This was also seen for 2 nm TiO films on the H-PCD surface for which initial ALD cycles

seemed to contribute high O incorporation, thus longer residence times are likely more effective on heterogeneous surfaces such as that of H-PCD for preventing O contamination in the film. The carbonyl and carboxyl groups present on the PCD surface resulted from exposure to the ALD precursors as they were not measured for the H-PCD film. Their presence is consistent with O-treated diamond surfaces and likely facilitated through O reactions with neighbouring -H and -OH surface terminations. Initial ALD cycles therefore modified the H-PCD surface via exposure to H_2O rather than TDMAT, as Ti-C bonding was not apparent in the XPS spectra.

Finally, the energy band alignment between ALD TiO and PCD films was diagrammatically depicted subsequent to calculations based on the Kraut method. ΔE_V was calculated to be 3.06 eV, sufficient to prevent charge leakage from the p-type diamond film, while PCD band bending was 0.13 eV. The small E_g of TiO, however, placed the TiO CBM close to the PCD VBM thus providing the opportunity for conductivity between the p-type PCD and TiO films, which may permit current leakages across the interface, compromising its integrity for applications which require capacitive rather conductive properties.

1 K. Kukli, M. Ritala, M. Schuisky, M. Leskelä, T. Sajavaara, J. Keinonen, T. Uustare and A. Hårsta, *Chem. Vap. Depos.*, 2000, **6**, 303–310.

2 J. Park, N. K. Yu, D. Jang, E. Jung, H. Noh, J. Moon, D. Kil and B. Shong, *Coatings*, 2020, **10**, 712.

3 T. Arroval, L. Aarik, R. Rammula, V. Kruusla and J. Aarik, *Thin Solid Films*, 2016, **600**, 119–125.

4 H. Saare, S. K. Song, J. S. Kim and G. N. Parsons, *J. Appl. Phys.*, 2020, **128**, 105302.

5 L. Ghazaryan, S. Handa, P. Schmitt and V. Beladiya, *Nanotechnology*, 2021, **32**, 095709.

6 Q. Xie, J. Musschoot, D. Deduytsche, R. L. Van Meirhaeghe, C. Detavernier, S. Van den Berghe, Y.-L. Jiang, G.-P. Ru, B.-Z. Li and X.-P. Qu, *J. Electrochem. Soc.*, 2008, **155**, H688.

7 M. E. Dufond, M. W. Diouf, C. Badie, C. Laffon, P. Parent, D. Ferry, D. Grosso, J. C. S. Kools, S. D. Elliott and L. Santinacci, *Chem. Mater.*, 2020, **32**, 1393–1407.

8 M. P. Gonullu and H. Ates, *Superlattices Microstruct.*, 2020, **142**, 106529.

9 B. Abendroth, T. Moebus, S. Rentrop, R. Strohmeyer, M. Vinnichenko, T. Weling, H. Stöcker and D. C. Meyer, *Thin Solid Films*, 2013, **545**, 176–182.

10 J. Dendooven, S. Pulinthanathu Sree, K. De Keyser, D. Deduytsche, J. A. Martens, K. F. Ludwig and C. Detavernier, *J. Phys. Chem. C*, 2011, **115**, 6605–6610.

11 Q. Xie, Y. L. Jiang, C. Detavernier, D. Deduytsche, R. L. Van Meirhaeghe, G. P. Ru, B. Z. Li and X. P. Qu, *J. Appl. Phys.*, 2007, **102**, 083521.

12 H. H. Sønsteby, A. Yanguas-Gil and J. W. Elam, *J. Vac. Sci. Technol. A*, 2020, **38**, 020804.

13 S. Zhuiykov, M. K. Akbari, Z. Hai, C. Xue, H. Xu and L. Hyde, *Mater. Des.*, 2017, **120**, 99–108.

14 E. T. Norton and C. Amato-wierda, *Chem. Mater.*, 2001, **13**, 4655–4660.

15 J. P. A. M. Driessen, J. Schoonman and K. F. Jensen, *J. Electrochem. Soc.*, 2001, **148**, G178–G184.

16 R. Gupta and R. Vaid, *IEEE Trans. Electron Devices*, 2021, **68**, 2625–2632.

17 S. Mollah, K. Hussain, R. Floyd, A. Mamun, M. Gaevski, M. V. S. Chandrashekhar, I. Ahmad, G. Simin, V. Wheeler, C. Eddy and A. Khan, *Phys. Status Solidi Appl. Mater. Sci.*, 2020, **217**, 1900802.

18 H. Song, D. Shin, J. Jeong, H. Park and D. Ko, *AIP Adv.*, 2019, **9**, 035333.

19 Y. Baek, S. Lim, L. H. Kim, S. Park, S. W. Lee, T. H. Oh, S. H. Kim and C. E. Park, *Org. Electron.*, 2016, **28**, 139–146.

20 J. Robertson, *Eur. Phys. J. Appl. Phys.*, 2004, **28**, 265–291.

21 Y. J. Shi, R. J. Zhang, D. H. Li, Y. Q. Zhan, H. L. Lu, A. Q. Jiang, X. Chen, J. Liu, Y. X. Zheng, S. Y. Wang and L. Y. Chen, *J. Phys. D. Appl. Phys.*, 2018, **51**, 085301.

22 M. Seo, S. Ho Rha, S. Keun Kim, J. Hwan Han, W. Lee, S. Han and C. Seong Hwang, *J. Appl. Phys.*, 2011, **110**, 024105.

23 P. Nunez, M. H. Richter, B. D. Piercy, C. W. Roske, M. Cabán-Acevedo, M. D. Losego, S. J. Konezny, D. J. Fermin, S. Hu, B. S. Brunschwig and N. S. Lewis, *J. Phys. Chem. C*, 2019, **123**, 20116–20129.

24 S. Wang, L. Pan, J. J. Song, W. Mi, J. J. Zou, L. Wang and X. Zhang, *J. Am. Chem. Soc.*, 2015, **137**, 2975–2983.

25 J. W. Liu, M. Y. Liao, M. Imura, R. G. Banal and Y. Koide, *J. Appl. Phys.*, 2017, **121**, 224502.

26 K. Wu, M. Liao, L. Sang, J. Liu, M. Imura, H. Ye and Y. Koide, *J. Appl. Phys.*, 2018, **123**, 161599.

27 A. Jaggernauth, R. M. Silva, M. A. Neto, F. J. Oliveira, I. K. Bdikin, M. P. Alegre, M. Gutiérrez, D. Araújo, J. C. Mendes and R. F. Silva, *Surf. Coatings Technol.*, 2020, **397**, 125991.

28 E. . Skopin, K. Abdukayumov, P. Abi Younes, M. Anikin, H. Roussel, J. L. Deschanvres and H. Renevier, *Thin Solid Films*, 2021, **723**, 138591.

29 K. Kukli, M. Ritala and M. Leskela, *J. Electrochem. Soc.*, 1995, **142**, 1670–1675.

30 K. Kukli, M. Ritala, R. Matero and M. Leskela, *J. Cryst. Growth*, 2000, **212**, 459–468.

31 M. Maarouf, M. Haider, Q. A. Drmosh and M. B. Mekki, *Crystals*, 2021, **11**, 239.

32 B. Bharti, S. Kumar, H. N. Lee and R. Kumar, *Sci. Rep.*, 2016, **6**, 1–12.

33 M. J. Jackman, A. G. Thomas and C. Muryn, *J. Phys. Chem. C*, 2015, **119**, 13682–13690.

34 O. Rosseler, M. Sleiman, V. N. Montesinos, A. Shavorskiy, V. Keller, N. Keller, M. I. Litter, H. Bluhm, M. Salmeron and H. Destaillats, *J. Phys. Chem. Lett.*, 2013, **4**, 536–541.

35 D. Wei, T. Hossain, N. Y. Garces, N. Nepal, H. M. Meyer, M. J. Kirkham, C. R. Eddy and J. H. Edgar, *ECS J. Solid State Sci. Technol.*, 2013, **2**, 110–114.

36 S. Torrengo, R. Canteri, R. Dell'Anna, L. Minati, A. Pasquarelli and G. Speranza, *Appl. Surf. Sci.*, 2013, **276**, 101–111.

37 E. . Kraut, R. . Grant, J. . Waldrop and S. . Kowalczyk, *Phys. Rev. Lett.*, 1980, **44**, 1620–1623.

38 S. Ghodbane, D. Ballutaud, F. Omnès and C. Agnès, *Diam. Relat. Mater.*, 2010, **19**, 630–636.

39 J. I. B. Wilson, J. S. Walton and G. Beamson, *J. Electron Spectros. Relat. Phenomena*, 2001, **121**, 183–201.

40 P. Strobel, J. Ristein and L. Ley, *Diam. Relat. Mater.*, 2008, **17**, 1362–1366.

41 M. A. Neto, G. Pato, N. Bundaleski, O. M. N. D. Teodoro, A. J. S. Fernandes, F. J. Oliveira and R. F. Silva, *Diam. Relat. Mater.*, 2016, **64**, 89–96.

42 J. I. Enriquez, F. Muttaqien, M. Michiuchi, K. Inagaki, M. Geshi, I. Hamada and Y. Morikawa, *Carbon N. Y.*, 2021, **174**, 36–51.

43 M. Wang, N. Simon, C. Decorse-Pascanut, M. Bouttemy, A. Etcheberry, M. Li, R. Boukherroub and S. Szunerits, *Electrochim. Acta*, 2009, **54**, 5818–5824.

44 Z. Shpilman, I. Gouzman, E. Grossman, R. Akhvlediani and A. Hoffman, *Appl. Phys. Lett.*, 2008, **92**, 234103.

45 S. Chaudhuri, S. J. Hall, B. P. Klein, J V Macpherson, R. J. Maurer, M. Walker and A. J. Logsdail, *Commun. Mater.*, 2022, **3**, 6.

46 S. Korkos, N. J. Xanthopoulos, M. A. Botzakaki, C. Drivas, S. Kennou, S. Ladas, A. Travlos, S. N. Georga and C. A. Krontiras, *J. Vac. Sci. Technol. A*, 2020, **38**, 032402.

47 J. W. Liu, M. Y. Liao, M. Imura and Y. Koide, *Appl. Phys. Lett.*, 2012, **101**, 1–5.

48 Y. Y. Lebedinskii, A. G. Chernikova, A. M. Markeev and D. S. Kuzmichev, *Appl. Phys. Lett.*, 2015, **107**, 5–9.

49 J. Zhao, J. Liu, L. Sang, M. Liao, D. Coathup, M. Imura, B. Shi, C. Gu, Y. Koide and H. Ye, *Appl. Phys. Lett.*, 2016, **108**, 1–6.

50 D. O. Scanlon, C. W. Dunnill, J. Buckeridge, S. A. Shevlin, A. J. Logsdail, S. M. Woodley, C. R. A. Catlow, M. J. Powell, R. G. Palgrave, I. P. Parkin, G. W. Watson, T. W. Keal, P. Sherwood, A. Walsh and A. A. Sokol, *Nat. Mater.*, 2013, **12**, 798–801.

51 H. H. Pham and L. Wang, *Phys. Chem. Chem. Phys.*, 2015, **17**, 541–550.

52 A. Yildiz, F. Iacomi and D. Mardare, *J. Appl. Phys.*, 2010, **108**, 083701.

Chapter 5: Fabrication of B-doped Polycrystalline Diamond Films and MOS Devices

1.0 Introduction

A fundamental step in electronic device fabrication is the use of component materials possessing properties which are both reproducible and targeted to the application. Thin diamond films grown onto substrates have been explored for MOS capacitors and transistors to mitigate the effects of heat in electronics and for use in power devices. This results from the theoretical properties of diamond namely, high thermal conductivity (2290-3450 $Wm^{-1}K^{-1}$), ultra-wide bandgap (5.47 eV) and high electric breakdown field (>10 $MVcm^{-1}$)[1,2], lending pertinence to such applications. In terms of reproducibility, mechanisms involved in the growth of diamond films have been reported in literature with emphasis placed on parameters resulting in the achievement of particular morphological, mechanical and electrical properties[3–7]. This general understanding of conditions which lead to films characterized by B concentrations, resistivities and charge carrier mobilities, are well accepted but may be subject to discrepancies based on differences in custom-built deposition systems and precursor gas sources. It is therefore prudent to plumb the growth conditions for the specific system utilized to identify reproducible film resistivities and targeted properties for MOS devices.

Fabrication and conductivity of PCD films have already been discussed in Chapter 1, sections 3.1 and 3.2, however the literature relevant to this chapter is reiterated here. Low pressure fabrication of PCD films can be achieved by one of the many types of plasma assisted CVD techniques[8,9]. HFCVD is economically beneficial with a thermal activation process enabling ease of use and understanding of the growth mechanism. Heavily B-doped free-standing diamond films were grown by HFCVD at a relatively high growth rate of 4.2 µm/h[9], and B incorporation into HFCVD grown (100) single crystal diamond was suggested to be more efficient than MPCVD techniques[10]. These examples demonstrate the continued validation of HFCVD for BDD film growth. Boron, as a commonly used dopant, enhances the conductivity of diamond films by introducing p-type acceptors (holes) into the diamond lattice by replacing displaced C atoms. Mid-gap states are thereby introduced at a relatively shallow activation energy, 0.37 eV, above the valence band[4,11]. This required energy may be high for room temperature activation of dopant charge carriers but becomes less problematic in high temperature applications.

Diamond film fabrication parameters, including B precursor concentration, have been shown to influence film morphology and electronic properties. Low B addition into the gas phase, B/C <500 ppm, has the effect of increasing grain size and BDD film growth rate, whereas high B addition, B/C >4000 ppm, results in a loss of crystallinity[12]. The benefit of larger grain sizes is the presence of fewer grain boundaries and impurity non-diamond species, thereby approximating the theoretical properties of diamond. BDD films demonstrate metal-like behaviour when heavily doped (>10^{20} B atoms cm^{-3})

and p-type semiconducting behaviour when lightly doped (10^{19} B atoms cm^{-3})[4,13]. The metal-like behaviour at higher doping concentrations is due to a significant overlap in the excited states of B atoms which forms an impurity band in contact with the top of the valence band, thereby omitting the need for thermal activation[4,14]. Film conductivity is, however, not linearly proportional to B concentration, and at concentrations $>10^{21}$ cm^{-3} BDD film conductivity was shown to decrease due to a lowered hole mobility, explained by the formation of B dimers (B-B), as opposed to single B substitution defects formed at lower dopant concentrations[14]. B dimers possess high acceptor energies which again hinder ionization from the valence band to the dopant level[14] suggesting that indefinite increases in the B dopant will not result in more conductive films.

Irrespective of doping, conductivity is generated from adsorbates on an H-terminated surface, and explained via a transfer doping mechanism whereby electrons from the diamond are transferred to unoccupied states in the surface adsorbate layer leaving behind holes in diamond just under its surface[1,15]. Electron transfer is instigated by modulation of the electronic energy levels at the adsorbate–H-diamond interface, due to the higher electron affinity (EA) of the adsorbates, and therefore stronger attraction, compared to the negative EA (NEA) of H-diamond[16]. Studies have also focused on the tunnelling of electrons from conductive substrates or interfaces into diamond surface states, their travel facilitated through the film by grain boundaries and non-diamond channels[17,18]. Electron field emission through doped and undoped PCD films was shown to originate preferentially from grain boundaries rather than the diamond grains, when analysed by tunnelling atomic force microscopy[18]. The application of a field across the PCD-substrate can therefore instigate conductivity from conductive non-diamond phases irrespective of the introduction of charge carriers by doping. This becomes particularly interesting for MOS structures whereby the presence of the gate bias is to control charge carriers and that of the high-κ oxide, to prevent leakage through the gate. The presence of both h^+ due to B dopants and e^- from graphite phases may create highly conductive films with the movement of charge carriers irrespective of the applied bias, realizing the loss of gate control.

The work presented here studies the resistivities of BDD films grown by HFCVD under various conditions. MOSFETs are prepared using these films with a TiO dielectric layer and their behaviour analysed. The utilization of TiO_2 as a gate dielectric or passivation layer specifically for diamond MOS electronic devices is rare. Liu et al. have reported on its use, in concert with Al_2O_3, as a bilayer gate dielectric for single crystal diamond MOSFETs and MOSCAPs[19]. A leakage current of 2.1E-5 Acm^{-2} was obtained at -4 V and a maximum drain–source current, I_{DS}, of -11.6 $mAmm^{-1}$ was measured[19]. In addition, it was determined that the valence band offset (ΔE_V) for this bilayer dielectric with H-terminated diamond was 2.3 eV, sufficient for preventing the uncontrolled passage of charge carriers across the dielectric[19]. κ values for TiO are reported between 25-80[20-23]. Despite few incidences in the study of TiO_2 dielectrics for diamond-based electronics, electrical characterization of FETs employing them has been reported for organic and high-electron-mobility semiconducting materials[21,23]. This work therefore discusses the not only the BDD film properties with the MOSFET behaviour but considers the TiO conductive properties, which seems to vary with BDD film characteristics.

2.0 Experimental Procedure

2.1. Diamond Film Fabrication

High resistivity Si (100) substrates, approximately 1 cm^2 were placed in isopropanol and cleaned via ultrasound for 10 minutes, then dried by compressed air. They were subsequently placed into individual beakers containing a diamond seeding solution, 0.5 g 40-60 μm diamond particles in 5 ml isopropanol, and agitated in ultrasound for 1 hour. The substrates were subsequently removed from the solution, rinsed with ethanol, twice, by placing in ultrasound for 2 minutes and then with flowing ethanol, then dried by compressed air. They were then introduced into the chamber for PCD film growth by HFCVD. The parameters used for PCD growth are given in Table 5; those held constant were the gas pressure in the chamber at 50±5 mbar, substrate temperature at 780±10 ^oC, H_2 flow at 100 ml/min, Ar flow at 10 ml/min and duration of exposure to diamond growth conditions at 75 minutes. Ar was used as the carrier gas for the B precursor (B_{pre}), B_2O_3 mixed in ethanol with a B/C ratio of 10 000 ppm, and heated to 70 ^oC.

Table 5: HFCVD growth conditions for polycrystalline diamond films

Test	CH_4 flow rate (sccm)	B_{pre} flow rate (sccm)	B_{pre}/CH_4 (ppm)
BDD1	7	2.5E-4	36
BDD2	5	2.5E-4	50
BDD3	3	2.5E-4	83
BDD4	2	2.5E-4	125
BDD5	3	5.0E-4	167
BDD6	5	1.0E-3	200
BDD7	3	1.0E-3	333
BDD8	5	2.5E-3	500
BDD9	3	2.5E-3	833

2.2. Diamond Film Characterization

The resulting diamond films were characterized by SEM using Hitachi S4100 equipment with accelerating voltages in the range 15-25 kV, from which their surface morphology and thickness were determined.

Analysis of surface topography was performed using Sensofar Metrology 3D optical profiler system.

Film resistance was determined from I-V measurements on transfer length method (TLM) contact arrangements using Keithley 2400-series systems. Au/Pd contacts, 1x8 mm, were deposited onto the diamond film surface using a mask to achieve 4 contacts. The samples were then annealed at 600 ^oC in an N_2 environment for 60 minutes with a heating and cooling rate of 8 ^oC/min so that ohmic contacts

could be attained. 2-probe current measurements were taken for applied voltages -10 V to 10 V and 10 V to -10 V. The gradients of the I-V lines were used to determine the resistances between the contact distances, 6 in total, and were subsequently plotted against said distances to obtain the film resistance. Film resistivity was then obtained from the product of resistance and film thickness. This analysis is typical for TLM.

2.3. TiO Deposition on Diamond Film Surface

HFCVD grown diamond films were rinsed in ethanol then dried in compressed air. They were placed into the centre of the ALD chamber which was purged for 50 cycles with 100 sccm N_2 gas. H_2O was used as the O precursor while tetrakisdimethylamide Ti (TDMAT) was used as the Ti precursor. One deposition cycle was defined by: H_2O pulse–H_2O residence–N_2 purge–TDMAT pulse–TDMAT residence–N_2 purge and was allotted the respective times of 0.1 s–4 s–30 s–0.2 s–4 s–20 s. The N_2 flow rate during depositions was kept at 40 sccm, depositions were performed at 210 ^oC and TDMAT precursor temperature was set to 70 ^oC. TiO films were grown to thicknesses of 80-100 nm on PCD surfaces.

2.4. MOSFET Fabrication and Characterization

MOSFET fabrication was carried out on TiO-BDD samples at the Institute of Microelectronics of Barcelona (IMB-CNM CSIC), Barcelona, Spain. Positive photoresist is applied to mask the area between source (S) and drain (D), TiO_2 is then wet-etched using SiO_2 etch with H_3PO_4. Ti/Au is then deposited, and lift-off performed to obtain Ti/Au bilayer for electrical connections on the patterned gate (G), S and D areas. TLM analysis was performed to ensure that contacts to BDD surfaces were ohmic. Annealing was performed for some of the samples at 450 ºC for 5 minutes but no significant improvement in the ohmic contact was observed. After ohmic contact formation, a second metal layer formed with Al (first batch) and Ti/Au (second batch) was deposited. A second photolithography mask was applied to pattern this metal layer which acted as the gate contact. Several gate lengths ranging from 2 µm to 24 µm have been integrated. The width of the gate was 150 µm and the distance between the drain and gate is 12 µm.

The morphological characterization of the different components of the devices, as well as the inspection of the cross-section of the different layers, were done using the focused ion beam (FIB)/SEM Cross-beam 550 (Carl Zeiss). The system is equipped with microanalysis capabilities (Aztec from Oxford Instruments) for element identification and quantification. SEM was used to characterize the different components of the devices and their morphology, choosing the high contrast/resolution In-lens (immersion lens) detector. Top-view high-resolution surface and topography characterization were done with low energy (3 keV) and low current (45 pA) beam conditions, and tilted images were obtained by increasing the energy to 5 keV in order to increase the depth of focus.

FIB cross sectioning of the different parts of the devices was obtained by first depositing, in the regions of interest, 10-20 nm Pt by electron beam induced deposition (EBID) and, on top of that, 200 nm of Pt by focused ion beam induced deposition (FIBID). This step is done at the SEM/FIB system in

order to ensure a smooth cross-section, preserving the integrity of the different layers, avoiding waterfall effects due to non-uniform material densities and/or sputter rates. After this preliminary step, the FIB milling processes is programmed to produce new slides of the different regions of interest, using a Ga ion beam at 1.5 nA and 30 kV to perform the FIB cuts. The sample is positioned at 54 ^{o} so that the ion beam is perpendicular to the surface of the sample, and the SEM column at 36 ^{o} for real time inspection.

EDX analysis is performed for the cross-section of the gate in three different regions, x_1, x_2 and x_3 (see Figure 35). Measured Pt and C elements are present in the protective deposited metalorganic material which used the precursor trimethyl (methylcyclopentadienyl) platinum (IV) $MeCpPt^{IV}Me_3$. In addition, Ga is detected in all regions of the cross-section as a result of the FIB cut. Si also appears in the top-most layers as measurements were collected using 10 keV to enhance the Ti signal, and this higher energy increased the volume of analysis thereby measuring contributions from the Si substrate.

3.0 Results and Discussion

3.1. PCD Film Sheet Resistivity

The calculated sheet resistivities, ρ_{sh}, of the resulting PCD films are given in Table 6, along with their sheet resistances, R_{sh}, and film thicknesses, t. In addition, the R_c/R_{sh} ratios are shown, obtained from TLM analysis, and describe the ratio of contact resistance, R_c, to sheet resistance, R_{sh}. These values are quite high, and, at best, R_c is only one order of magnitude smaller than R_{sh}. The ppm B_{pre}/CH_4 value, based on gas flow rates introduced in the chamber, is used since film growth rate and morphology are influenced by both B and CH_4 concentrations, thereby influencing ρ_{sh}.

Table 6: PCD film properties, film thickness, sheet resistance and sheet resistivity

Test	Film thickness t (cm)	B(pre)/ CH_4 (ppm)	Sheet Resistance R_{sh} (Ω/sq)	R_{sh} error (Ω/sq)	Sheet Resistivity ρ_{sh} (Ωcm)	ρ_{sh} error (Ωcm)	R_c/R_{sh}
BDD1	2.60E-04	36	339	84.5	8.8E-02	2.2E-02	0.5
BDD2	1.30E-04	50	947	64.7	1.2E-01	8.4E-03	0.2
BDD3	5.30E-05	83	1607	55.5	8.5E-02	2.9E-03	0.3
BDD4	3.13E-05	125	2121	721.2	6.6E-02	2.3E-02	0.1
BDD5	4.80E-05	167	779	212.2	3.7E-02	1.0E-02	0.9
BDD6	1.30E-04	200	2359	104.7	3.1E-01	1.4E-02	0.3
BDD7	4.60E-05	333	4534	237.7	2.1E-01	1.1E-02	0.3
BDD8	1.00E-04	500	1065	61.2	1.1E-01	6.1E-03	0.2
BDD9	9.70E-05	833	59	5.4	5.8E-03	5.2E-04	0.3

The relationship between R_{sh} and ppm B_{pre} with respect to CH_4 volumetric flow is graphically represented in Figure 31, along with that for ρ_{sh}; the two graphs showed similar trends. PCD films, for the parameter ranges explored, displayed ρ_{sh} values between 6×10^{-3} to 3×10^{-1} Ωcm, with R_{sh} values also spanning 2 orders of magnitude. It should be noted, however, that all the values lie between 10^{-1}-10^{-2} Ωcm and 10^{2}-10^{3} Ω/sq, respectively, with the exception of BDD9 which was performed with the highest B_{pre}/CH_4. A decrease in ρ_{sh}, and R_{sh}, with increased B incorporation is expected as B atoms generate p-type conduction due to their role as e^- acceptors in the diamond lattice. Figure 31 however demonstrates two such regions, one of low B_{pre}/CH_4 (50-170 ppm) in the HFCVD gas mixture, exhibiting a small variation in resistivity, and the other of higher B_{pre}/CH_4 (200-830 ppm). It is generally accepted that there are 3 mechanisms of conduction that can occur in BDD, dependant on the concentration of B measured in the diamond film. Low concentration films, $<10^{19}$ B atoms/cm^3, display p-type semiconducting properties, thereby fulfilling conduction through the valence band and requiring an activation energy of 0.37 eV, while concentrations closer to 10^{20} B atoms/cm^3 realize hopping conduction through distant impurity centres, as opposed to nearest neighbour centres, referred to as variable range hopping (VRH), finally, at and above 10^{20} B atoms/cm^3 semimetal conduction occurs. It is therefore the tendency of film resistivity to decrease with increasing B concentration thereby identifying these 3 mechanisms.

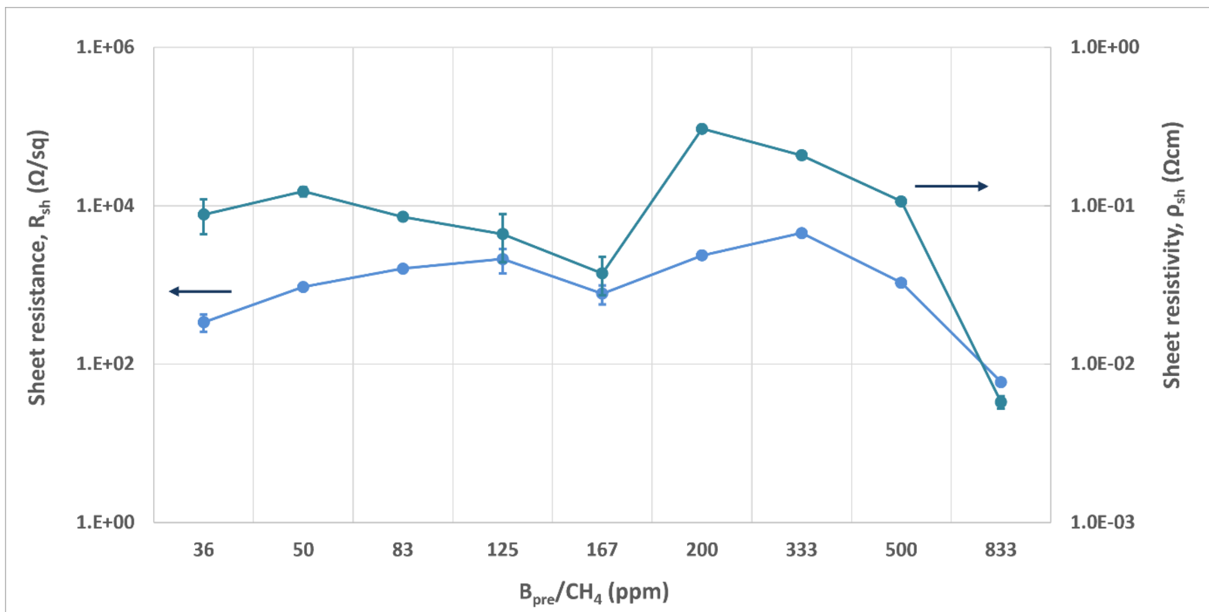

Figure 31: Sheet resistance and resistivity graphs showing their variation with B precursor to CH_4 concentration; the effect of the B is more noticeable for B_{pre}/CH_4 values from 200 ppm.

Film resistivity may however deviate from a proportional dependence on B precursor flow rate since its concentration in the gas phase does not necessarily represent the ratio incorporated into the diamond film structure. In addition, the B atoms incorporated into the film may not all contribute to lowering film resistivity. B may be incorporated as single atoms which function to increase conductivity

in PCD films, resulting in the described mechanisms in which increasing single B atom concentrations give rise to decreased film resistivities[14]. Conversely, films with high B concentrations have been shown to contain B-B dimers, signifying high acceptor energy levels, or other complex defects giving rise to B clusters, both of which act to reduce the overall number of charge carriers and result in films with higher resistivities[14]. The low ρ_{sh} of Figure 31 for B_{pre}/CH_4 <200 ppm, taking into consideration that R_{sh} in this range is also lower than expected and that film thickness does not vary sufficiently across samples to greatly influence ρ_{sh}, can therefore be due to the incorporation of B as single atoms from low B_{pre} flow rates (2.5E-4-5.0E-4 sccm) in the gas mixture, increasing film conductivity due to high mobility.

In the low range of 50-170 ppm, the B_{pre} flow rate is constant at 2.5E-4 sccm for the first 4 values while the CH_4 flow rate is changed through 7-2 sccm resulting in a small change in ρ_{sh} and demonstrating that film conductivity, in this range, is minimally affected by changes in CH_4. Figure 32 further highlights the small effect of the CH_4 flow rate on film conductivity for B_{pre} flow rates 2.5E-4-1.0E-3 sccm, evidenced by small changes in ρ_{sh} for CH_4 between 3-5 sccm, however, at 2.5E-3 sccm B_{pre}, a larger change in film conductivity is seen for the different CH_4 flow rates, which is attributed to a larger B_{pre} concentration in the gas mixture. It is also noted that films grown at 5 sccm CH_4 had higher ρ_{sh} than those grown at 3 sccm, a characteristic more noticeable at higher B_{pre} concentrations.

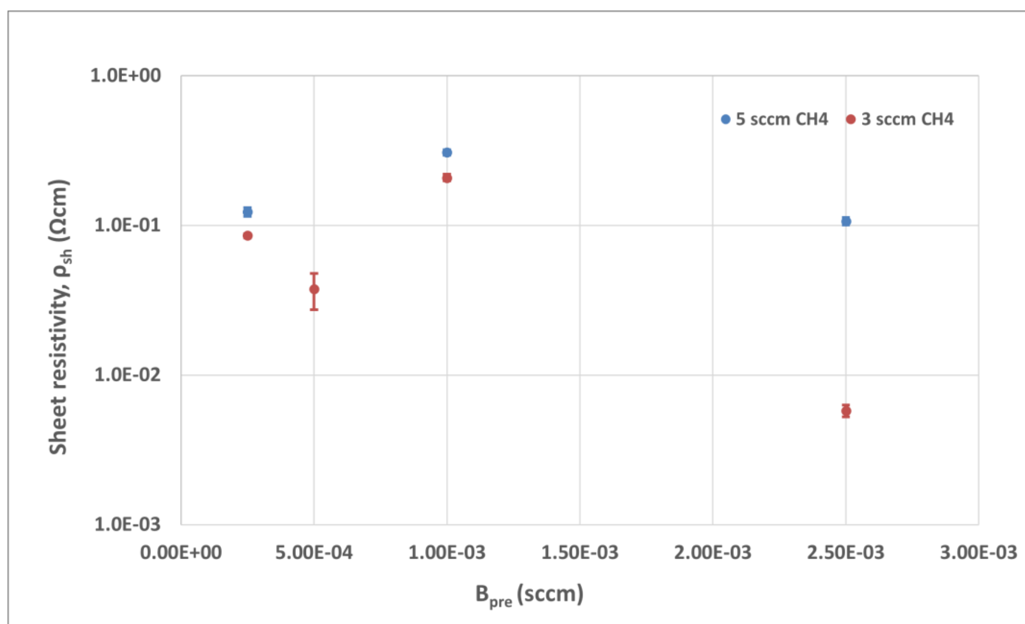

Figure 32: Variation in sheet resistivity with B precursor flow rate for CH_4 rates of 3 and 5 sccm; influence on ρ_{sh} is seen for higher B flow rates.

Morphological characterization of the BDD films was performed by SEM and is shown in Figure 33. Films grown with higher CH_4 flow rates resulted in higher growth rates and thus thicker films for the range of parameters used. An exception was observed in films grown at the highest B flow rate of 2.5E-03 sccm, which instead realized similar growth rates independent of CH_4 flow, and possibly suggests an influence of high vapour phase B concentrations on film growth rate. In addition, for the

films grown at 3 sccm CH_4, a significant increase in film growth rate was observed for B_{pre} flow rate of 2.5E-03 sccm. As sheet resistivity is dependent on film thickness, thicker films will result in higher resistivities for similar sheet resistances, so it is reasonable that 5 sccm CH_4 produces films with higher sheet resistivities, based solely on consideration of this physical property.

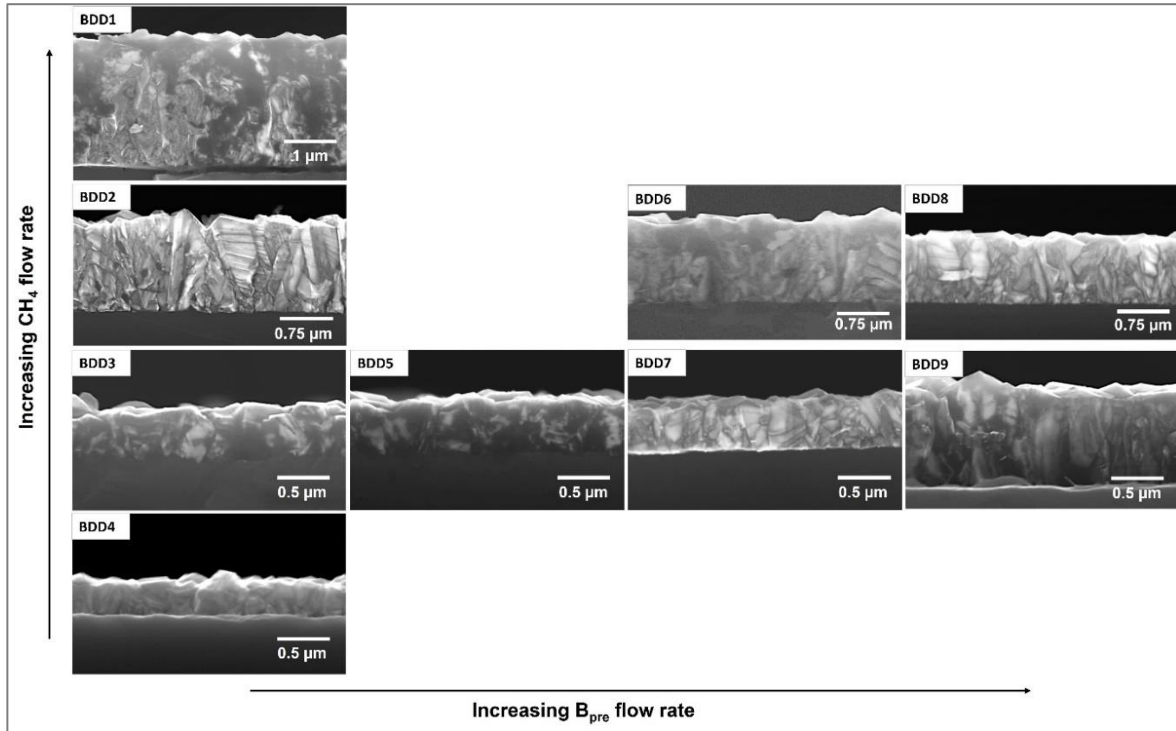

Figure 33: Cross-sectional view of BDD films grown under different parameters and presented in order of increasing CH_4 flow rate and B_{pre} flow rate.

3.2. MOS Device Characterization

MOSFETs characterization reported here are based on devices fabricated on BDD films grown from tests BDD5 and BDD7, with R_{sh} in the range 8E02–5E03 Ω/sq. Images obtained by SEM, for the transistors are given in Figure 34, with the G, S and D regions identified. Characterization of the MOS structure cross-section was also performed by SEM (Figure 35) by removing a portion of the sample by FIB in the G region. Figure 35(b) distinguishes the different layers, 150 nm Ti/Au metal contacts on 100 nm TiO, on 850 nm BDD film, and an interfacial region can be identified between Si and BDD. In addition, EDX measurements are performed on the points labelled x_1, x_2 and x_3, and their resulting

spectra (Figure 35(c)) establish regions of dominant Au, Ti and C for the metal, oxide and semiconductor films, respectively.

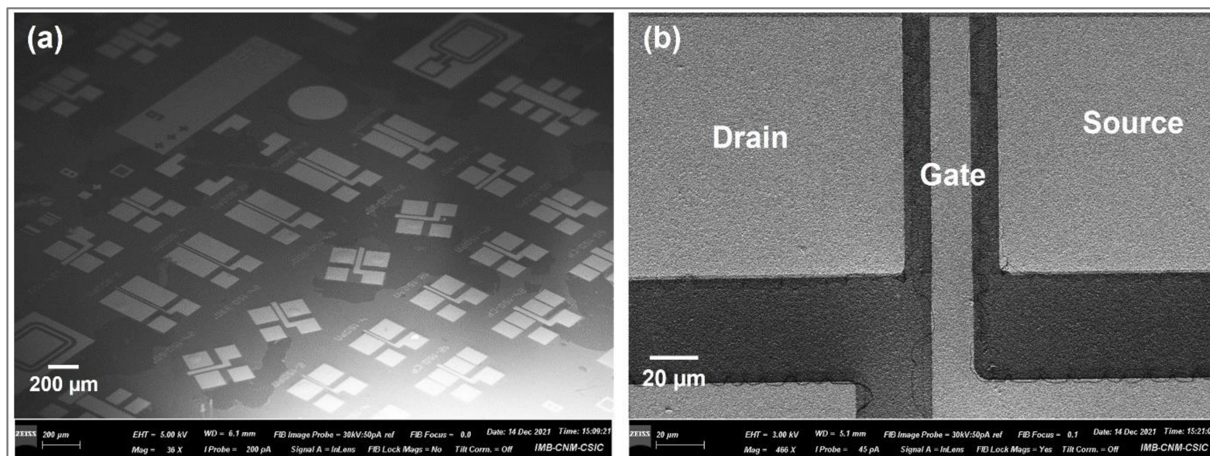

Figure 34: SEM surface images showing (a) 45 ° tilted SEM image showing fabricated MOSFETs; (b) top-view, high resolution SEM image showing the drain, source and gate electrodes of the transistor.

TiO sheet resistance was measured using two probes on the surface of the TiO-BDD5 and TiO-BDD7 samples grown under BDD5 and BDD7 conditions, respectively (Figure 36(a)). An applied bias from -1.1 to +1.1 V resulted in the flow of current near the mA range for TiO-BDD5, while that for TiO-BDD7 lay below the nA range, indicating that the TiO film of the former was not insulating. Further characterization of TiO-BDD5 (Figure 36(b)) showed the occurrence of a high G leakage current, I_G, with the application of V_{GS} from -5 to +5 V. This property coupled with the high sheet conductivity of TiO-BDD5 prevented its use in MOSFET characterization, which was then only performed for TiO-BDD7. Interestingly, TiO-BDD5 exhibited both a low TiO sheet resistance and high I_G, and had a higher conductivity for its BDD film compared to TiO-BDD7. It may therefore be hypothesized that the high BDD conductivity and TiO sheet resistance both contributed to the high I_G. Furthermore, the occurrence of the low TiO sheet resistance may be linked to the BDD5 surface characteristics as ALD conditions were constant for all BDD samples, however, further investigation is required before this can be concluded.

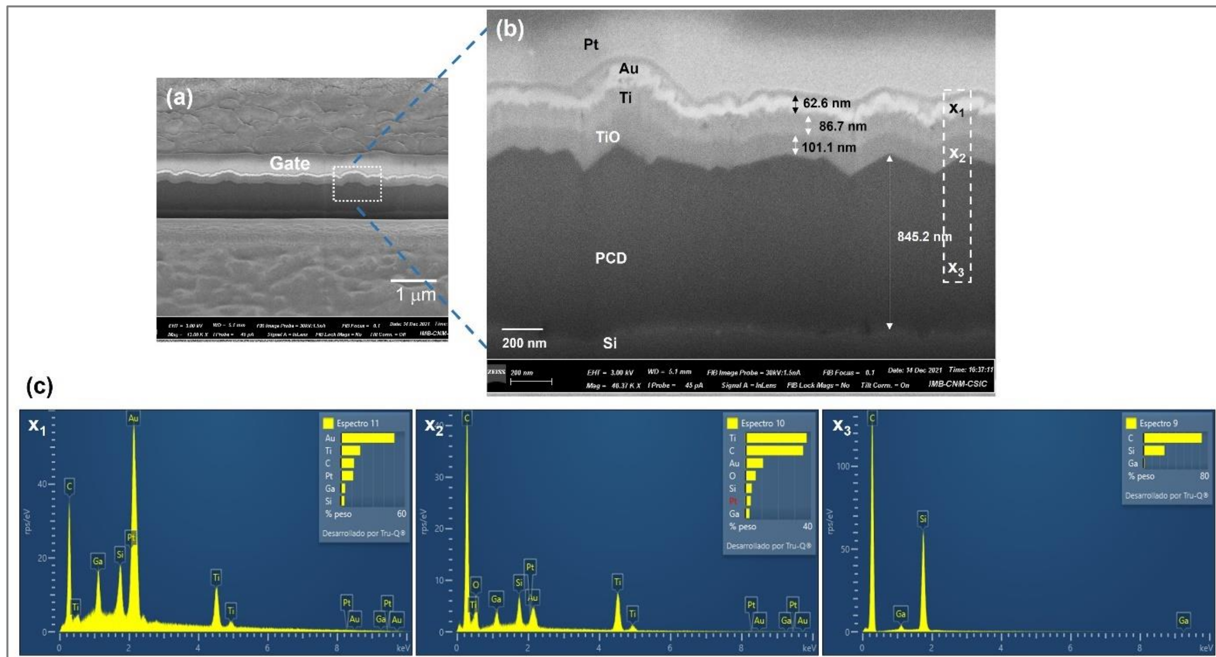

Figure 35: (a) SEM tilted image of gate area with a volume milled by FIB to reveal the cross-section; (b) magnified SEM image of gate cross-section showing the various layers and respective thicknesses; x_1, x_2, and x_3 are approximated points on the sample where EDX analysis was performed, the results of which are shown in (c).

Measurements taken on two transistors from TiO-BDD7 are shown in Figure 36(c) and (d). I_G lays between -1E-13–1E-10 A, with breakdown occurring at -9 and -15 V for the respective transistors. The current at D, I_{DS}, however, remained relatively constant at 0.47 mA for both transistors with applied V_{DS} =3V, even beyond the breakdown V demonstrating a lack of control of I_{DS} by V_{GS}. It is expected, for MOSFET operation, that V_{GS} will affect I_{DS} flowing through the BDD film. This is because the applied bias at G will impact the charge carriers, from B doping, in the film so that increasing the bias would act to either increase the charge carriers in the conduction channel, resulting in an increase in I_{DS}, or remove them, resulting in a decrease in or zero I_{DS}. In addition, the purpose of the TiO dielectric is to concentrate the charges below it, in the BDD film, preventing charge from flowing across the BDD-TiO interface. The constant I_{DS} obtained for these MOSFETs however, even after breakdown of G, when it is no longer insulating, seems to demonstrate no major influence on the charge carriers by V_{GS}, so that G does not act to modulate the charge carriers and hence I_{DS}.

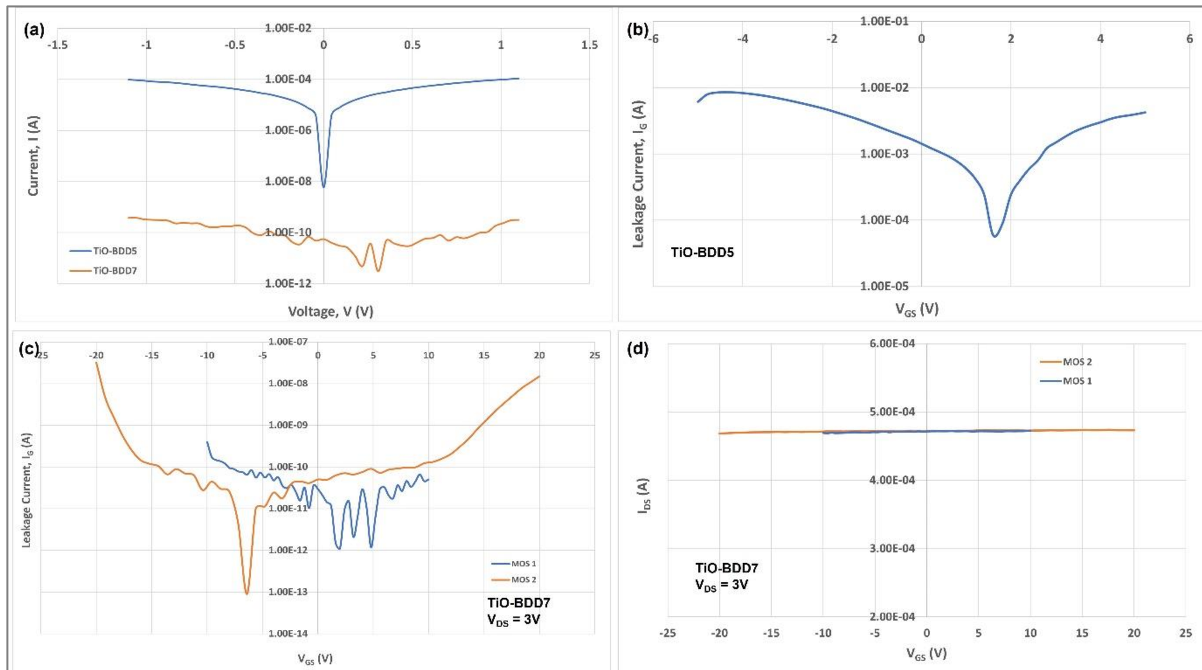

Figure 36: MOSFET characterization graphs showing (a) surface current of TiO films on BDD5 and BDD7; (b) leakage current through G of TiO-BDD5 MOSFET; (c) leakage current for 2 transistors, MOS 1 and MOS 2, fabricated from TiO-BDD7 and (d) respective drain currents for MOS 1 and MOS 2.

BDD film characteristics are likely the source of this departure from V_{GS} control, acting in concert with interfacial properties. A highly doped or conductive BDD film would mean that charges flow through it due to V_{DS} irrespective of V_{GS}. Studies on field emissions in diamond films conclude that grain boundaries and graphitic layers between crystallites are conductive regions which facilitate the passage of charge from the substrate to the surface[17,18]. Furthermore, the NEA H-terminated diamond surface and a conductive interface between the film and substrate enhance the local electric field thus permitting film conductivity[17,18]. BDD5 and BDD7 are both considered to be predominantly H-terminated as they are cooled in H plasma after fabrication, although H surface species may have oxidized over time. In addition, the BDD-Si interface contains an amorphous C layer which is noticed in Figure 35(b), but is better displayed in our earlier work with alumina films on BDD[24]. These two characteristics may give rise to an enhanced field in the BDD film which, along with the non-diamond channels, facilitates vertical conduction. This conductivity, irrespective of dopants, could therefore explain the ineffective control by V_{GS} to modulate I_{DS}.

PCD film surface roughness has also been a point of concern for interface conductivity. This is because the electric field is higher at the peaks of a rough surface rather than at its valleys due to the increased density of electric charges with aspect ratio, thus a non-uniform electric field distribution at the interface is established and has the effect of scattering charge carriers[25,26]. In addition, the enhanced electric field intensity at the peaks, compared to the valleys and the bulk, can lead to localized electrical breakdown in these areas of the dielectric and proliferate to full breakdown via the opening of conduction pathways[26,27]. Figure 37 shows SEM images of the BDD5 and BDD7 surfaces along with

the topography of BDD5 obtained by profilometry. The surfaces of the two samples are shown to be similar and the rms roughness is measured to be 86 nm. In this respect the BDD surface is rough and may have contributed to the high I_G of the TiO-BDD5 MOSFET. The TiO-BDD7 MOSFET however, does not seem to have an appreciably different surface morphology to conclude a large difference in roughness compared to that of BDD5 to conclude that the effect of roughness was indeed a significant factor. It may, however, be suggested that in terms of the MOSFET performance, smoother surfaces may give rise to lower electron emissions and charge scattering, thus providing G control and being a factor for overall performance optimization.

To explain the differences in electronic behaviour between TiO-BDD5 and TiO-BDD7, the conclusions of the previous chapters lead to consideration of the nucleation of TiO on the PCD surfaces during initial ALD cycles. The results presented in Chapters 2 and 4 for AlO and TiO films, respectively, both highlight the susceptibility of the oxide film properties to substrate surface characteristics. In the case of AlO films this was seen as changes in mechanical integrity with PCD surface species, while for TiO films, calculated stoichiometry changed either because of film thickness or type of substrate. In addition, the results for TaO films of Chapter 3 highlighted that changes in GPC were based on the number of ALD cycles on Si substrates, owed to differences in growth at the Si surface, Si and TaO surface and then finally only on the TaO surface as the film proliferated. The images of Figure 37, however, demonstrate no major difference in morphology between BDD5 and BDD7, and chemically they are both considered to be H-terminated so that TiO film nucleation is not considered to present significant differences in these regards, but the high sensitivity of ALD to surface conditions have proven to be a compelling factor in this thesis and thus may not be considered trivial for polycrystalline surfaces. Surface characteristics may therefore be extended to diamond grain orientation or concentration of grain boundaries (non-diamond) in relation to diamond composition. The higher conductivity of BDD5 may also prove to be a factor if it is also due to the H-terminations and hence a quantification of this property may be useful for exploring oxide film nucleation. What can be concluded here is that further analysis is necessary for determining the effects of the heterogeneous PCD surface on ALD film growth, and that differences in nucleation does seem to be a factor on two surfaces with similar morphological and chemical compositions.

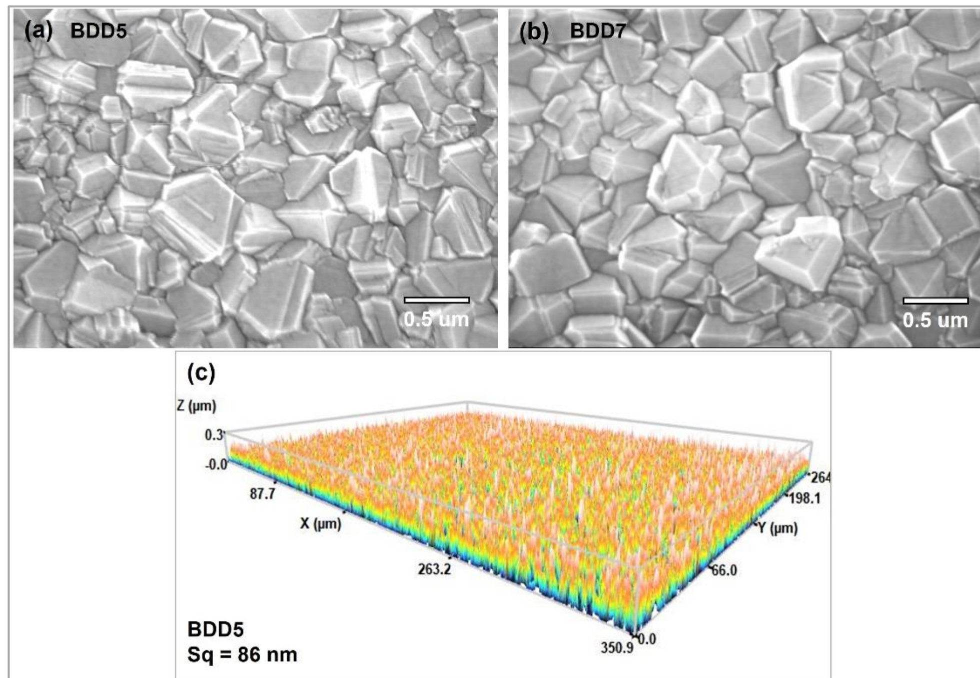

Figure 37: SEM micrographs in (a) and (b) showing the surface morphology of BDD5 and BDD7, respectively; (c) shows the topography of BDD5 with rms roughness of 86 nm.

Complementary to the effects of TiO film nucleation and the resulting MOSFET behaviour is the band alignment of TiO with H-terminated BDD films. XPS results of Chapter 4 demonstrated that both valence band and conduction band offset energies, ΔE_V and ΔE_C, respectively, for the two films in contact, were sufficiently high, >1 eV, to prevent the passage of charge across the interface. It was also shown that the CBM of TiO and VBM of H-terminated BDD were positioned very close to each other, separated only by 0.11 eV, providing a sufficiently low barrier for the passage of charge between the two films. This may occur as recombination of e^- and h^+, e^- in TiO and h^+ in BDD in a few nm across the interface, or as a leakage, I_G, via the movement of charge carriers. In our results, the high conductivity of the BDD7 film through the amorphous C interface, grain boundaries and other non-diamond content led to a lack of G control of I_{DS}, but a small I_G was obtained signifying effectiveness of the TiO film to prevent current flow across the MOS structure. This was not the case for the BDD5 films of lower resistivity, which instead exhibited I_G close to the mA range, a high leakage, meaning that the TiO layer easily permitted the flow of charge. It may be that the O-rich TiO film coupled with the high conductivity of BDD5 facilitated conductivity across the interface through the low barrier of 0.11 eV. An excess of O in the TiO film may also act as adsorbates to the PCD H-terminations thereby encouraging e^- flow from the non-diamond content towards the interface, accounting for the lack of G control in the TiO-BDD7 transistors.

4.0 Conclusions

In this work the fabrication parameters of various BDD films were presented and their resistivities measured by TLM. Films grown at low B_{pre}/CH_4 ratios, 50-170 ppm, exhibited a small variation in resistivity, while those of higher B_{pre}/CH_4, 200-830 ppm, had a larger variation in sheet resistivity and resistance. In general, however, ρ_{sh} and R_{sh} ranged from 10^{-1}-10^{-2} Ωcm and 10^{2}-10^{3} Ω/sq, respectively, with the lowest values attained for the highest B_{pre}/CH_4 gas flow ratio, likely correlated to the highest B atom concentration.

BDD5 and BDD7 films were used to fabricate MOSFETs with TiO dielectric layers grown by ALD. Different device behaviours were obtained for TiO-BDD5 and TiO-BDD7. Firstly, the TiO film on BDD5 was found to be conductive and the transistors displayed a high I_G near mA range. The TiO film on BDD7 however, was found to be insulating and its transistors measured I_G lower than the nA range. The high I_G of TiO-BDD5 was discussed as being due to the TiO film conductivity as well as the lower resistivity of the BDD5 film. It was also suggested that the conductivity of TiO may be due to surface disparities of the BDD5 and BDD7 films, although these differences are not apparently obvious, since TiO on the BDD7 films was insulating but they were both grown with the same ALD conditions. TiO film nucleation from ALD precursor exposures on the BDD surfaces was discussed as being a possible source for the electronic dissimilarity of the TiO films but this requires further investigation. TiO-BDD7 MOSFETs also displayed an I_{DS} of 0.47 mA, which remained constant irrespective of V_{GS} even after TiO breakdown. This was explained by a high BDD7 conductivity likely due to the amorphous C layer at the interface of the diamond-substrate and non-diamond content, which permitted charge carrier transport into diamond surface states.

Finally, the energy band alignment between TiO and BDD was also discussed as a possibility for TiO-BDD5 leakage current due to the low energy barrier, 0.11 eV, between the CBM of TiO and VBMof H-terminated BDD. In addition, as it pertains to the lack of G control in the TiO-BDD7 transistors, excess O in the TiO film, adsorbed on the H-terminations of BDD, may facilitate movement of e^- from the non-diamond species thereby enhancing film conductivity and preventing control through V_{GS}.

1 M. W. Geis, T. C. Wade, C. H. Wuorio, T. H. Fedynyshyn, B. Duncan, M. E. Plaut, J. O. Varghese, S. M. Warnock, S. A. Vitale and M. A. Hollis, *Phys. Status Solidi Appl. Mater. Sci.*, 2018, **215**, 1–14.

2 J. Y. Tsao, S. Chowdhury, M. A. Hollis, D. Jena, N. M. Johnson, K. A. Jones, R. J. Kaplar, S. Rajan, C. G. Van de Walle, E. Bellotti, C. L. Chua, R. Collazo, M. E. Coltrin, J. A. Cooper, K. R. Evans, S. Graham, T. A. Grotjohn, E. R. Heller, M. Higashiwaki, M. S. Islam, P. W. Juodawlkis, M. A. Khan, A. D. Koehler, J. H. Leach, U. K. Mishra, R. J. Nemanich, R. C. N. Pilawa-Podgurski, J. B. Shealy, Z. Sitar, M. J. Tadjer, A. F. Witulski, M. Wraback and J. A. Simmons, *Adv. Electron. Mater.*, 2018, **4**, 1–49.

3 N. Yang, S. Yu, J. V Macpherson and Y. Einaga, *Chem. Soc. Rev.*, 2019, **48**, 157–204.

4 J. V Macpherson, *Phys. Chem. Chem. Phys.*, 2015, **17**, 2935–49.

5 D. C. Barbosa, P. R. P. Barreto, V. W. Ribas, V. J. Trava-Airoldi and E. J. Corat, in *Encyclopedia of Nanoscience and Nanotechnology*, ed. H. S. Nalwa, American Scientific Publishers, 2011.

6 E. M. A. Fuentes-Fernandez, J. J. Alcantar-Peña, G. Lee, A. Boulom, H. Phan, B. Smith, T. Nguyen, S. Sahoo, F. Ruiz-Zepeda, M. J. Arellano-Jimenez, P. Gurman, C. A. Martinez-Perez, M. J. Yacaman, R. S. Katiyar and O. Auciello, *Thin Solid Films*, 2016, **603**, 62–68.

7 J. J. Gracio, Q. H. Fan and J. C. Madaleno, *J. Phys. D. Appl. Phys.*, 2010, **43**, 374017.

8 J. G. Buijnsters, M. Tsigkourakos, T. Hantschel, F. O. V. Gomes, T. Nuytten, P. Favia, H. Bender, K. Arstila, J.-P. Celis and W. Vandervorst, *ACS Appl. Mater. Interfaces*, 2016, **8**, 26381–26391.

9 S. Ohmagari, H. Yamada, H. Umezawa, N. Tsubouchi, A. Chayahara and Y. Mokuno, *Diam. Relat. Mater.*, 2018, **81**, 33–37.

10 S. Ohmagari, M. Ogura, H. Umezawa and Y. Mokuno, *J. Cryst. Growth*, 2017, **479**, 52–58.

11 J. H. T. Luong, B. Male, J. D. Glennon, K. B. Male and J. D. Glennon, *Analyst*, 2009, **134**, 1965–79.

12 V. V. S. S. Srikanth, P. Sampath Kumar and V. B. Kumar, *Int. J. Electrochem.*, 2012, **2012**, 1–7.

13 J. R. Oliveira, O. M. Berengue, J. Moro, N. G. Ferreira, A. J. Chiquito and M. R. Baldan, *Appl. Surf. Sci.*, 2014, **311**, 5–8.

14 P. Ashcheulov, J. Šebera, A. Kovalenko, V. Petrák, F. Fendrych, M. Nesládek, A. Taylor, Z. Vlčková Živcová, O. Frank, L. Kavan, M. Dračínský, P. Hubík, J. Vacík, I. Kraus and I. Kratochvílová, *Eur. Phys. J. B*, 2013, **86**, 443.

15 M. Kasu, *Jpn. J. Appl. Phys.*, 2017, **56**, 01AA01.

16 C. Verona, W. Ciccognani, S. Colangeli, E. Limiti, M. Marinelli and G. Verona-Rinati, *J. Appl.*

Phys., 2016, **120**, 025104.

17 M. W. Geis, N. N. Efremow, K. E. Krohn, J. C. Twichell and T. M. Lyszczarz, *Nature*, 1998, **393**, 431–435.

18 V. Chatterjee, R. Harniman, P. W. May and P. K. Barhai, *Appl. Phys. Lett.*, 2014, **104**, 171907.

19 J. W. Liu, M. Y. Liao, M. Imura, R. G. Banal and Y. Koide, *J. Appl. Phys.*, 2017, **121**, 224502.

20 R. Gupta and R. Vaid, *IEEE Trans. Electron Devices*, 2021, **68**, 2625–2632.

21 S. Mollah, K. Hussain, R. Floyd, A. Mamun, M. Gaevski, M. V. S. Chandrashekhar, I. Ahmad, G. Simin, V. Wheeler, C. Eddy and A. Khan, *Phys. Status Solidi Appl. Mater. Sci.*, 2020, **217**, 1900802.

22 H. Song, D. Shin, J. Jeong, H. Park and D. Ko, *AIP Adv.*, 2019, **9**, 035333.

23 Y. Baek, S. Lim, L. H. Kim, S. Park, S. W. Lee, T. H. Oh, S. H. Kim and C. E. Park, *Org. Electron.*, 2016, **28**, 139–146.

24 A. Jaggernauth, R. M. Silva, M. A. Neto, F. J. Oliveira, I. K. Bdikin, M. P. Alegre, M. Gutiérrez, D. Araújo, J. C. Mendes and R. F. Silva, *Surf. Coatings Technol.*, 2020, **397**, 125991.

25 S. Saito, K. Torii, Y. Shimamoto, S. Tsujikawa and E. Al, *Appl. Phys. Lett.*, 2004, **84**, 1395.

26 Y. Zhao, G. C. Wang, T. M. Lu, G. Palasantzas and J. Hosson, *Phys. Rev. B - Condens. Matter Mater. Phys.*, 1999, **60**, 9157–9164.

27 Y. S. Kim, M. Y. Sung, Y. H. Lee, B. K. Ju and M. H. Oh, *J. Electrochem. Soc.*, 1999, **146**, 3398–3402.

Chapter 6: General Conclusions and Future Perspectives

The scope of this thesis was the fabrication of high-κ dielectric oxides by ALD on polycrystalline diamond surfaces for their application in MOS structures. It was motivated by the need to achieve cost-effective electronic materials for high power applications as well as for operation in harsh environments, which include those of high temperatures, high temperature differences, and extreme mechanical vibrations. In addition, from a structural perspective, the limitation on mainstream materials such as Si, instigated by the reduction in the size of device components, has unlocked the potential for more pragmatic options and combinations. To this extent, the properties of diamond, an ultra-wide bandgap and high thermal conductivity, are considered advantageous to these niche applications, as does the investigation of its interface quality with high-κ oxides. Considering the experimental work performed in this thesis, and towards the realization of its aim, the following novelties are highlighted and conclusions proffered.

AlO, TaO and TiO films have been successfully fabricated by ALD onto both Si and PCD surfaces. AlO presents a system which has been well studied in literature especially for TMA and H_2O, and was proven to be easily deposited. ALD of TiO films was achieved using TDMAT and H_2O. The metal precursor in this case comprised a larger molecule of a different chemical family, alkylamides as opposed to alkyl, from TMA. Decomposition of TDMAT above 200 ^oC, was considered to be a factor in film growth behaviour and thus posed a challenge for saturation studies. ALD of TaO films were carried out using PDMAT and H_2O; the solid alkylamide Ta precursor contained 5 ligands to Ta, compared to 4 for that of Ti. A deposition temperature of 270 ^oC resulted in the lowest GPC but temperatures lower than this displayed a higher but constant GPCs. The challenge with the TaO system stemmed from inconsistencies in surface exposure by the precursor vapour due to the uneven heating of its solid particles. PDMAT was thus subjected to a range of heating temperatures to achieve films, and in general, provided low yield. The study of these 3 distinct systems on Si was necessary to understand growth behaviour and possible challenges prior to their deposition on the more complex PCD surfaces. Characterization of the TaO and TiO films advances the scientific knowledge of ALD parameters and inconsistencies in precursor reaction behaviour, especially since reports on ALD of TaO films by PDMAT and H_2O are scarce in published literature.

The quality of the oxide-semiconductor interface of the MOS stack has been studied in this thesis by a variety of methods namely, nanoindentation, HRTEM and XPS. The novel investigation of AlO-BDD stacks by nanoindentation for both as-grown and O-treated BDD surfaces unequivocally demonstrated differences in AlO film adhesion. The latter resisted delamination of the AlO film due to the active O surface sites which facilitated TMA adsorption on the PCD surface during initial ALD cycles. Another successful result was obtained by HRTEM analysis which clearly displayed differences

in interface quality, showing regions where the AlO film delaminated from the as-grown PCD surface, corroborating the findings from nanoindentation.

In contrast to the mechanical quality of the AlO-BDD interface, XPS was used to understand the electronic quality of the TiO-PCD interface, via calculation of the energy band alignment. This analysis is novel for TiO-PCD interfaces so that the achievement of this work is especially interesting for supplementing the knowledge of high-κ TiO for PCD devices. In our results, as-grown PCD, relative to TiO, exhibited sufficiently large, > 1 eV, ΔE_v and ΔE_c, however the TiO CBM was positioned very close to the PCD VBM, signifying a conductive interface, one unsatisfactory for MOSFET performance. Without this analysis it would have been difficult to understand the challenges associated with application of these materials so this type of analysis was shown to be crucial for this thesis. Overall, the characterization techniques utilized in this work for the purpose of interfacial analysis have proven to be effective, providing options for determining both mechanical and electronic quality. These properties are critical when considering the choice of materials for electronics used in harsh environments.

Finally, the fabrication of BDD films by HFCVD permitted testing of MOSFETs utilizing TiO films. A range of parameters were explored and conductive BDD films were achieved resulting in resistivities spanning 2 orders of magnitude. The more conductive BDD5 film demonstrated high current leakage through the gate, while that of lower conductivity, BDD7, had a low leakage current, although no gate control could be attained over the I_{DS} channel. The role of film proliferation during initial ALD cycles, evident in previous chapters, accompanied the discussion of discrepancies in film characteristics. This final chapter therefore culminates the work of the previous chapters, effectively producing devices from the fabricated materials and, with the analysis from these chapters, pragmatic discussion is given. Pertinent to this chapter is the conclusion that more experiments are required to understand the challenges faced with these MOSFETs, although investigation of the high-κ oxide–PCD interface in this thesis has been invaluable to the discussion of device feasibility.

The challenges highlighted in the discussion and conclusions of this body of work give leeway to perspectives for future work, which are provided here.

ALD TaO films using PDMAT require more repetitive tests to better understand film proliferation and precursor behaviour. It was already discussed that the use of in situ techniques such as mass uptake by a QCM could discern PDMAT surface adsorption over the number of deposition cycles. In this way, PDMAT decomposition and partial pressure over the deposition lifetime could be established. This knowledge would be important for obtaining consistent films in terms of GPC and Ta loading so that validity and reliability in their fabrication could be achieved. The low yield of PDMAT also provides a challenge, being a costly and inconsistent option for TaO films. An alternative such as $Ta(OC_2H_5)_5$, which exists as a liquid precursor, is perhaps a better contender and should be explored for ALD of TaO films.

The realization of MOSFETs based on TaO films is also categorized in this section although efforts were made towards their fabrication and characterization. These were limited by the difficulty in etching TaO from the PCD surface. It is therefore suggested that this be an opportunity for future work, either for exploring options for successful etching or changing the fabrication technique so that etching

is not required, that is, masks can be used to deposit TaO only under the gate. Complementary to TaO-PCD MOSFETs, and even pre-emptive to its operational characterization, is the study of the TaO-PCD interface for electronic quality, ensuring that band alignment can facilitates charge carrier concentration rather than promote leakage.

Pertinent also to the interface quality is the functionalization of the PCD surface, as was done in this work for AlO-BDD stacks. ALD, as a surface sensitive technique, is dependent on the active surface species for precursor adsorption so that surface functionalization prior to oxide film deposition influences interfacial bonding. Furthermore, PCD sub-surface conductivity is modified by the surface species, modulating band bending and alignment. To this extent, the interface for TiO and TaO with functionalized PCD can be studied to better understand the ramifications on interface quality and MOSFET operation.

One issue that has not been addressed in this work but has arisen in much of the discussion leading to its implementation and conclusions is the roughness of the PCD surface. This consideration has plagued MOSFET operations as rough surfaces are known to possess a non-uniform charge distribution whereby breakdown at the interface can occur due to concentrated points of charge. Efforts to polish PCD to attain a smoother surface have been reported in literature although disadvantages, such as the introduction of defects and limited reproducibility, has accompanied such attempts. It is however worth exploring this possibility for the purpose of expanding the knowledge in this area. Polished or smoothed, by some other means, surfaces may influence ALD reactions, band alignments, mechanical stability, and electronic properties, and may thus be considered in contrast to as-grown surfaces.

Finally, the differences in the TiO films of TiO-BDD5 and TiO-BDD7 require further investigation. If the oxide film proliferation is affected by the specific BDD surface then it may be better understood by studying the interface after a few ALD cycles, 10-20, and determining changes, if any, in conductivity and chemical composition. It may also be that TiO film discrepancies may be due to other characteristics of the PCD film like crystal orientation, for example. In such a case, this may be unravelled by performing depositions on SCD surfaces and determining film conductivity and stoichiometry.

In general, there are many avenues for the progression of this work, both from the perspective of the materials utilized, the interfaces of the two films, and the performance of the MOS devices. As the overall motivation of the work was for achievement of cost-effective devices for applications in harsh environments, then optimized diamond MOS structures can then be tested under such conditions, including high temperatures.